

MICRODISK CAVITY INTEGRATION WITH INAS
QUANTUM DOTS: FROM AS-GROWN TO REGROWTH

A DISSERTATION
SUBMITTED TO THE DEPARTMENT OF APPLIED PHYSICS
AND THE COMMITTEE ON GRADUATE STUDIES
OF STANFORD UNIVERSITY
IN PARTIAL FULFILLMENT OF THE REQUIREMENTS
FOR THE DEGREE OF
DOCTOR OF PHILOSOPHY

Zhigang Xie

March 2005

© Copyright by Zhigang Xie 2005
All Rights Reserved

I certify that I have read this dissertation and that, in my opinion, it is fully adequate in scope and quality as a dissertation for the degree of Doctor of Philosophy.

Prof. James S. Harris (Principal Adviser)

I certify that I have read this dissertation and that, in my opinion, it is fully adequate in scope and quality as a dissertation for the degree of Doctor of Philosophy.

Dr. Glenn S. Solomon (Co-advisor)

I certify that I have read this dissertation and that, in my opinion, it is fully adequate in scope and quality as a dissertation for the degree of Doctor of Philosophy.

Prof. Yoshihisa Yamamoto

Approved for the University Committee on Graduate Studies:

Abstract

The growth of self-assembled quantum dots growth is a strain-driven phenomenon, usually taking place in lattice-mismatched epitaxial growth. Electrons and holes confined in these nano-scale man-made objects, give out atomic-like sharp optical transitions. This kind of emission can be used in quantum information processing if the optical extraction efficiency is high enough, which is possible by embedding QDs into a micro-scale optical cavity. This enhancement effect can be estimated as a Purcell effect, which is the largest when the cavity Q is as high as possible and the cavity volume is as small as possible. A microdisk cavity is one of the widely used microcavities in cavity-QED research. In this thesis, we discuss QD lasing in the smallest microdisk (1.8 μm) reported. From the cavity mode lines tuning through QD exciton lines, it approaches single QD lasing, usually a Purcell factor of 80 is required to achieve this goal. When the QD is at resonance with a cavity mode, a lasing threshold as low as 10A/cm², or 300nW for each disk is estimated. Another issue is also important for QD emission to achieve better coupling with the cavity mode, that is, spatial coupling. Therefore, we developed a regrowth technique to place QDs close to the anti-node of the microdisk whispering-gallery modes. Under our preferred growth condition with a long diffusion path for In adatom, the QDs will only appear at the disk edge. We notice an obvious size effect for this regrowth: on larger disk of 30 μm diameter, the QD linear density will saturate at 6/ μm ; while on smaller disks of 3~4 μm diameter, there are usually only 1~3 QDs in the whole disk plane. Our micro-PL shows a standard single QD emission signature, as well as a large splitting for the neutral excitons, with opposite linear polarization. This regrowth technique can provide sharp exciton peaks as well as a cavity Q of 4,000 for the small disks of 3~5 μm diameter.

This thesis is dedicated to my parents and my wife, Jianyang.

“Parent’s ages should be known, for joy on one hand, for fear on the other.”

——Confucius (Chinese Most Holy and Foremost Teacher)

Acknowledgements

Five years ago, I moved to Stanford. Here I found my favorite research and research group. First, of course I would like to thank Coach, Prof. Harris. Not mentioning of his knowledge and prestige in MBE society, he is always nice to students and creates a relax forum for all Harris students to benefit from. I will also thank the entire group of colleagues: Xiaojun Yu, Juxian Fu, Ke Wang, Xin Jiang, Mark Wistey, Seth Bank, Rafael Aldaz, Barden Shimbo, Luigi Scaccabarozzi, Vijit Sabnis, Chien-chung Lin... I also would like to thank Prof. Yamamoto and his group. Prof. Yamamoto is very generous to let me use his lab 25C, where I have done most of my optical measurement. His PhD students and postdocs, Charlie Santori, Hui Deng, Kai-mei Fu, David Fattal, not only provide help on the equipment, but also help me build up the skill with micro-PL measurement. I have not really got a chance to help back, here I sincerely thank their help.

I would especially express my thanks to Dr. Glenn Solomon, my co-advisor. To me, he is a bridge between the Harris and Yamamoto group. Bingyang Zhang, my closest partner for MBE growth, helps a lot for the machine maintenance. Without his help, the growth work would not be so smooth.

I would like to thank Prof. Hui Cao and her students, Wei Fang and Xiaohua Wu. During my several visits to Northwestern University, they not only offered help for measurements, but also provided help on my travel and stay. Also, I really enjoy discussing and working together with them.

Besides research, I really appreciate the help from Gail Creech. Gail makes everything going smoothly and handles all the paperwork. Also, I need to thank Paula Perron and Claire Nicholas. As an applied physics student, I really appreciate their help during my whole PhD life.

I would like to thank my parents. They did too much for me, especially my father. Although he was passing away from me forever, I think he would be very happy to see I get my PhD finally. Finally, I must thank my wife, Jianyang. Marrying her is my biggest achievement during my life at Stanford, if there is any. I always work overnight, fly off bay area and neglect her for a long time, but she always shows support.

Contents

Abstract	iv
Acknowledgements	vi
Chapter 1. Introduction.....	1
1.1. Spontaneous emission coefficient β and very low threshold laser	3
1.2. Enhancement of spontaneously emission in a microcavity — the weak coupling regime	6
1.3. Strong coupling of cavity mode with the dipole emitter.....	7
1.4. The outline of this thesis	9
Chapter 2. Semiconductor Microdisk Devices And FDTD simulation	11
2.1. Theory for the microdisk cavity: microdisk resonator and cavity mode	11
2.2. Microdisk fabrication and coupling.....	15
2.2.1. Microdisk without waveguide-coupling	15
2.2.2. Microdisk resonator with direct waveguide coupling.....	17
2.2.3. Microdisk with vertical waveguide coupling.....	19
2.3. FDTD simulation	23
Chapter 3. As Grown QDs Embedded inside Microdisk Sample...	35
3.1. Self-assmbled QDs growth	35
3.2. Mcrodisk fabrication.....	36

3.3.	Optical setup and typical PL results for high-Q microdisk.....	41
3.4.	Low-threshold QD lasing.....	45
3.5.	Towards single QD lasing.....	48
Chapter 4. Regrowth Dynamics of InAs Quantum Dots on the		
GaAs Circular Mesa and Partial Microdisk Cavities		
		53
4.1.	Circular features defined by optical lithography and chemical etching	53
4.2.	MBE regrowth on a circular shaped mesa	60
4.3.	MBE regrowth on a partial microdisk cavity.....	68
Chapter 5. Optical Measurement on Regrowth Samples		
		75
5.1.	PL from isolated QDs	75
5.2.	Large splitting in the neutral exciton emission.....	79
5.3.	Life time measurement of isolated QDs	85
5.4.	Whispering Gallery Modes in the regrowth cavity.....	98
Chapter 6. Future directions and conclusions.....		
		107
Appendix A. Microdisk Processing recipe.....		
		109
Appendix B. 3D FDTD Calculation and Output Code.....		
		112
Bibliography.....		
		123

List of tables

Table 2-1. The mode position and effective index for $TE_{m,1}$	26
Table 2-2. The mode position and effective index for $TM_{m,1}$	26

List of figures

Figure 1-1. A typical light emitting devices with an optical microcavity.....	4
Figure 1-2. The active media spectral alignment with the cavity modes. The low dimensional active media could be quantum well (2D), quantum wire (1D) and quantum dot (0D), (from left to right).	6
Figure 2-1. (left) microdisk resonator structure; (right) cylindrical coordinate.	12
Figure 2-2. The field distribution of TE_{m1} mode along the radial direction.	14
Figure 2-3. The edge emission profile of microdisk.....	17
Figure 2-4. An illustration of waveguide coupling with microdisk resonator.	19
Figure 2-6. Test run of my 3D FDTD calculation.	25
Figure 2-7. A Gaussian pulse centered at 900 nm is applied close to the left edge of the disk. The middle figure is the FFT of the original Hz pulse; the lower figure is the FFT of Hz at the same point after 6,000 time steps.	27
Figure 2-8. The field distribution after 5,000 time steps following application of a fixed frequency signal at a point close to the left edge.	27
Figure 2-9. Two-step simulation to find the resonant peak and field distribution in a circular disk with 2D FDTD simulation. The first set of figures is for a Gaussian pulse as a hard d source to get the spectrum filtered out by the microdisk cavity; the last figure is with a sine wave as a hard source with the frequency calculated from the first step.	29
Figure 2-10. The electromagnetic field distribution of $TE_{15,1}$ mode for a 1.8 μ m disk with a thickness of 200nm from 3D calculations. The grid size is about 20nm. The top view and cross section are shown.	30
Figure 2-11. This figure shows the spectrum of 3 different disks with the same thickness of 200nm. 1) 3 μ m disk with 45 degree tilted edge and complete undercut. 2) 1.8 μ m disk with 45 degree tilted edge and	

400nm undercut. 3) 1.8 μ m disk with straight edge and complete undercut. The blue arrow shows the positions of TE _{m,1} modes.	32
Figure 2-12. The mode profile for TE _{15,1} and TE _{16,1} and the edge is 45 degree tilted. The grid is 20nm. The top one is for TE _{15,1} mode and the bottom one is for TE _{16,1} mode. These disks have a diameter of 1.8 μ m and a thickness of 200nm.	33
Figure 3-1. A 1 μ m scale AFM image of the 1.9ML QDs with a growth temperature of 500 °C. We would expect see a dots density of 50/ μ m ²	36
Figure 3-2. SEM images of HBr-based etching with both side view and top view. (a) oxide-removal-limited regime; (b)interim regime; (c) oxidation-limited regime.	37
Figure 3-3. SEM images of the first-step-etch by (a)HBr and (b)HCl for disks with a diameter 3 μ m and above. HBr based etchants cause smooth and circular profile, while HCl based etchants cause rough and un-circular profile.	38
Figure 3-4. SEM images of HCl:HNO ₃ :H ₂ O=1:1:2 etching. (a) top view of a 2 μ m disk; (b) side view of a 2 μ m disk; (c) side view of a big disk showing there is a over-etch in the GaAs-AlGaAs interface. .	39
Figure 3-5. An SEM image of our 1.8 μ m disk. The undercut is roughly 0.5 μ m and the pedestal is about 0.8 μ m wide and 0.7 μ m high, very robust. The thickness of the disk is 150nm.	40
Figure 3-6. An SEM image of our 3.5 μ m and 4.5 μ m disk. The undercut is between 1 μ m and 2 μ m, far enough for high-Q microdisk. The shape is perfectly circular.	40
Figure 3-7. Comparison between top and side collection. All the data are collected at the same pumping power.	42
Figure 3-8. (a) PL spectrum shows the FSR of a typical 1.8 μ m microdisk, which is roughly 45nm. In the QD SE regime, there only exist two TE modes. (b) The mode positions along a row of 1.8 μ m disk. The neighboring disks have very close mode position (wavelength).	43
Figure 3-9. Power tuning curve for a single QD exciton peak and a cavity mode peak. The top figure is for the QD and the bottom figure is for the WGM.	44

Figure 3-10. A high-resolution PL spectrum shows a high-Q mode from a 3.5 μ m disk. The linewidth is about 0.067nm after de-convolution, which suggest the Q is 13,000 and above. The actual Q might be higher than this because absorption broadening, but it is beyond the spectrometer resolution. 45

Figure 3-11. the linewidth of the cavity mode reduces with a increasing of pump power. The insertion shows the PL at 3 different pumping power points: 15 μ W, 45 μ W and 120 μ W. The threshold here is corresponding to a power of 45 μ W..... 46

Figure 3-12. Lasing charistics of a cavity mode at a temperature of 40K. The top figure shows the linewidth narrowing and the bottom one shows the intensity dramatically increases after the threshold. 47

Figure 3-13. The WGM positions shift with temperature at low pumping power and high pumping power condition separately. A QD exciton peak shifting with temperature is also plotted for comparison. 48

Figure 3-14. High resolution PL data at different temperature. The red curve shows the trace of QD peaks shift with temperature. They roughly shift equal distance for the same temperature change. The cavity modes don't shift monotonically. 49

Figure 3-15. L-I curve for the cavity mode at different temperatures. 50

Figure 4-1. The left drawing shows the process flow for as-grown QDs integrated with microdisk; the right drawing shows the process flow for regrowth QDs integrated with microdisk. 54

Figure 4-4. Etching depth is too much. (a) the disk shape deviates from circular shape; (b) part of the GaAs layer extending out has been etched away; (c) the GaAs top layer almost completely gone (top view); (d) the GaAs top layer almost completely gone (side view). 57

Figure 4-5. An AFM image shows typical pinhole defects when the pre-loading etching solution is too diluted. 58

Figure 4-6. The choice of non-selective recipe will influence the regrowth results. (a) HBr based recipe; (b) HCl:HNO₃:H₂O=1:1:2; (c) H₂SO₄:H₂O₂:H₂O=1:8:80 (top view); (d)H₂SO₄:H₂O₂:H₂O=1:8:80 (side view). 59

Figure 4.7. Quasi non-selective profile depends on the AlGaAs layer thickness and aluminum concentration. (a) the edge is 45 degree tilted when the aluminum concentration is 70%; (b) the tilting angle of the

edge is reversed to $-45\sim-60$ degree, if the etching depth is over 600nm and the aluminum concentration is 80%. In both cases, the top GaAs layer thickness is 120nm.	60
Figure 4-10. Regrowth on mesa structures with different diameters.	62
Figure 4-11. Average linear density of QDs at the mesa edge. On Sample “A”, the etching depth is about 500 nm, while on Sample “B”, the etching depth is 1 μ m. On both samples, the linear density slightly increases with the decrease of the mesa diameter.	63
Figure 4-12. The QD linear density dependence on the crystal orientation. The QDs distribution is almost uniform along the mesa edge. However, owing to non-inversion symmetry, QD alignment with the edge is relatively poor between [110] and [1 -10] direction.	64
Figure 4-13. The QD linear density dependence on the tilt of the sidewall. The sidewall is about 80 nm wide in (a), 150 nm wide in (b) and 600 nm wide in (c). For all three samples with undercut, the GaAs top layer is about 100 nm thick.	65
Figure 4-14. Crystal facets show up at the edge of regrowth feature (post or disk). The growth temperature is 585 degree C.	66
Figure 4-15. (a) The CCD image of PL from several 15 μ m disk samples very close to each other. (b) A typical PL from the edge of a 25 μ m disk sample, the collection area is limited to 5 μ m. According to AFM or SEM observations, there should be \sim 50 QDs in the spectrum range of 890~940nm.	67
Figure 4-16. (a) SEM of the microdisk sample before regrowth, with a top layer thickness of \sim 50 nm and a diameter of 4 mm. (b) The microdisk sample after regrowth, with a total thickness of 200~250nm.	70
Figure 4-17. (a) An AFM image of 5 mm disk showing one QD at the disk edge. The QDs width and height are approximately 40 nm and 5nm, respectively. (b) An AFM image of the 30 mm disk, using the same scale, showing several QDs aligned at the disk edge. Insert: The SEM image of the disk cross-section shows the sidewall of the disk is 45° tilted. We denote the edge region as Region II and the non-edge region as Region I. (c) Plot of the function $f(R')$ versus R' , where $R'=R/\lambda$. (d) The	

QDs density versus the disk diameter. The linear QD density approaches 7.6 QDs/mm for large disks and zero for small disks. The line is the fitting result based on our model (see text).....	71
Figure 5-1. PL measurement setup.....	75
Figure 5-3. (a) PL spectrum from a 3 μ m diameter and 30 μ m disk, pumped by a cw 670nm semiconductor laser. The pump power is 1 μ W. (b) The 3 μ m diameter microdisk, pumped using a cw Ti-sapphire at 860nm, under different pump powers. (c) The pump power dependence for peaks “a” and “b”. (d) The PL spectrum of a typical QD and WGM. The insert shows the temperature-tuning curve of the QD and WGM.....	77
Figure 5-3. The PL intensity ratio between two orthogonally polarized exciton peaks from one QD. Peak a' is radially polarized, while peak a is tangentially polarized.	78
Figure 5-4. (a) A Photoluminescence (PL) spectrum taken from a disk sample A. The insertion shows the fine structure of a QD centered at 1.377 eV. (b) PL for disk sample B. similar signature exists for a QD centered at 1.383 eV.	81
Figure 5-5. The PL spectrum for a disk sample C at a temperature of 8K. (a) The sample is pumped into the quasi-continuous states from wetting layer fluctuations around the disk edge. (b) The sample is pumped with above band pumping.	83
Figure 5-7. (a) 7K Micro-PL measurement from disk 1 (3 μ m diameter). There are quasi-continuous states in the range of 860~885nm. With increasing temperature, emission is only at 882nm, possibly because all the carriers relax to the deepest confinement. (b) Micro-PL measurement from another disk, disk 2 (4 μ m diameter). Besides the quasi-continuous states in the range of 860~885nm, there are also distinct QD peaks in the long wavelength side of 890 nm.....	88
Figure 5-8. (a) Micro-PL measurement from the disk 3 (4 μ m diameter). Very similar to the disk 2, there is a QD peak at 887 nm. (b) PLE measurement with detection of the 897nm QD peak. The wavelength of the pump laser is tuned from 857 nm to 875 nm. The results show there are quasi-continuous states spatially close to the QD state. The sharp drop of the QD PL intensity at 850~860 nm is observed as the pump wavelength scans cross the wetting layer into the WL fluctuation region. When the pump	

passes 872 nm, there are no longer quasi-continuous states, accounting for the second drop of PL intensity.	90
Figure 5-9. (a) The large wavelength scale PL spectrum for disk 4 (3 μ m diameter). As with other samples, there is a broad quasi-continuous distribution of states between 860 nm and 885 nm, as well as several distinct QD peaks passing 890 nm. (b) A higher resolution scan for the QD peaks around 917 nm. Peak "a" is assumed to be the single exciton peak, and Peak "a2" and "a3" are assumed to be charged exciton peaks. (c) The SE decay curves under several combinations of pumping wavelength and sample temperature. The dash line on the left indicates the pump laser pulse. (d) A schematic band diagram of the global wetting layer, wetting layer fluctuations close to the edge, and the QD. The carriers repopulation between the QD and wetting layer fluctuations makes the observed mono-exponential exciton lifetime longer with increasing temperature.	92
Figure 5-10. Comparison between the lifetime measurements and rate-equation simulations for disk 4. The "dots" are from experiment measurement and the "line" is from the simulation. (a) The exciton (peak a) SE emission decay curve. (b) The charged exciton (peak a2) decay curve.	93
Figure 5-11. The fitted SE lifetime measurement results change with the temperature for disk 4. (a) The exciton. (b) One of the charged exciton (peak "a2").	96
Figure 5-12. SEM images of 5 μ m disk by regrowth. The top view shows the atomic flat surface and the side view shows the tilted edge due to the nature of MBE growth.	99
Figure 5-13. The cavity Q of different sizes of microdisk by regrowth in the same column.	100
Figure 5-14. PL spectrum for a 5 μ m microdisk, the left graph shows the FSR for the mode distribution pattern and the right graph shows the lasing at wetting layer with a pumping power of 10mW. ...	101
Figure 5-15. The temperature-tuning curve for the cavity mode peaks belonging to a 5 μ m microdisk. ..	101
Figure 5-16. The experiments of QDs tuning through cavity modes. The red line is the cavity mode position determined at a high pump power.	103
Figure 5-17. (left) the PL spectrum at a high power of 30 uW; (b) Two cavity modes shift with the temperature.	104

Chapter 1. Introduction

In recent years, the interest in microcavity masers and lasers has increased. The idea to use microcavities lies in several facts. One of them is when the cavity volume is reduced to about one wavelength cubed, or at most a few, only one optical mode will interact with the active gain medium. One most obvious advantage of having one or a few optical modes interacting with the gain medium is that very little power is carried away by spontaneous emission in spurious modes and hence the threshold power of microcavity lasers can be very low. In that case, the input power versus output power curve is ideally a straight line and the device quantum efficiency is close to unity.

The above issue looks more likely related to a cavity “size effect”. However, another issue is obvious when the cavity size shrinks to one wavelength cubed $(\lambda/n)^3$, that is, Purcell effect. Purcell [1] suggested 50 years ago that the spontaneous emission (SE) rate of radiating dipoles could be tailored by using a cavity to modify the dipole-field coupling and the density of available photon modes. This revolutionary concept is now fully established due to the experimental and theoretical development of cavity quantum electrodynamics (CQED). When the active media is located inside such a micro-cavity, the spontaneous emission can be enhanced or suppressed. If an ideal emitter is: 1) perfectly matched spectrally with the cavity mode, 2) located at a maximum of the electric field, and 3) with its dipole aligned with the local electric field, then this ideal emitter will experience an enhancement. The figure of merit takes the form proposed by

Purcell, $F_p = \frac{\tau_{free}}{\tau_{cav}} = \frac{3Q(\lambda_c/n)^3}{4\pi^2 V_{eff}}$. For a one-wavelength-cubed cavity, even with a Q of

1,000, we can expect the enhancement to be ~ 70 .

There are mainly two types of active media for semiconductor microcavities: quantum well (QW) or self-assembled quantum dots (QD). For the continuous distribution of QW medium, the spontaneous emission coupling efficiency β (defined as the ratio of spontaneous emission into the mode over all spontaneous emission) can be enhanced by the Purcell effects. However, the QW emission is indeed spectrally much broader than the resonant modes of the cavities, which weaken considerably the magnitude of the

Purcell effect. Nonradiative recombination at the sidewall is also a major subject of concern for the QWs, since it usually dominates the intrinsic modification of the carrier lifetime. Self-assembled QDs are quite different in this context. This is especially true when the active media is an isolated QD and coupled spectrally and spatially well with the cavity mode, and the coupling efficiency will be very close to 1[2]. This high efficiency provides the possibility for future novel devices working on quantum information processing. Also in this case, QD coupling with a high quality microcavity will be an ideal single-photon source with greatly approved extraction efficiency. Recently there is a member of publications for turnstile devices [3] [4] in this weak-coupling region.

This is for the condition of weak coupling, that is, the rate of the photon leaking out the cavity is much larger than the enhanced SE rate. This case is comparable to an over damped string. From the lifetime measurement, we can measure an exponentially decaying photon density. For standard InAs quantum dots, the SE decay lifetime will be about 500ps~1ns. Under the interaction of a microcavity, we can see lifetime reduction, for example, 1.05ns to 0.2ns[5], 0.9ns to 0.18ns[6]. However, when the cavity Q is high enough, that is, the rate of photon leaking out is comparable to SE rate, we would expect to see a totally different phenomenon. Still, in the example of InAs QDs, the SE rate is enhanced to ~10ps. First, it will be possible to see single QD lasing, which maybe the final goal of microcavity laser. Due to the Fermionic nature of laser, the requirement to achieve inversion needs very high Purcell effect and very low loss (high Q) cavity. A truly single quantum dot laser, as well as single trapped ion laser, single molecular laser are still big goals for cavity-QED research.

While, inside a very high Q microcavity, a damping oscillation-Rabi oscillation can potentially occur if the vacuum Rabi splitting, $2g$, due to a SQD exceeds the mean of the decay rates of the cavity, κ , and the quantum dot, γ . For macro cavities, $\kappa(=2\pi\nu/Q)$ usually exceeds γ . So the challenge is how to get as high as Q/V as possible. Once this criterion is satisfied, then the interaction between the QD and micro cavity goes from the weak coupling regime into the strong coupling regime. In that regime, exciton and photon will form a polariton and the bosonic nature of this system will suddenly make possible lasing without inversion [7]. The strong coupling regime used to be observed as Rabi

oscillations inside a large external cavity with a single atom or molecular. In semiconductor microcavities, the strong coupling between QW and cavity mode has been reported in Reference [8]. With improving epitaxial growth and processing techniques, now the strong coupling between QDs and all typical microcavities, such as micropost [9], microdisk [10] and photonic bandgap cavity [11] have all now been realized and reported.

1.1. Spontaneous emission coefficient β and very low threshold laser

The knowledge of the electromagnetic field around a microcavity allows one to calculate the quality factor Q of a resonant mode, which is defined as the ratio between the energy stored in the cavity and the energy emitted in one cycle. Microdisk resonators can be realized with a very high Q . Thus for a microcavity laser, the most important parameter is the spontaneous emission coefficient, β , of the lasing mode [12] [13]. The spontaneous emission coefficient of a given mode is defined as the ratio between the spontaneous emission rate of that mode, A_0 , and the total spontaneous emission rate.

$$\beta = A_0 / \sum_i A_i \quad (1.1)$$

Where the index 0 indicates the optical mode that will eventually lase, and the spontaneous emission lifetime is defined as

$$\tau_{sp} = 1 / \sum_i A_i \quad (1.2)$$

where A_i is the spontaneous emission rate of the active material into mode i .

Figure 1-1 shows a standard semiconductor light emitting devices with an optical microcavity. When the input is low, the device is working in the spontaneous emission (SE) regime and light exaction efficiency is quite low. However, when the input exceeds the threshold, there enough photons existing in the cavity to trigger amplified emission, so the device goes into the laser regime. No mentioning of the high exaction efficiency, the modulation bandwidth will be much higher in the laser regime for optical communication applications. A efficient device will requires a low threshold to reduce power consumption and improve thermal stability. Thus the problem is how to realize lasing with an ultra-low threshold.

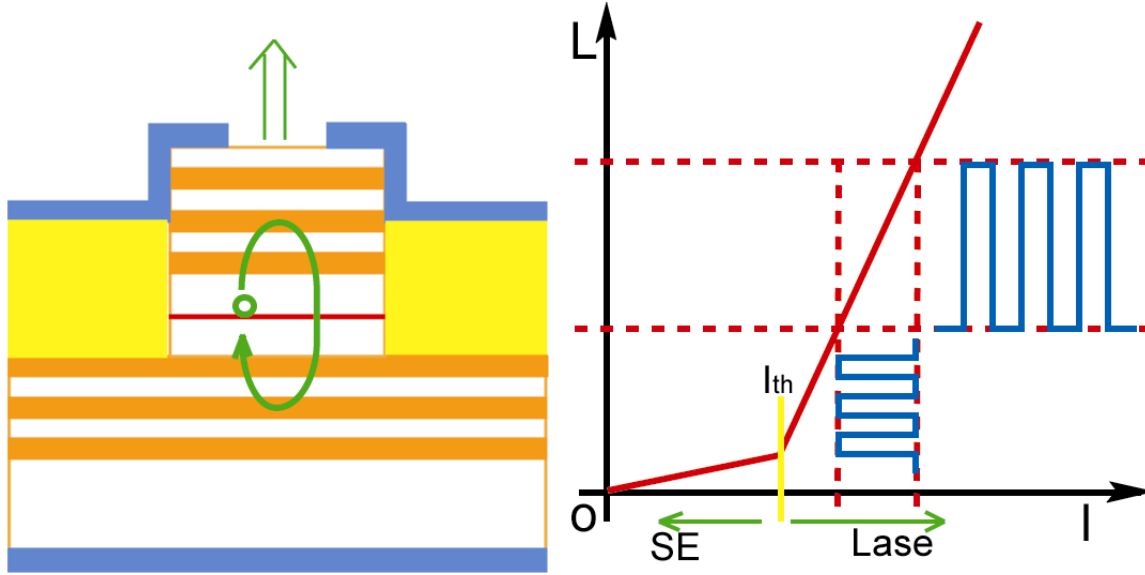


Figure 1-1. A typical light emitting devices with an optical microcavity.

From the rate equation analysis below, we will see why increasing β ($\beta \rightarrow 1$) will lower the laser threshold and improve dynamics response

$$\begin{aligned} \frac{dN}{dt} &= \frac{I}{qV} - \left(\frac{1-\beta}{\tau_{sp}} + \frac{\beta}{\tau_{sp}} \right) N - \frac{N}{\tau_{nr}} - \frac{gp}{V} \\ \frac{dp}{dt} &= -(\gamma - g)p + \frac{\beta NV}{\tau_{sp}} \end{aligned} \quad (1.3)$$

Where N is the free-carrier density in the active medium, p is the photon population in the cavity, and γ is the cavity decay rate, which depends on Q . Here we assume the electrical pumping case and I is the injection current. But we can get a similar result for the optical pumping case.

From Einstein's relationship between the spontaneous and stimulated coefficients, it is clear that for every mode, the spontaneous emission equals the stimulated emission when the average photon number in the cavity is unity. So we have

$$g = \beta V / \tau_{sp} (N - N_0) \quad (1.4)$$

The most widely used definition for the threshold current is that the net stimulated gain should equal the loss. By inspecting the rate eqn (1.3), we find it is equivalent to

$$\gamma = \frac{\beta V}{\tau_{sp}} (N_{th} - N_0) \quad (1.5)$$

and

$$N \approx \frac{I}{qV(1/\tau_{sp} + 1/\tau_{nr})} \quad (1.6)$$

$$\text{So we find the threshold pumping will be } I_{th} = \frac{q\gamma}{\beta} \left(1 + \frac{N_0\beta V}{\gamma\tau_{sp}}\right) \left(1 + \frac{\tau_{sp}}{\tau_{nr}}\right) \quad (1.7)$$

If we neglect non-radiative recombination ($\tau_{nr} \rightarrow \infty$), the threshold current will only depend on the first two terms. For a traditional semiconductor cavity, β may be in the order of 10^{-5} to 10^{-4} , and the second term is also close to 1. Thus we can have

$$I_{th} = \frac{q\gamma}{\beta} \quad (1.8)$$

For an ideal microcavity laser ($\beta \rightarrow 1$), with no nonradiative recombination, $I_{th} = q\gamma$. In such an ideal laser the only loss mechanism is photons emitted into the lasing mode. The photon emission rate is exactly the rate at which we must inject new carriers in order to compensate for the loss. Since the photon loss rate in this case is γp , which tells us that the mean photon number at threshold is unity for a truly ideal laser.

Reduction of the threshold current by increasing β can be viewed as a mixture of classical effects and cavity QED effects (we will discuss this in the next section). Shrinking the size of the microcavity can simply reduce the number of modes interacting with the active media. For the microdisk resonator we discussed, a high $\beta \sim 0.1$ can be achieved. In such a cavity, we can expect to see a very low lasing threshold for the microdisk laser. Besides, we will use low dimensional materials to increase the β by enhancing the spectral matching and overlapping between the cavity mode and active media. The active media in this dissertation will be quantum dots.

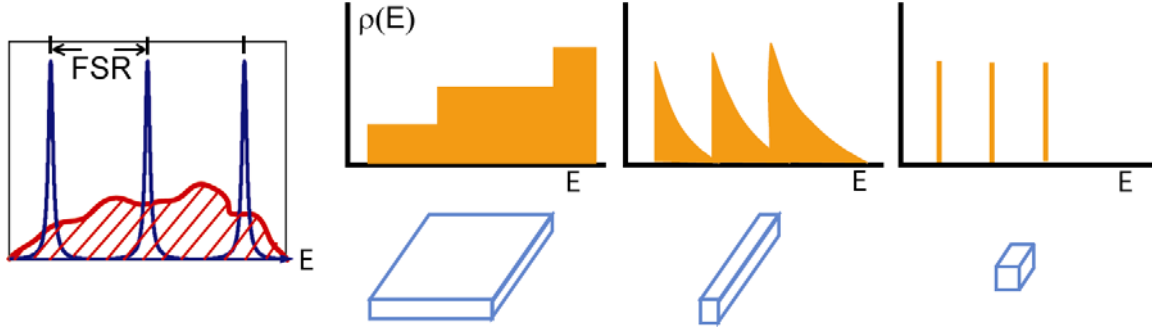


Figure 1-2. The active media spectral alignment with the cavity modes. The low dimensional active media could be quantum well (2D), quantum wire (1D) and quantum dot (0D), (from left to right).

1.2. Enhancement of spontaneously emission in a microcavity — the weak coupling regime

In 1946, Purcell first proposed a revolutionary concept to control the spontaneous emission (SE) rate of a quasi-monochromatic dipole by using a cavity to tailor the number of electromagnetic modes to which it is coupled. Later work on Cavity QED [14][15][16][17][18] has provided a firm theoretical and experimental basis for his idea and it became a major source of inspiration for the research activity since 1990. The ability to enhance the SE rate is the so called Purcell Effect.

Let's first consider a general electric dipole transition given by Fermi's golden rule

$$\frac{1}{\tau} = \frac{4\pi}{\hbar} \rho(\omega) \left\langle \left| \vec{d} \cdot \vec{\varepsilon}(\vec{r}) \right|^2 \right\rangle, \quad [19] \quad (1.9)$$

where $\vec{\varepsilon}(\vec{r})$ is the vacuum electric-field amplitude at location, \vec{r} , of the emitter and \vec{d} is the electric dipole. $\rho(\omega)$ is the density of vacuum states at the emitter angular frequency ω . However, if the emitter is put into a cavity, the final density states, $\rho(\omega)$, will be greatly modified and instead of being a constant value, it is given by a normalized Lorentzian in the cavity case. Thus at the resonance frequency ω_0 , the density of modes can be very high, depending on the quality factor of the cavity.

Purcell originally considered this enhancement of spontaneous emission in the “weak-coupling regime”. That is, a localized dipole (wavelength λ_e , linewidth $\Delta\lambda_e$) placed on

resonance with a single cavity mode (wavelength λ_c , linewidth $\Delta\lambda_c$, quality factor $Q = \lambda_c / \Delta\lambda_c$), since $\Delta\lambda_e \ll \Delta\lambda_c$, the escape time of SE photons out of the cavity is much shorter than the radiative lifetime and re-absorption is negligible. In the weak-coupling regime, the emitter feels a quasi-continuum of modes and the SE rate can be expressed using Fermi's Golden rule. A simple derivation shows that the SE rate in the cavity mode, referenced to the total SE rate in a homogeneous medium, is given by the Purcell factor, $F_p = 3Q\lambda_c^3 / 4\pi^2 n^3 V$, where n is the refractive index of the medium and V is the effective mode volume (V is given by the spatial integral of the vacuum field intensity for the cavity mode, divided by its maximum value). To get the maximum enhancement, given by the Purcell factor, the emitter must be on exact resonance with the cavity and located exactly at the antinode of the vacuum field, with its dipole parallel to the vacuum electric field. Thus the Purcell factor provides the maximum enhancement one can expect from an ideal cavity. However for a practical microcavity, the spontaneous emission enhancement can be expressed as

$$\frac{\gamma}{\gamma_0} = \frac{3Q(\lambda_c/n)^3}{4\pi^2 V} \frac{\Delta\lambda_c^2}{4(\lambda - \lambda_c)^2 + \Delta\lambda_c^2} \frac{|E(\vec{r})|^2}{|E_m|^2} 2\eta^2 = F_p g(\lambda) h(\vec{r}) 2\eta^2 \quad (1.10)$$

where γ_0 is the spontaneous emission rate of the dipole without the cavity, say, with isotropic vacuum field; $E(\vec{r})$ is the electric field amplitude of the cavity mode at the position of the dipole emitter; $E_m = (h\nu / 2\varepsilon_0 n^2 V)^{1/2}$ is the maximum value of the electric field amplitude. The first term, F_p , is the Purcell factor. The second term $g(\lambda)$ and the third term $h(\vec{r})$ describe the spectral and spatial matching between the dipole emitter and the cavity mode. The factor of 2 comes from the two-fold polarization degeneracy of the cavity mode. η describes the orientation match between the emitter dipole and the polarization of the cavity mode.

1.3. Strong coupling of cavity mode with the dipole emitter

When the interaction between the cavity mode and dipole emitter is large, we cannot use Fermi's golden rule to describe the spontaneous emission. When the cavity Q is large enough, the cavity lifetime will be very close to the intrinsic lifetime (given by the

spontaneous emission lifetime without a cavity) of the dipole emitter and strong coupling occurs. The strong coupling is characterized by a vacuum-field Rabi splitting and formation of dressed states.

There are two types of strong coupling, depending on the character of the emitter. Over the past decade, there have been extensive studies on strong coupling of quantum well excitons to photons in planar semiconductor microcavities. Transverse momentum conservation requires that a quantum well exciton state with transverse momentum, k_{\parallel} (parallel to the quantum well plane) interact only with the cavity photon state with the same k_{\parallel} . The strong coupling between these states leads to the formation of two new eigenstates, i.e., cavity polariton states. Due to the Bosonic character of the quantum well exciton, the Rabi splitting is basically independent of field intensity for weak excitation. If the emitter is a zero-dimension structure — i.e. Quantum Dots, we come to the vacuum Rabi splitting in the atom-cavity case. The quantum dot is like a two-level atomic system. It is intrinsically Fermionic. Its Rabi splitting is proportional to the square root of the intra-cavity photon number.

However, the strong coupling behavior for these two different types of emitter is very similar. As an example, we will present an estimation of how it is possible to achieve strong coupling in a QD-microcavity system.

The eigen-frequencies of the vacuum-field-induced dressed states of a single quantum dot in resonance with a microcavity mode are [20]

$$\Omega_{\pm} = \omega_0 - \frac{i}{4}(\gamma_c + \gamma_e) \pm \sqrt{g^2 - \left(\frac{\gamma_c - \gamma_e}{4}\right)^2} \quad (1.11)$$

where ω_0 is the transition frequency of the quantum dot. γ_c (γ_e) is the decay rate of the cavity mode (quantum dot intrinsic spontaneous emission) and g is the coupling constant of the quantum dot and cavity interaction:

$$g = \left(\frac{1}{4\pi\epsilon_0\epsilon_r} \frac{\pi e^2 f}{mV}\right)^{1/2} \quad (1.12)$$

where m is the free-electron mass; ϵ_0 (ϵ_r) is the vacuum (relative) permittivity; V is the effective cavity mode volume; f is the oscillator strength of single quantum dot.

The condition for strong coupling is $g > |\gamma_c - \gamma_e|/4$. We have two ways to achieve this goal: either increasing the cavity quality factor, Q (making $\gamma_c \rightarrow \gamma_e$), or decreasing mode volume, V . The microdisk resonator has very low mode volume ($\sim 0.2 \mu\text{m}^3$). The active media (quantum dots) has a linewidth of $50 \mu\text{eV}$. When the cavity Q reaches a value of 20,000, then $|\gamma_c - \gamma_e| \rightarrow 0$. Thus in the microdisk resonator, we can achieve strong coupling between active media (i.e. Quantum Dots) and the cavity mode. As Q increases, the QD microdisk system experiences a crossover from the weak-coupling regime to the strong coupling regime. In the strong coupling regime, the real part of the energy splits. This is a manifestation of the vacuum Rabi splitting.

It is well known that “Quantum Entanglement” is critical to quantum information manipulation, such as quantum cryptography and computation. The quantum dot, which is strongly coupled to a cavity mode, can be used as a single quantum bit (qubit) in quantum logic gates.

1.4. The outline of this thesis

This thesis will discuss theoretical and experimental work about the coupling between a high- Q microdisk cavity and self-assembled InAs/GaAs QDs. As an outline of this thesis, I will first introduce the microdisk cavity, theoretical background and applications. I then discuss in detail the traditional ways of high Q microdisk cavity coupling with as-grown QDs, including the methods to fabricate microdisks and QDs growth. In Chapter 3, I report an ultra-low threshold microdisk laser and the threshold lowering by QD-cavity mode resonance. In Chapter 4, I describe a new method of growing QDs: patterned MBE regrowth. At first, I describe the QDs regrowth mechanism, such as In adatom long distance diffusion driven by the surface chemical potential, and the QD alignment with the crystal orientation. Gradually we introduce the regrowth from the mesa substrate to the partial microdisk cavity. Using this technique, InAs QDs will concentrate only at the outer edge of the disk where the electric field of the cavity mode is highest and promises the highly possible spatial matching of gain media and optical mode. Single QD PL as well as the cavity Q is measured by filtered spontaneous emission. Together with the lifetime resolved PL measurement, our optical measurement proves that QDs by regrowth

have as sharp exciton peaks as as-grown QDs, except for a large splitting, possibly due to the asymmetric strain distribution around the QD or a structural asymmetry from the diffusion process. Our microdisk cavity achieved by regrowth has a cavity Q of 4,000 for the small disk of 3~5 μm . In the last Chapter, I provide a summary and the possible directions for future research. The recipe to make high- Q , as-grown microdisks and regrowth microdisks both are included. Also my code for FDTD simulation based on Matlab is attached as an Appendix.

Chapter 2. Semiconductor Microdisk Devices And FDTD

simulation

Microdisk and microring waveguides, resonators and lasers are important optoelectronic devices and efficient active and passive devices, because of their high Q circular structure. Many practical passive devices incorporating microdiscs and microrings have been demonstrated recently, including channel dropping filters, WDM demultiplexers, and notch filters [21][22][23][24][25]. Despite the fact that vertical cavity surface emitting laser (VCSEL) or horizontal cavity edge emitting lasers are the dominant semiconductor lasers for most applications, some interest is now focused on circular lasers, due to the demonstration of ultra small microdisk lasers. There are a lot of advantages to these kinds of lasers, such as narrow-band and single mode operation, sub-milliamperere threshold current, quality factors on the order of thousands, and a high spontaneous emission coupling factor. The small size, low power consumption, and light propagation parallel to the substrate plane make these devices an appropriate choice as waveguide-coupling active devices for integrated optical applications.

The intrinsic character of the microdisk is its high Q and low mode volume. Because of these elements, it may be possible to get very fast spontaneous emission, a thresholdless laser or vacuum Rabi oscillations for quantum computation. I will first introduce the basic character of the microdisk resonator, and then from Cavity QED perspective, explain why microdisks have such capabilities. After this, I will introduce the real device fabrication and waveguide-coupling issues.

2.1. Theory for the microdisk cavity: microdisk resonator and cavity mode

The microdisk provides a resonant cavity with a dimension comparable to the lasing wavelength, so there exist only a few optical modes that are coupled with the excitation states of the active gain region materials. Unlike a normal vertical cavity surface emitting laser, a microdisk does not need a large number of DBR mirror pairs to achieve

high reflectivity. The laser beam bounces around the disk edge and undergoes total internal reflection at the edge. The strong index difference between the guiding layer and surrounding cladding layer provides vertical optical confinement. In this way, a very high Q (2,000 to 20,000) can be achieved. The optical modes in such a microdisk are called whispering gallery modes (WGM). This is the reason that microdisks can provide a single mode laser with very narrow bandwidth and high Q.

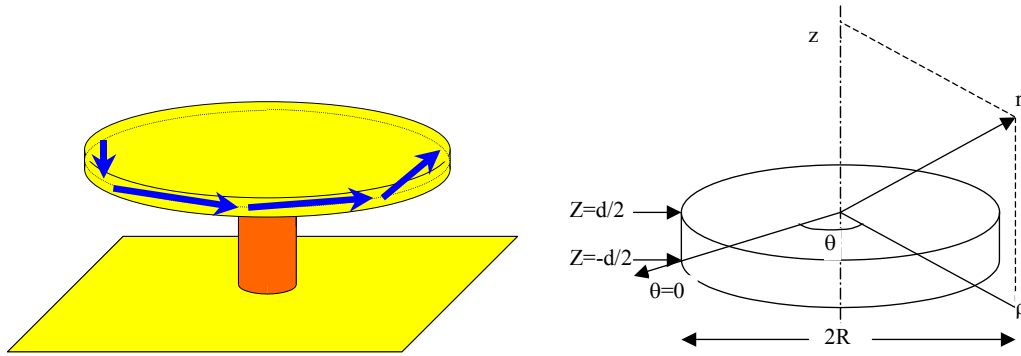


Figure 2-1. (left) microdisk resonator structure; (right) cylindrical coordinate.

In an optical mode calculation, the real structure of a microdisk resonator is usually simplified as a dielectric disk with optical gain. Because of the relatively low symmetry of the microdisk system, we cannot reduce the three dimensional Maxwell equation to a one-dimensional problem. In a continuous dielectric medium with no free electrical charges and no current sources, the electromagnetic field of an optical wave can be written, in cylindrical coordinates, as follows [26]:

$$\begin{cases} H_z = k^2 g + \frac{\partial^2 g}{\partial z^2} \\ H_\rho = \frac{\partial^2 g}{\partial \rho \partial z} + \frac{k_0}{\rho} \frac{\partial f}{\partial \theta} \\ H_\theta = \frac{\partial^2 g}{\rho \partial \theta \partial z} - k_0 \frac{\partial f}{\partial \rho} \end{cases}, \quad \begin{cases} E_z = i\omega\mu_0 \left(f + \frac{1}{k^2} \frac{\partial^2 f}{\partial z^2} \right) k_0 \\ E_\rho = i\omega\mu_0 \left(\frac{k_0}{k^2} \frac{\partial^2 f}{\partial \rho \partial z} + \frac{\partial g}{\rho \partial \theta} \right) \\ E_\theta = i\omega\mu_0 \left(\frac{k_0}{k^2} \frac{\partial^2 f}{\partial \rho \partial z} - \frac{\partial g}{\partial \rho} \right) \end{cases} \quad (2.1)$$

where k and k_0 are moduli of the wave vector in the medium and in free space, respectively. f and g are two scalar functions which satisfy the following wave equation:

$$(\Delta + k^2)[f, g] = 0 \quad (2.2)$$

The real electromagnetic field is the addition of different guided modes and nonguided modes. The combinational coefficient of these modes is decided by the continuity condition of the electromagnetic field at the interface of the microdisk. This is the general approach of solving disk-like resonators. However, due to the very small thickness of the microdisk resonator, we may assume that for optical waves with wavelengths within the spontaneous emission spectral region, only one TE ($E_z = 0$) polarized and one TM ($H_z = 0$) polarized guided mode can exist (typically for the radius $R \sim \lambda$ and thickness $d < \lambda/2n$). For an m th order TE mode, $TE_{m,l}$, we have $f=0$ and:

$$\begin{aligned} g &= C_m \tilde{n}^2 \int dp [s^2 K_m(k_0 s R)]^{-1} G(p) K_m(k_0 s \rho) e^{ipk_0 z} e^{im\theta} \\ (s^2 &= p^2 - 1) \text{ for } \rho > R; \text{ and} \\ g &= C_m [J_m(k_0 \tilde{n} R)]^{-1} J_m(k_0 \tilde{n} \rho) e^{im\theta} g(z) \\ \text{for } \rho &\leq R \end{aligned} \quad (2.3)$$

$$g(z) = \begin{cases} \cos(\sqrt{n^2 - \tilde{n}^2} k_0 z), & |z| \leq \frac{d}{2} \\ \cos(\sqrt{n^2 - \tilde{n}^2} k_0 \frac{d}{2}) \exp[-k_0 \sqrt{\tilde{n}^2 - 1} (|z| - \frac{d}{2})], & |z| > \frac{d}{2} \end{cases} \quad (2.4)$$

$$(n^2 - \tilde{n}^2)^{1/2} \operatorname{tg}\left[\frac{k_0 d}{2} (n^2 - \tilde{n}^2)^{1/2}\right] = (\tilde{n}^2 - 1)^{1/2} \quad (2.5)$$

There are three approaches to solve $TE_{m,l}$:

- 1) Assume $J_m(k_0 \tilde{n} R) = 0$ for whispering gallery modes using these equations; [27]
- 2) FDTD calculation;
- 3) Conformal transformation and WKB approximation.

We can use a similar approach to solve the TM mode. However, it turns out that by numerical calculation the effective index for TM polarized modes, \tilde{n} , in a very thin slab waveguide is only slightly greater than 1. Thus very high slab threshold optical gain is expected for these modes. In practice, such large optical gain can never be approached. The light emitted from a microdisk is always nearly completely TE polarized. Thus, we

only need to consider the TE polarized modes in a microdisk resonant cavity. After solving an eigen-value problem, we can explicitly write down all the components of the electromagnetic field. In contrast with a vertical cavity laser case, the energy flux of the microdisk is in the in-plane direction.

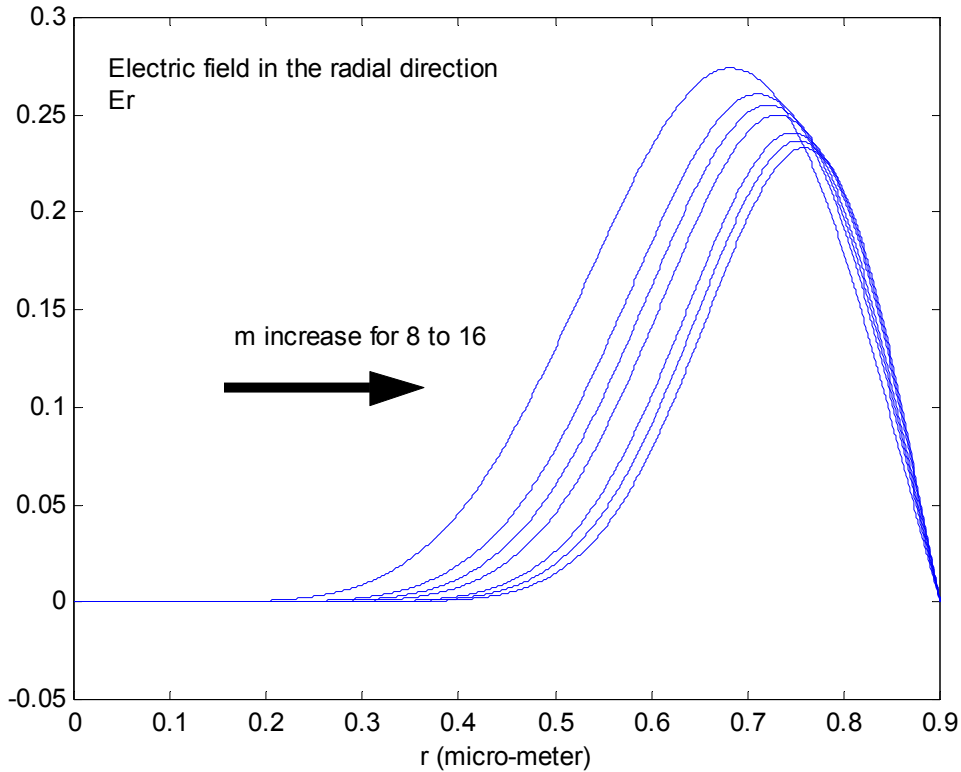


Figure 2-2. The field distribution of TE_{m1} mode along the radial direction.

So, based on these assumptions a simple calculation provides the effective index and allowed wavelength in the cavity. We can express the quality factor Q (due to radiation or bending loss) as:

$$Q = b \cdot \exp(2mJ), J = \tanh^{-1}(S) - S, \text{ and } S = \sqrt{1 - 1/n_{\text{eff}}^2} \quad (2.6)$$

where $b \sim 1/6.5$. This formula is from an estimation of tunneling rates using the WKB approximation [27]. Thus, we can see that, (1) a higher n_{eff} will lead to a higher Q and a lower threshold, which is the reason we only see TE modes instead of TM modes, (2) the higher index of m means the field intensity will be closer to the edge and the incidence angle is larger so the radiation loss is smaller, and (3) the FWHM of the edge-emission

angle is estimated to be $2/\sqrt{m}$. Thus for higher order of TE_{ml} , we get a narrower edge-emission angle. However, the estimation of Q based on eqn (2.6) will be on the order of 10^9 for the first order TE modes, which is not practical since in reality, the cavity Q is decided by the sidewall roughness.

2.2. Microdisk fabrication and coupling

2.2.1. Microdisk without waveguide-coupling

High- Q microdisks using QWs or QDs have been reported over the past decade [28] with a cavity Q of 5,000-20,000. In 2000, H. Cao and G.S. Solomon reported a very high Q microdisk laser [29]. In their structures, quantum dots were embedded as the active media into microdisk cavities. A cavity with a Q of 5,000 was achieved. The device fabrication begins with molecular beam epitaxy (MBE) growth of the QDs. The structure consists of a GaAs buffer, 500 nm $Al_{0.7}Ga_{0.3}As$, 45 nm GaAs, 3 monolayer InAs (transition into quantum dots), and 45 nm GaAs. The photoluminescence spectrum of quantum dots at 77K is centered around 970 nm with a full width at half maximum (FWHM) of 20 nm.

The microdisks are fabricated by electron beam lithography and two steps of wet etch. 100 nm silicon dioxide (SiO_2) is deposited on the wafer and used as the etch mask. Disk patterns are defined by electron beam lithography with negative resist. The pattern is transferred from the e-beam resist to the SiO_2 etch mask by reactive ion etch. It is followed by two steps of wet etch. The first step is a nonselective etch, i. e., the sample is nonselectively etched down to the GaAs buffer layer in a dilute water solution of phosphoric acid (H_3PO_4) and hydrodioxide (H_2O_2). The second step is a selective etch of a dilute solution of hydrofluoric acid which etches the $Al_{0.7}Ga_{0.3}As$ without attacking either the GaAs layers or InAs quantum dots. With careful control of the etch time, microdisk GaAs structures are formed on top of AlGaAs pedestals. In Reference [29], a high-resolution SEM image shows a $3\mu m$ microdisk following this recipe. The edge of the microdisk is quite smooth, which is the key to achieve a high quality factor, Q .

Although semiconductor lasers built with such microdisk cavities can have very high Q and very low threshold, there is a problem of coupling the light emission out. To analyze

the emission spacing pattern, we need to go back to Section 2.1. The requirement that the field wave vector components parallel to the dielectric sheet edge must be equal across the sheet edge results in total internal reflection at a sheet edge for incident angles larger than $\sin^{-1}(1/n_{eff})$, where n_{eff} is the velocity of light divided by the phase velocity in the thin dielectric sheet. While the laser beam bounces around the edge, a bending loss occurs (similar to the bending loss of optical fibers), and the lasing emission is from this bending loss. The loss is tangential and into the full 360° azimuthal angle. This bending loss can be analyzed using the WKB approximation and conformal transformation. Two mode numbers should be reintroduced for the field in the disk: m corresponds to the azimuthal angle, ϕ , in cylindrical coordinates, and a radial number, n , where $n-1$ denotes the number of nodes along the radius, r . The factor of $\exp(im\phi)$ in the wave equation solution is associated with a repulsive angular momentum potential that varies as m^2/r^2 . This repulsive potential, in combination with the attractive potential within the dielectric disk, combine to form a trough potential just inside the disk edge and a tunneling barrier just outside the disk extending to a radius, $r \approx m\lambda/2\pi \approx n_{eff}R_D$, where R_D is the disk radius. Thus waves propagating outward from the disk into the surrounding low index region are evanescent while tunneling out to a radius, $r \approx n_{eff}R_D$, and then propagate freely outward from the disk. An intensity profile of a whispering-gallery mode, the evanescent region and the free-propagation region can be found in Reference [30], where an approximate calculation of the intensity pattern for an $m=8, n=0$ whispering-gallery mode is shown corresponding to the plane of a 2- μm -diameter disk.

A perfect disk mode emits radiation into a relatively narrow range of angles about the disk plane compared with the diffraction angle associated with the disk thickness. This angle narrowing of the whispering-gallery mode emission is the result of the tunneling barrier described above. The full width half maximum of the edge-emission angle is estimated to be $2/\sqrt{m}$ ($\approx 23^\circ$ for a 5- μm -diam disk).

The light emission from a microdisk is almost focused in the in-plane direction, so only under special circumstances, i.e. as a flat-panel display cell, a microdisk can be used directly as a light-emission source. Most research groups did think about some ideas of increasing the light emission into “useful direction”. Cylindrical symmetry implies that

the field mode functions are characterized by a factor $\exp(im\phi)$ with a mode degeneracy of two (M and $-M$). Any defect around the circumference of the disk will remove this degeneracy. So if we change the microdisk from a circular shape into elliptical shape, this degeneracy is broken and light emission will focus along the long-axis direction. One group built a structure with two microdisks stacked together in the vertical direction and also with vertical optical coupling [31][32]. The bottom disk has a perfect circular shape and the top one has a defect on the edge (made by ion-milling). Thus light-emission at the defect is greatly increased, while at other locations, it is greatly suppressed.

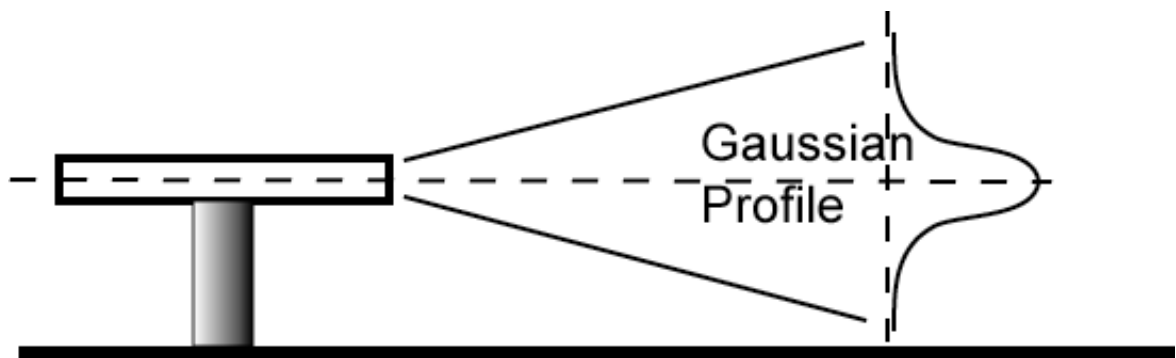


Figure 2-3. The edge emission profile of microdisk.

2.2.2. *Microdisk resonator with direct waveguide coupling*

We have cited some endeavors where research groups have directed at increasing the direct light emission from a microdisk. In principal, a microdisk laser cannot compete in most useful properties with more conventional lasers with horizontal or vertical cavities. However, intrinsically, a microdisk laser has advantage over these other laser cavities in optical VLSI circuits because of its compact size, extremely low threshold and ease of coupling with waveguides. Also, the active devices can be relatively easily pumped electrically or optically. For the optical pumping case, the pumping light can be either top injection or via side waveguide coupling, and we can always use waveguide to extract light out. Regarding microdisk coupling issues, there have been a lot of discussions for passive devices, but similar results can be applied to active device.

It is already well known that optical ring and disk resonators are useful components for wavelength filtering, routing, switching, modulation, multiplexing and demultiplexing applications. These compact high-index-contrast semiconductor disk resonators have attracted much attention because of negligible bending losses, large longitudinal mode spacing and their potential for high-density integration with other semiconductor devices. For active devices, the wide FSR (free spectral range) can yield single-mode operation well above threshold. To obtain light output, these disk resonators are coupled to directional couplers via a very small gap. For example, for a 3- μm -diam microdisk with emission at 900 nm, typically the gap should be as small as 100nm. Because of this small dimension, e-beam lithography is utilized to make such a structure. The low finesse that results from such strong output coupling is compensated for by the high gain in these active devices. Nanofabrication techniques now allow the realization of semiconductor microcavity disk resonators with evanescent wave coupling to submicron-width waveguides across submicron-width air gaps. With high-quality etching, the scattering losses can be kept low enough to achieve simultaneously a high finesse. In addition to the considerable body of experimental work, a number of designs have been theoretically modeled using finite-difference time domain (FDTD) calculation [33].

Mechanisms that can affect the Q of microdisk resonators are intrinsic material absorption, radiation loss caused by waveguide bending and surface roughness scattering, and coupling from the cavity to the adjacent waveguides. In addition to cavity Q and finesse, the FSR is also a very important parameter. The submicron width and large lateral index contrast of the semiconductor waveguides leads to significant optical waveguide dispersion. The impact of this is illustrated with the following equation for the FSR between the m th and $(m+1)$ th longitudinal modes.

$$\Delta\nu_{FSR} = \frac{c}{\pi} \left\{ \frac{m+1}{d_{eff}(\nu_{m+1})n_{eff}(\nu_{m+1})} - \frac{m}{d_{eff}(\nu_m)n_{eff}(\nu_m)} \right\} \quad (2.7)$$

where n_{eff} is the effective index of the waveguide mode and d_{eff} is the effective disk/ring diameter of the micro-ring or disk. For a disk with a relatively large diameter d , negligible waveguide dispersion can be expected, so eqn (1.6) can be simplified to

$$\Delta\nu_{FSR} = \frac{c}{\pi} \frac{1}{dn_{eff}}. \text{ With a diameter as small as } 5 \mu\text{m}, \text{ the FSR can be as wide as } 6 \text{ THz (50}$$

nm) in the optical communication wavelength. With a typical gain spectral width of active devices, it is very easy to achieve single-mode operation well above threshold.

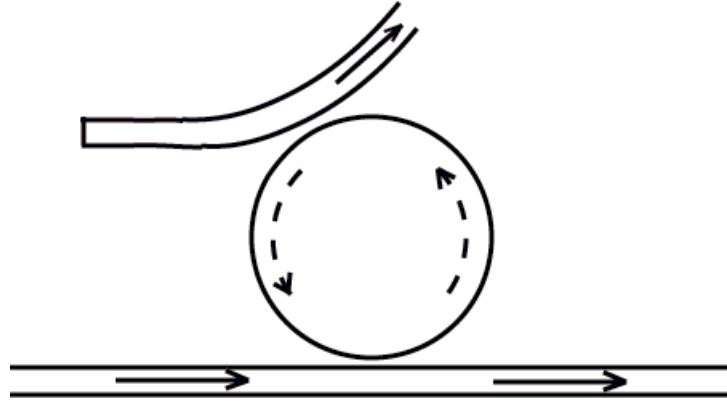


Figure 2-4. An illustration of waveguide coupling with microdisk resonator.

A SEM image in Reference [34] shows a 10 μm -diameter disk coupled to two straight 0.5 μm -wide waveguides. The fabricated gap widths are 0.1 μm . The resonator patterns were created on PMMA with electron-beam lithography. Using reactive ion etching, the PMMA mask was transferred to an underlying SiO_2 layer to provide a more durable mask. The AlGaAs/GaAs was then etched using chemically assisted ion-beam etching with chlorine and argon process gases. The resonators and input/output waveguides, as seen in the SEM images, are defined and isolated from the rest of the sample by etching a 1 μm -wide trench (the dark regions in the images).

2.2.3. *Microdisk with vertical waveguide coupling*

The concept of directional coupling by waveguide is straight forward and widely used for passive devices, but not ideal for active devices. The reason is simple: since the resonator cavity and waveguide are at the same level, we cannot isolate the design of the active device and the coupling of the passive waveguide.

Recently, K. Djordjev and coworkers [35][36][37][38] presented a high-Q vertically coupled microdisk resonator based on the InP materials system. Vertical coupling is

chosen because it offers two major advantages compared to the lateral geometry, namely the following: 1) the coupling coefficient can be precisely controlled by epitaxial growth and 2) the material composition of the waveguides and resonator can be optimized and grown independently. The latter advantage facilitates the design of active microdisk devices—ON/OFF switches, modulators, and microdisk lasers. The InP system also allows the incorporation of gain or electro absorption regions into the microdisk cavity suitable for operation in the communication window around $\lambda=1.55 \mu\text{m}$. In a real wavelength-division-multiplexing (WDM) system, active microdisk devices are required to correct for fabrication imperfections and add additional functionality.

Because of the low index contrast of the InGaAsP/InP system, wafer-bonding techniques are used to fabricate the vertical coupling structure. There are two types of wafer-bonding techniques: polymer wafer-bonding using BCB and a thermal wafer-to-wafer bonding technique. The first one applies strain to the structure, and also the polymer is an insulating material, which is not acceptable for the design of active devices. Using the second method, the resultant structure is thermally stable and strain free and interface exhibits ohmic electrical conduction. This Vertically coupled microdisk with a post improves the mechanical stability and current/field uniformity.

The corresponding epi structures were grown with low-pressure metal-organic chemical vapor epitaxy (MOCVD) on a (001) InP substrate. Epitaxial layer growth is followed by optical lithography and etching. Figure 2-5 shows the process flow chart. 100 nm SiN_x is used as a dielectric mask throughout the process and the patterns are transferred from the photoresist to the SiN_x layer with a low pressure (10 mtorr) RIE CF_4 plasma. The dry-etching process was optimized leading to negligible mask erosion and extremely smooth sidewalls. In this way, the waveguide/post pattern was transferred to the SiN_x mask. The waveguide width was $0.7 \mu\text{m}$ below the disk and adiabatically tapers to $3 \mu\text{m}$ for better coupling efficiency to a lensed fiber. The width of $0.7 \mu\text{m}$ was chosen to assure phase matching to the fundamental disk mode and also this is the minimum linewidth achievable with the optical contact mask aligner. The waveguides were dry etched to a $1.5\text{-}\mu\text{m}$ depth.

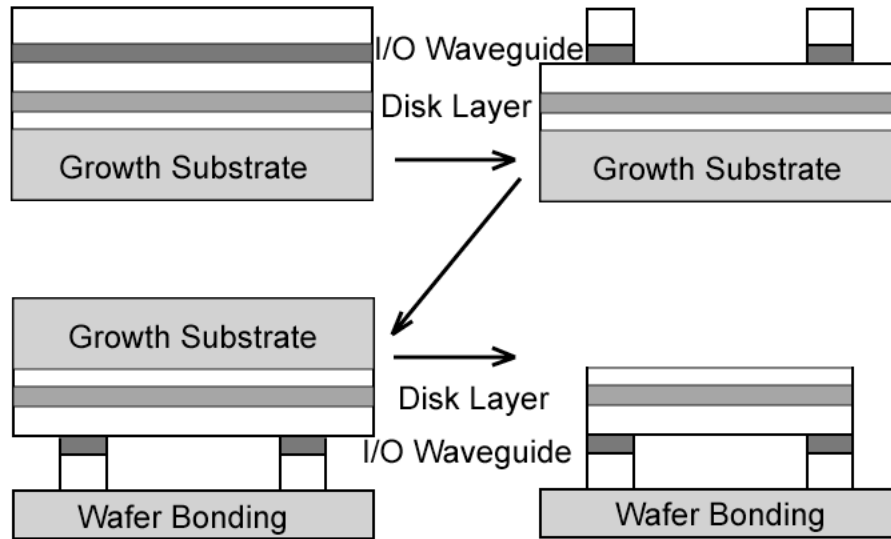


Figure 2-5. Microdisk resonators built by thermal wafer bonding technique. Process flow chart.

Second, the whole structure is flipped over and thermally bonded to another InP transfer wafer. To assure “perfect” bonding between both wafers, a critical step is the sample cleaning to remove particles and organic residue. The wafers were bonded in a H_2 atmosphere at $550\text{ }^\circ\text{C}$. A stress-free, thermally stable ohmic interface was obtained without degradation in the material quality.

The third step is the substrate removal. The samples were mechanically polished and the remaining InP from the original substrate was completely removed by selective chemical wet etch, which stops at the InGaAs etch-stop layer. This layer is then removed by another selective etchant. At this point, the top disk-cladding layer is exposed for further processing.

The most critical step in fabrication is the disk pattern alignment relative to waveguide and etching. Misalignment of the disk mesa with respect to the I/O waveguides will lead to asymmetric coupling and significant decrease of the transmission contrast ratio. For this purpose, a small area around the sample edge was etched down to the waveguide pattern, which makes the waveguides, the posts and the alignment marks defined with the first dry etch visible. The disk mesa was successfully aligned to this alignment mark and dry etched so that $0.1\text{-}0.3\mu\text{m}$ of the InP separation layer was left unetched. Optical tests

showed the power coupling coefficient is around $\kappa = 4\%$ and quality factor Q as high as 7000 for 12- μm radius disks.

Microdisks are widely used both as passive and active devices in optoelectronics. Passive devices have many limitations when considered for incorporation into large-scale systems using a fixed manifold of wavelengths. Their inherent wavelength selectivity places unrealistic demands on fabrication uniformity and reproducibility, and their temperature sensitivity suggests that a static system design would be thermally unstable. For these reasons alone, active resonator devices with tunable elements are more suitable for future applications. Active devices also enable switching and tuning elements to be incorporated into an optical circuit that greatly increases the functionality of such circuits. Furthermore, with slight modifications of the device design, one can easily envision that the same basic structure can be used to incorporate tunable lasers, detectors, and modulators into complex systems.

In this session, passive and active microdisk resonators are introduced from the basic principle of a cavity model for fundamental scientific research to future practical applications. The microdisk has a very large quality factor, Q , low mode volume and can have a very large spontaneous emission coefficient (β close to 1). Based on these merits, the microdisk resonator has the potential to outperform other cavities in three applications: 1) quantum information processing in the strong coupling regime; 2) very fast and thresholdless spontaneous emission or very low threshold microdisk lasers for optical VLSI, where compact size and low power-consumption are very important; 3) other active and passive optical elements, such as modulators and electroabsorption devices for future optical VLSI applications. We introduce three different schemes for microdisk coupling structures: 1) a direct emission structure, 2) a lateral and directional coupling waveguide-resonator structure, and 3) a vertical coupling waveguide-resonator-coupler structure. Besides improving the device performance, such as Q , FSR and finesse, we can expect more functional microdisk-like possibilities to be developed, such as mechanical and electrical tuning of the resonant wavelength. We believe, active microdisk resonator will be of great importance in cavity-QED research and future

optical VLSI circuit designs. For the remainder of this thesis, I will narrow down the concept to isolated upstanding disk with QDs embedded inside the disk for cavity-QED research. In our research, direct optical pumping is used and top or side collection is applied.

2.3. FDTD simulation

The calculation of electro-magnetic fields in complex structures is a well-developed field based on discretization of Maxwell's equations. This is especially true for the application with free-space and metal boundary conditions. However, the application of this technique to photonic crystals has difficulties due to the lack of appropriate boundary condition techniques. Recently, propelled by the development of high-speed computer and corresponding breakthroughs in perfectly matched layer (PML) boundary techniques, the finite difference time domain (FDTD) techniques are widely utilized in photonic device designs and simulations. Here, I calculate the cavity mode of a microdisk with a diameter of 1.8-micron meter (in the x-y plane) and a thickness of 100nm (in the z direction), as an example using this technique. The optical wavelength of interest is around 900 nm, and the cavity material is GaAs ($n=3.5$). In the z- direction, confinement is provided by the air-GaAs index contrast. In the x-y plane, the confinement is described by whispering gallery modes (WGM). With the above size, a diameter of λ and a thickness of $\lambda/3n$, normally only one TE and one TM mode can exist in the full spectrum of the active media. I utilized FDTD simulations to understand whisper gallery modes in the microdisk cavity better and compare this calculation with other simplified or more analytical techniques.

This calculation is a 3D FDTD calculation, using Cartesian coordinates and split field PML boundary conditions. The grid was $120 \times 120 \times 50$ and about 180,000 time steps are required to figure out the cavity Q ($\sim 3,000$). Basically one run of such a FDTD calculation will take several days or even longer. Thus I used this 3D FDTD to get the approximate position of the resonant mode and field distribution. It is technically possible to use a 2D FDTD calculation to figure out the Q and accurate mode pattern (distribution). Given that the z-distribution of field is known, it is possible to use the

concept of “effective index” in the x-y plane calculation. Thus the 3D problem is separated into a 1D (vertical confinement by refractive index contrast) + 2D TE or TM WG mode calculation. Since the electric dipole is usually in the x-y plane, TE modes are most interesting. The 2D calculation provides sufficient accuracy when the effective index is large enough, which is the case for a GaAs microdisk.

I use three-dimensional time-domain Maxwell’s equations for Berenger’s split-field PML. In three dimensions, all six Cartesian field vector components are split and according to Reference [39], the modified Ampere’s Law is given by

$$\begin{aligned}
(\varepsilon \frac{\partial}{\partial t} + \sigma_y)E_{xy} &= \frac{\partial}{\partial y}(H_{zx} + H_{zy}) & (\varepsilon \frac{\partial}{\partial t} + \sigma_z)E_{xz} &= -\frac{\partial}{\partial z}(H_{yx} + H_{yz}) \\
(\varepsilon \frac{\partial}{\partial t} + \sigma_z)E_{yz} &= \frac{\partial}{\partial z}(H_{xy} + H_{yz}) & (\varepsilon \frac{\partial}{\partial t} + \sigma_x)E_{yx} &= -\frac{\partial}{\partial x}(H_{zx} + H_{zy}) \\
(\varepsilon \frac{\partial}{\partial t} + \sigma_x)E_{zx} &= \frac{\partial}{\partial x}(H_{yx} + H_{yz}) & (\varepsilon \frac{\partial}{\partial t} + \sigma_y)E_{zy} &= -\frac{\partial}{\partial y}(H_{xy} + H_{xz})
\end{aligned}$$

$$\begin{aligned}
(\mu \frac{\partial}{\partial t} + \sigma_y^*)H_{xy} &= -\frac{\partial}{\partial y}(E_{zx} + E_{zy}) & (\mu \frac{\partial}{\partial t} + \sigma_z^*)H_{xz} &= \frac{\partial}{\partial z}(E_{yx} + E_{yz}) \\
(\mu \frac{\partial}{\partial t} + \sigma_z^*)H_{yz} &= -\frac{\partial}{\partial z}(E_{xy} + E_{xz}) & (\mu \frac{\partial}{\partial t} + \sigma_x^*)H_{yx} &= \frac{\partial}{\partial x}(E_{zx} + E_{zy}) \\
(\mu \frac{\partial}{\partial t} + \sigma_x^*)H_{zx} &= -\frac{\partial}{\partial x}(E_{yx} + E_{yz}) & (\mu \frac{\partial}{\partial t} + \sigma_y^*)H_{zy} &= \frac{\partial}{\partial y}(E_{xy} + E_{xz})
\end{aligned} \quad (2.8)$$

The microdisk in this calculation is 1.8 μm . Considering the extreme long calculation time involved, I used $\Delta x = \Delta y = \Delta z = 25 \text{ nm}$ ($\sim \lambda/10n$) and $\Delta t = \Delta x / \sqrt{3}c$ (magic time step). The air region around the GaAs microdisk is about 400nm thick, which is reasonable to prevent leakage from the microdisk. The PML layer is 10-layers-thick and the polynomial grading is simply $\sigma_x(x) = (x/d)^4 \sigma_{x,\text{max}}$ and $\sigma_{x,\text{max}} = \frac{0.8(m+1)}{\eta\Delta}$ (here $m=4$).

Basically the grid is $116 \times 116 \times 48$. At every grid point, we need to store 42 variables (12 equations and their coefficients, 12 field components, 24 split field components), So totally 211 MB physical memory is required for storage and over 300 MB RAM is

required for this calculation. In my desktop PC (1.4 GHz P4 CPU and 256 MB physical memory), it took approximately 3hrs to run 1,000 time steps.

Before the formal calculation, I tested my code by running a short Hz Gaussian pulse propagating through the same space, but removing the GaAs dielectric disk. The result is shown below for both the xy-plane and the xz-plane. We see the wave is close to the expected spherical wave and propagating outwards and the PML boundary condition absorbs the wave well without any reflection.

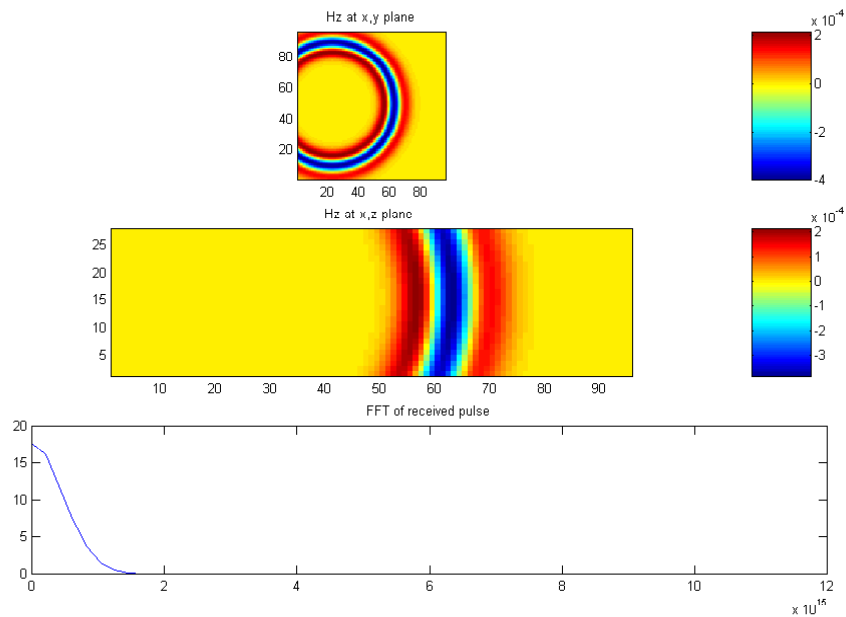


Figure 2-6. Test run of my 3D FDTD calculation.

The real calculation takes two steps: the first step is to launch a Gaussian pulse modulated by center frequency (corresponding to 900 nm wavelength). This is launched with the code:

```
if n < 300 Hz(i_A, j_A, k_A) = exp(-(n/50 - 3).^2) * sin(2 * pi * frequency * n * delta_t);
else
end
```

The hard source is defined at (i_A, j_A, k_A) which is about 300 nm away from the disk edge. The excitation efficiency of the hard source will greatly depend on where it is located. In general, when the hard source is near to the edge (~ 100 nm in our case) most

of the modes excited would be TE_{m1} since TE_{m2} has higher bending loss than TE_{m1} . When the hard source is placed a little bit far away from the edge, higher order modes have higher possibility to be excited. After running a long time, we can make a FFT of the field at the same point, and find out where the cavity mode is located. In Figure 2-7 below, we can see the result after the FDTD calculation runs 6,000 time steps. The longer the running time, the more precisely we can locate the mode position. In the 6,000 time steps run, we can roughly point out the location of the mode. The 6,000 time steps run also shows a mixture of several TE_{m1} and TE_{m2} modes. From the FFT curve, we can pick a “peak”, $f = 3.2216 \times 10^{14}$ Hz (corresponding to $\lambda = 931$ nm). By referring to the theoretical calculation table achieved by the techniques introduced in Section 2.1, we estimate it should be $TE_{11,1}$ mode ($\lambda = 937.7$ nm).

Table 2-1. The mode position and effective index for $TE_{m,1}$

	$TE_{8,1}$	$TE_{10,1}$	$TE_{11,1}$	$TE_{12,1}$
n_{eff}	2.4128	2.5330	2.5831	2.6327
Wavelength λ (nm)	1116.0	989.5	937.7	891.6
	$TE_{14,1}$	$TE_{15,1}$	$TE_{16,1}$	
n_{eff}	2.7168	2.7541	2.7886	
Wavelength λ (nm)	812.9	778.9	747.9	

Table 2-2. The mode position and effective index for $TM_{m,1}$

	$TM_{6,1}$	$TM_{8,1}$	$TM_{10,1}$
n_{eff}	1.3704	1.5628	1.7441
Wavelength λ (nm)	779.9	722.9	681.3

The next step is to launch a hard source at a single frequency where we guess the location of the resonant peak based on Step one and run the FDTD simulation. The field distribution is as below after 5,000 time steps. We can see that it is close to, but not exactly, the $TE_{11,1}$ mode (with roughly 11 maxima and 11 minima around the circle).

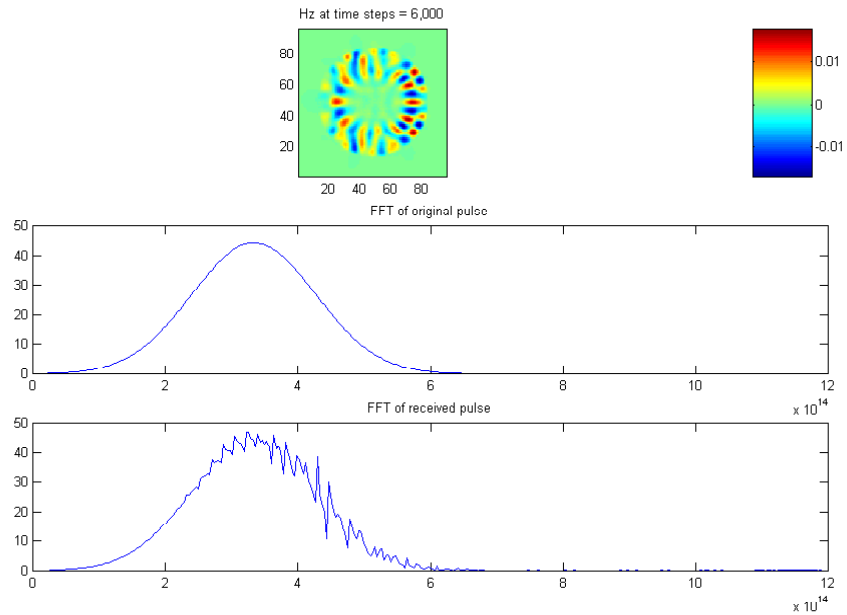


Figure 2-7. A Gaussian pulse centered at 900 nm is applied close to the left edge of the disk. The middle figure is the FFT of the original Hz pulse; the lower figure is the FFT of Hz at the same point after 6,000 time steps.

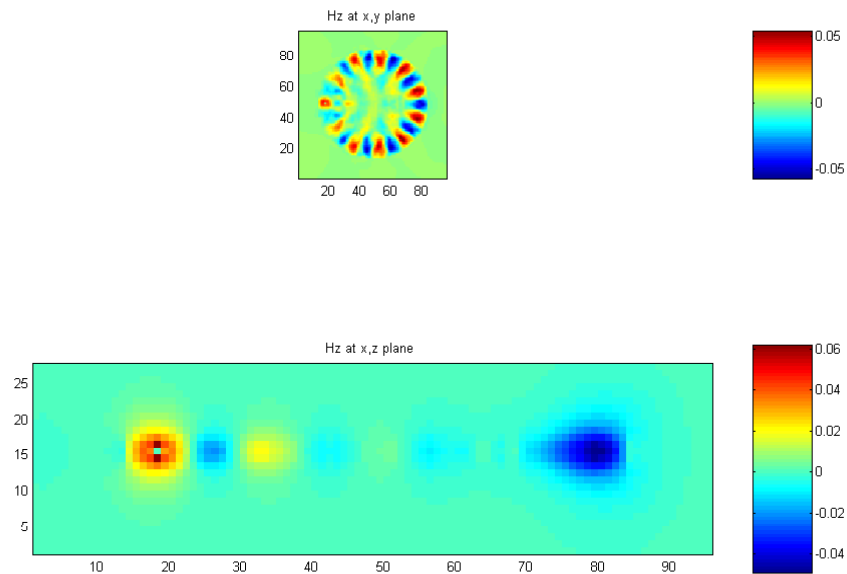


Figure 2-8. The field distribution after 5,000 time steps following application of a fixed frequency signal at a point close to the left edge.

To get a more accurate field distribution and mode position, we need to run the 3D FDTD on a computer with enough physical memory. Unfortunately, it is usually difficult to figure out the cavity Q because of the extreme long run times. In order to figure out the Q , the FWHM of a peak should be comparable to FFT resolution, that is, $\Delta f = \frac{1}{N\Delta t}$ and $\Delta t = \frac{\Delta x}{\sqrt{3}c} = \frac{\lambda}{10n\sqrt{3}c}$, $Q = \frac{f}{\Delta f} = \frac{N}{10n\sqrt{3}}$. For example, to get a cavity Q of 3,000, a FDTD run of 180,000 is required with a grid size of $\lambda/10n$.

A 2D simulation can be utilized to analyze the in-plane field distribution and cavity Q . Theoretically the cavity loss is due to bending loss at edge and there is no loss from the top or bottom surfaces since the dielectric microdisk is fabricated from perfect single crystal. Since $1/Q = 1/Q_{\perp} + 1/Q_{\parallel}$, we only need to consider the parallel loss (radiative loss, 10,000~100,000 typically). In order to achieve the necessary dimensions with very high resolution, e-beam lithography and dry etching are used to make microdisk devices. Unfortunately this approach produces relatively rough edges on the microdisk, which degrades the Q to 1,000~5,000. We can simulate how edge roughness affects cavity Q by changing the grid size. In our simulation, a grid size of 10 nm is used ($< \lambda/20n$), which is similar to a practical process. A surrounding air region with a thickness of 400 nm is used to prevent leakage. The final grid is 280×280 (taking up 10 MB physical memory) and also magic time-step ($\Delta t = \frac{\Delta x}{\sqrt{2}c}$) for two-dimensional case is used.

As mentioned previously, we can separate the 3D problem into 1D (vertical) + 2D (in-plane). In the vertical direction, we treat the disk as slab wave-guide since thickness \ll diameter of microdisk, and get the effective index n_{eff} ($1 < n_{eff} < n = 3.5$) corresponding to the wavelength of interest. We then have an analytical solution for the vertical 1D and use the FDTD simulation to solve the in-plane 2D problem. For the size and wavelength we specified, according to Table 2-1 and Table 2-2, $n_{eff} = 2.63$ (very typical value in WG mode) is used in our simulation.

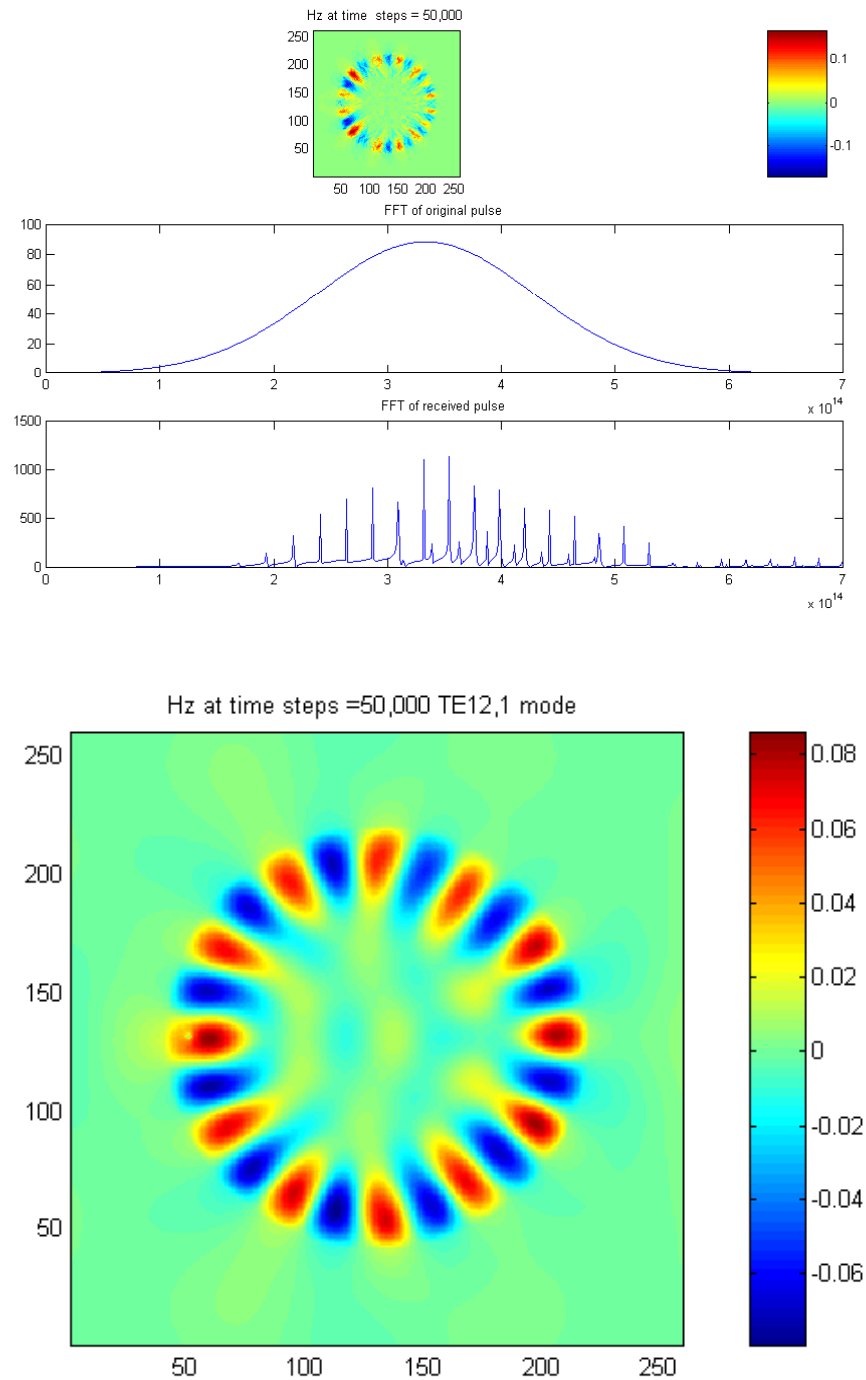


Figure 2-9. Two-step simulation to find the resonant peak and field distribution in a circular disk with 2D FDTD simulation. The first set of figures is for a Gaussian pulse as a hard d source to get the spectrum filtered out by the microdisk cavity; the last figure is with a sine wave as a hard source with the frequency calculated from the first step.

The split-field PML boundary condition is used in our simulation. Comparing both $TE_{12,1}$ modes calculations, we find a wavelength of 904.2 nm in the circular disk, which is close to both the theoretical estimation (891.6 nm) and 3D calculation. Also, the FSR value of 46nm can be calculated from all three methods. Using the 2D simulation, with the great saving in CPU time and memory usage, it is possible to find a solution for some more interesting configurations, such as how a deformed disk (elliptical shape) will change the Q and splitting. The deformed disk is of interest because it may be used to enhance the directionality of microdisk emission (in plane and tangential) to focus the emission into some specified angle [40]. Such a slight elliptical shape may occur natively. Wet etching is used to make high quality microdisk cavity, but the etching rate could have a small crystallographic asymmetry, thus an elliptical shape is unavoidable. Other configurations, such as the coupled microdisk (array) [41] photonic device can also be quickly simulated by 2D FDTD simulation.

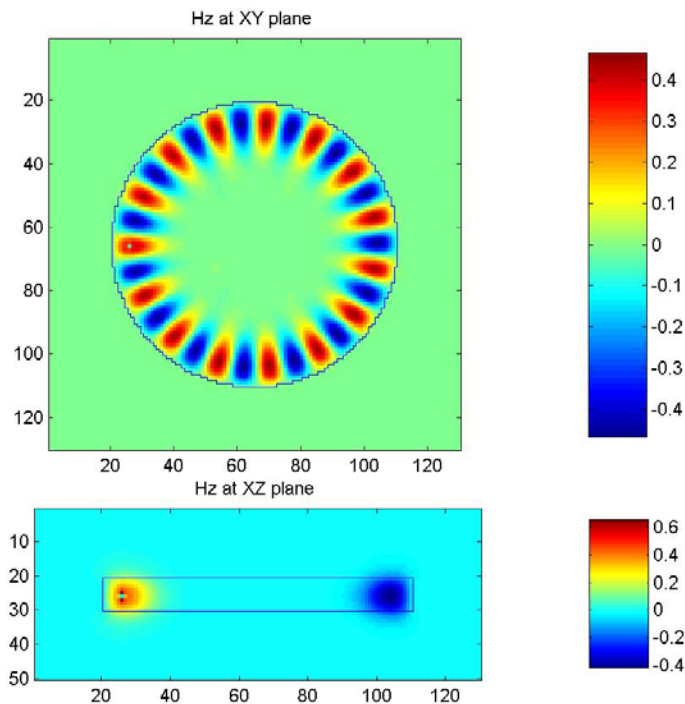


Figure 2-10. The electromagnetic field distribution of $TE_{15,1}$ mode for a 1.8 μm disk with a thickness of 200nm from 3D calculations. The grid size is about 20nm. The top view and cross section are shown.

3D FDTD must be used in case of some feature in the z-direction must be taken into consideration, such as the sidewall tilt and the disk undercut. In this section, we will list a 3D calculation for a microdisk with a diameter of $1.8\mu\text{m}$, a thickness of 200nm . A calculated spectrum is shown above. In this calculation a spatial grid size of 20nm is utilized and $5,0000$ time steps is taken for figuring a cavity $Q\sim 1,200$. With a grid of $160\times 160\times 70$, roughly 2 weeks and 450MB of memory are required for this calculation. Just keeping in mind, for a similar calculation on a $3\mu\text{m}$ disk, 1GB of memory is required and on a $4\mu\text{m}$ disk, 1.6GB of memory is required. For the microdisk with this diameter and a working wavelength of $\sim 900\text{nm}$, The FSR is $40\sim 50\text{nm}$ with a thickness $100\text{nm}\sim 200\text{nm}$. While the FSR is tightly related to the mode volume, this implies that vertical confinement for light is always the same for this thickness regime.

In this part of this thesis, we will also show how the tilted sidewall and undercut will influence the mode field distribution and cavity Q . In Figure 2-12, the mode profile for $\text{TE}_{15,1}$ and $\text{TE}_{16,1}$ is shown respectively with a 45 degree tilted edge. The grid is 20nm . These disks have a diameter of $1.8\mu\text{m}$, a thickness of 200nm and an undercut of 400nm . Comparing with the straight wall microdisk with a large undercut, we can see that there is a possibility of optical waves leaking into the pedestal. In Figure 2-11, with the same amount of running steps of $50,000$ with a resolution capability of $Q = 1,000$, it begins to show the difference of cavity Q in different configurations. An undercut of 400nm will limit the Q to be less than $1,000$. Also, we can calculate the FSR in different in different sizes of microdisks according to Figure 2-11. With a thickness of 200nm , the $3\mu\text{m}$ disk has a FSR of 24nm near a wavelength of 900nm , while a $1.8\mu\text{m}$ disk has a FSR of 43nm . In Chapter 5, we will show experimental data for cavity Q characterization of such issues.

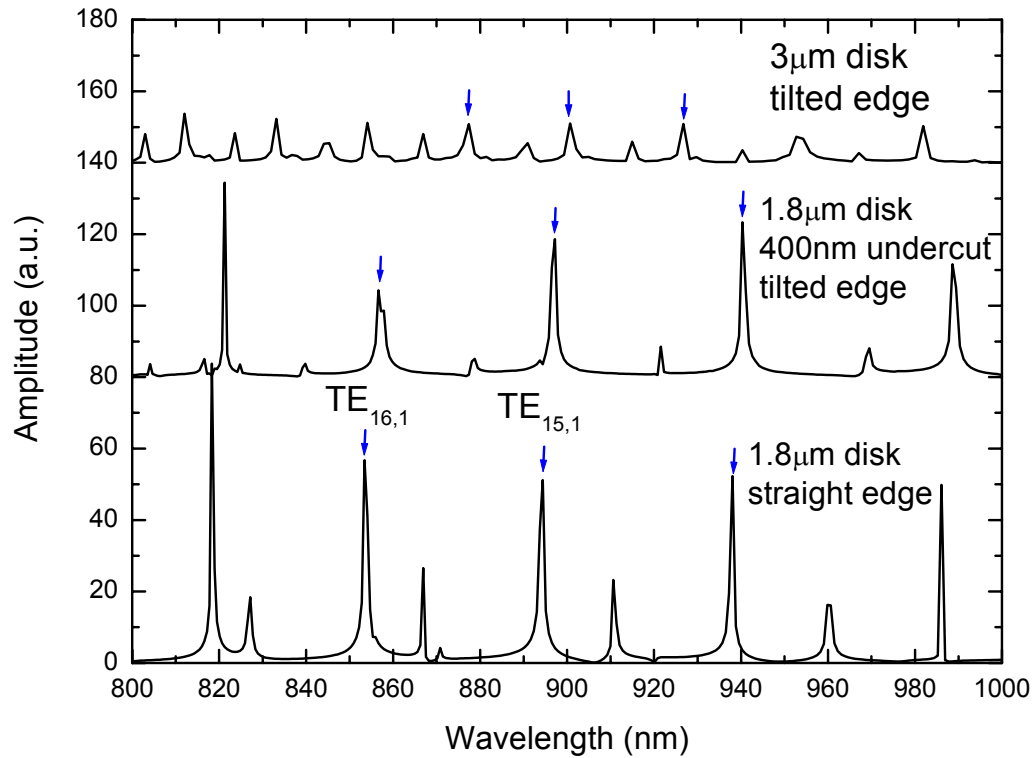


Figure 2-11. This figure shows the spectrum of 3 different disks with the same thickness of 200nm. 1) 3μm disk with 45 degree tilted edge and complete undercut. 2) 1.8μm disk with 45 degree tilted edge and 400nm undercut. 3) 1.8μm disk with straight edge and complete undercut. The blue arrow shows the positions of TE_{m,1} modes.

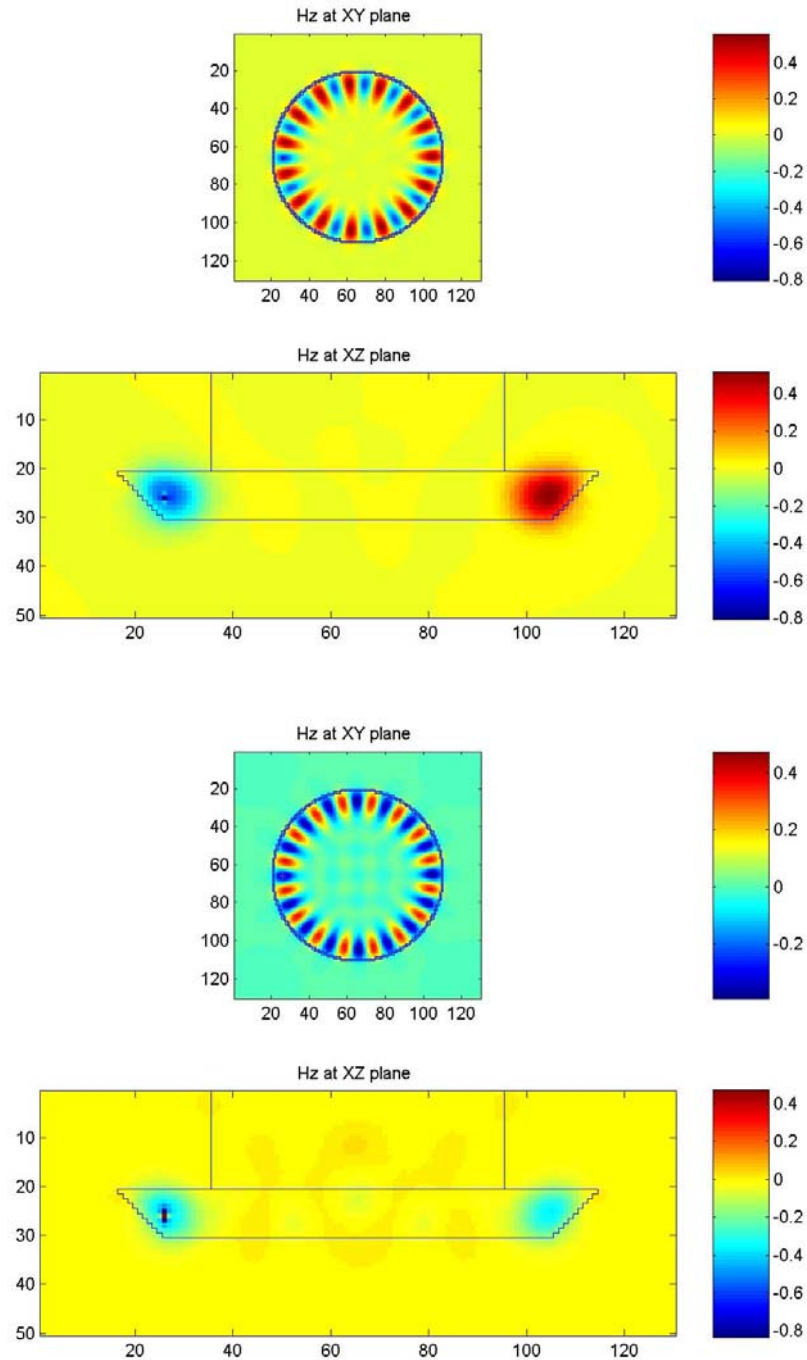


Figure 2-12. The mode profile for $TE_{15,1}$ and $TE_{16,1}$ and the edge is 45 degree tilted. The grid is 20nm. The top one is for $TE_{15,1}$ mode and the bottom one is for $TE_{16,1}$ mode. These disks have a diameter of 1.8 μ m and a thickness of 200nm.

Chapter 3. As Grown QDs Embedded inside Microdisk Sample

About 5 years ago, Prof. H. Cao's group at Northwestern University along with Dr. G.S. Solomon reported the first microdisk laser using QDs as the active media [29]. In their paper, a laser threshold as low as 23 μW for each 3 μm disk is achieved with a cavity Q of 5,000 for their best results. A wet etching and ebeam lithography technique is utilized. Several months later, Prof. Imamoglu's group at UCSB [42] got similar result, with a little different approach for the wet etching recipe and a cavity Q of above 10,000 is reported. Both papers used a very high density of QDs ($\sim 10^{11} \text{ cm}^{-2}$) as the lasing media, which is the general approach to get microdisk laser. Soon, Prof. Imamoglu's group reported a single photon source result [56] from the direct coupling of a single QD with microdisk cavity mode. In that case, a very different approach is used to get isolated QDs inside the cavity, with very low density of QDs embedded inside, and working in the SE regime instead of the lasing regime. Microdisk QD lasers are reported with different techniques for making disks. Recently, a group firstly realize strong coupling in a micro disk cavity, also reported a 2 μm GaAs/AlOx disk lasing at a threshold of 3900W/cm² [43], with a dot density of 400/ μm^2 . However, from the discussion above, spatially the cavity mode region is just a very small portion of the whole disk, with the minimum size of 1.5~2 μm in mind. So it is very important to optimize the growth of QDs and microdisk fabrication. We reported with a low density of 100/ μm^2 that QD lasing is achieved on our smallest high- Q disk, with a threshold of $\sim 200 \text{ W/cm}^2$, or 5 μW on each disk. On resonance, we can even see a reduction of the threshold to 50 W/cm², or 1.3 μW on each disk, which is very close to single QD lasing.

3.1. Self-assmbled QDs growth

To get the optimal InAs QDs quality, a growth temperature of 500°C and Group V/III flux ratio of 30 is used for the QD growth. Usually at this growth condition, the critical coverage of 1.7ML is expected. When the InAs deposition is in the range of 1.9~2.0ML, a quantum dots density of 50~100 / μm^2 can be achieved. Between 1.7~1.9 ML, we get a

low density, as low as $10/\mu\text{m}^2$, but the result is not quite repeatable. In Reference [29], an InAs deposition of 2.8~3.0 ML is used to achieve a high density of $1000/\mu\text{m}^2$ for the application of a micro-cavity laser. While for the application of a single QD laser or turnstile photon source, a growth condition of 1.9~2ML is reasonable. Figure 3-1 shows an Atomic Force Microscopy (AFM) image of such kind of growth. We count the density to be $50/\mu\text{m}^2$ for this sample and an average QD lateral size of 40nm and height of 5~10nm. At this growth condition, we will see a low intensity of SE at the wetting layer of 850nm and high intensity of sharp peaks around 890nm~950nm under low pumping region [44], contrast to the growth in Reference [29], where a wavelength of 920-980nm is achieved. So before the processing, a 600~700nm AlGaAs layer, 75nm GaAs, 1.95ML InAs and 75nm GaAs layer are sequentially grown. According to FDTD calculation, a disk layer of 150nm will be most suitable for efficient optical cladding, good for small mode volume as well as QD protection from surface states.

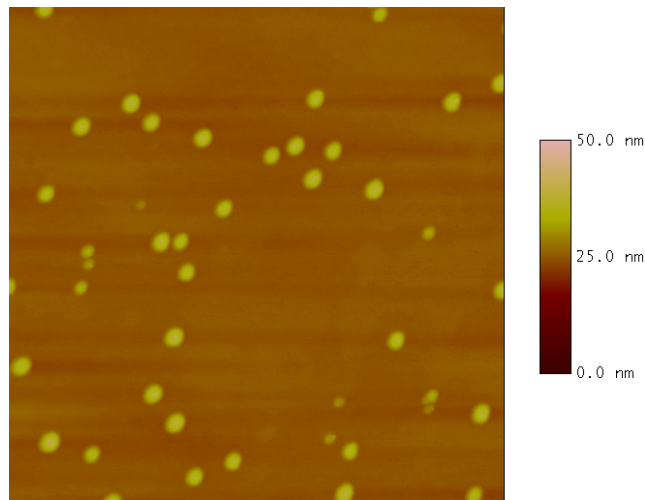


Figure 3-1. A $1\mu\text{m}$ scale AFM image of the 1.9ML QDs with a growth temperature of $500\text{ }^\circ\text{C}$. We would expect see a dots density of $50/\mu\text{m}^2$.

3.2. Microdisk fabrication

The microdisk pattern is defined by optical lithography. Using the $1\mu\text{m}$ thick photoresist as an etching mask, the pattern is transferred to the MBE grown sample. An alternative scheme is to use e-beam lithography, Ni film lifted off technique and Si_3N_4 or

SiO₂ as the etching mask. There are a broad selections for using such kind of recipes, but the resulting microdisk Q is quite similar, yet the process is more complicate and time consuming comparing with optical lithography. The optical lithography based recipe is described at the end of this thesis.

The next step is to transfer the microdisk pattern to the MBE grown sample and is very critical for the high Q microdisk sample. That is, non-selective etching or quasi-isotropic etching of the GaAs and AlGaAs layer. The requirement is to etch GaAs and AlAs at the almost same rate. Usually a two-step chemical reaction takes place. The first step is to oxidize the GaAs or AlAs surface. Usually a weak oxidant is used, such as hydrogen peroxide, or diluted nitride acid. The next step is to remove the oxide. Both acids and bases can be used to remove the oxide, such as phosphoric acid (H₃PO₄), hydrochloric acid (HCl), hydrofluoric acid (HF) or ammonia (NH₄OH). The removal of the oxide from the GaAs and AlAs should be at the same rate. To get an isotropic etching, usually the chemical should be in the oxidation-limited regime, where the removal of oxide is much faster than the generation of oxide. In the next several, we listed several choices of recipe for the non-selective etching, such as HCl based solution, HBr based solution and HF:HNO₃:H₂O or HCl:HNO₃:H₂O solution.

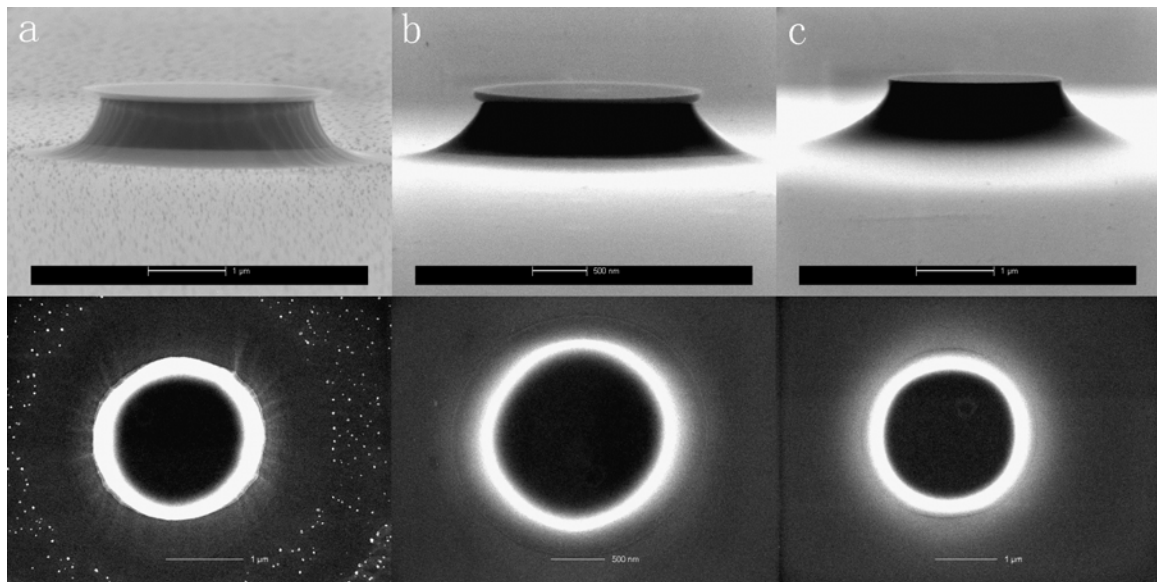


Figure 3-2. SEM images of HBr-based etching with both side view and top view. (a) oxide-removal-limited regime; (b) interim regime; (c) oxidation-limited regime.

Our conclusion is that the HBr based solution is the best choice to get a high Q microdisk cavity since it generates smooth and straight sidewall. However, we can see that in the oxide-removal-limited regime, usually etching of AlAs is much faster, which usually make sharp angle for the sidewall. In the oxidation-limited regime, we get really isotropic etching and seamless profile in the GaAs-AlGaAs boundary. And for the downward etching of $0.75\ \mu\text{m}$, we would expect a diameter reducing of $1\ \mu\text{m}$ for the microdisk. In the interim regime, we don't get perfect straight sidewalls, but the slightly tilted profile will also be useful under some condition. So HBr based solution is the ideal etching chemical for non-selective etching. But unfortunately, it will generate toxic Br_2 gas, which make the storage vessel dark brown and not permitted in the CIS clean room.

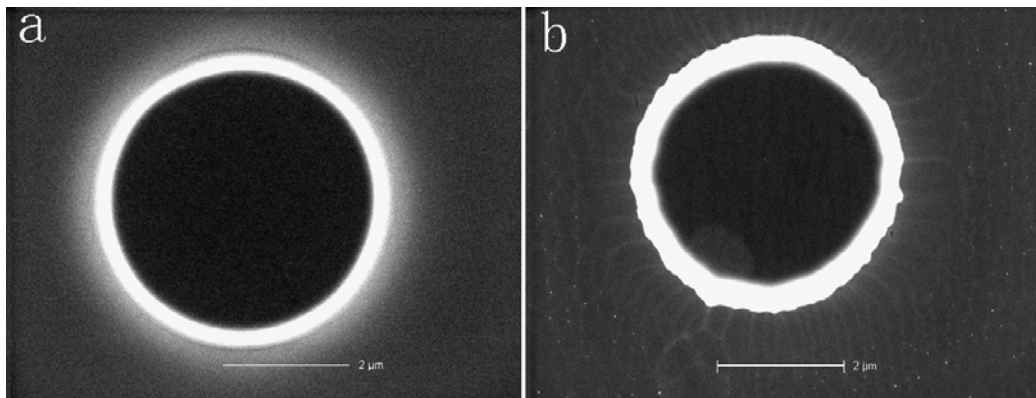


Figure 3-3. SEM images of the first-step-etch by (a)HBr and (b)HCl for disks with a diameter $3\ \mu\text{m}$ and above. HBr based etchants cause smooth and circular profile, while HCl based etchants cause rough and un-circular profile.

We look for the alternate for HBr, which is HCl [45] [46]. Unfortunately, a HCl based solution is always easy to bubble and makes the etched surface not smooth. All the other standard acids provided in CIS clean room cannot reproduce the same etching result by HBr. We also tried the recipe of $\text{HCl}:\text{HNO}_3:\text{H}_2\text{O}=1:1:2$ and $\text{HF}:\text{HNO}_3:\text{H}_2\text{O}=1:1:2$ [47][48], and the result is showed in Figure 3-4 for HBr and HCl. It produces as smooth a profile as the HBr based solution, not as straight sidewall, but sometimes it will make very fast lateral etching in the GaAs and AlGaAs interface. Also, considering the etch rate is not constant, in the range of $200\sim 900\text{nm}/\text{min}$, and very sensitive to the heat generated during the etching process, this widely used recipe is not good for our purpose,

either. There are other quasi-isotropic etching recipe, we tried, but proved to be not as good, which will be discussed in the next chapter [49][50][51].

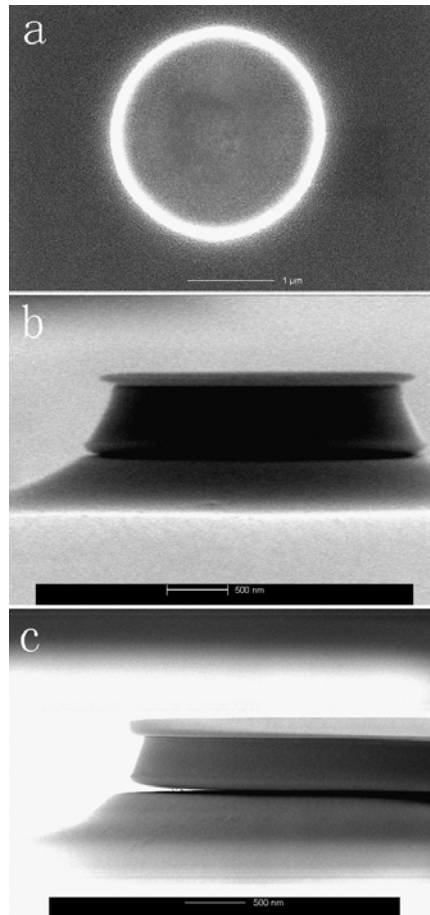


Figure 3-4. SEM images of HCl:HNO₃:H₂O=1:1:2 etching. (a) top view of a 2 μm disk; (b) side view of a 2 μm disk; (c) side view of a big disk showing there is a over-etch in the GaAs-AlGaAs interface.

The next step to finish microdisk is to make an undercut. For this step, we have the choice of hydrochloric acid (HCl), hydrofluoric acid (HF) or buffed oxide etcher (BOE). The advantage of the HCl undercut is a smooth interface. But the lateral etching is much faster than the vertical etching for the substrate with (001) crystal orientation, and it also generates octagonal cross-section if looking from the top, which is usually not important if the undercut is enough. On the other hand, HF based etchants will produce relatively rough interface in nanoscale, but are quite isotropic for the undercut [52][53].

In Figure 3-5, we show a typical 1.8 μm disk from the side view and several 3~4 μm disks from the top view. The dark pattern in the center is the pedestal. According to the

knowledge of the FDTD simulation, the mode profile will be only in the region about 300nm from the edge, an undercut of $1\mu\text{m}$ will usually be enough to ensure high Q cavity for big disk and $0.5\mu\text{m}$ undercut is good for the smallest disk ($1.5\sim 2\mu\text{m}$).

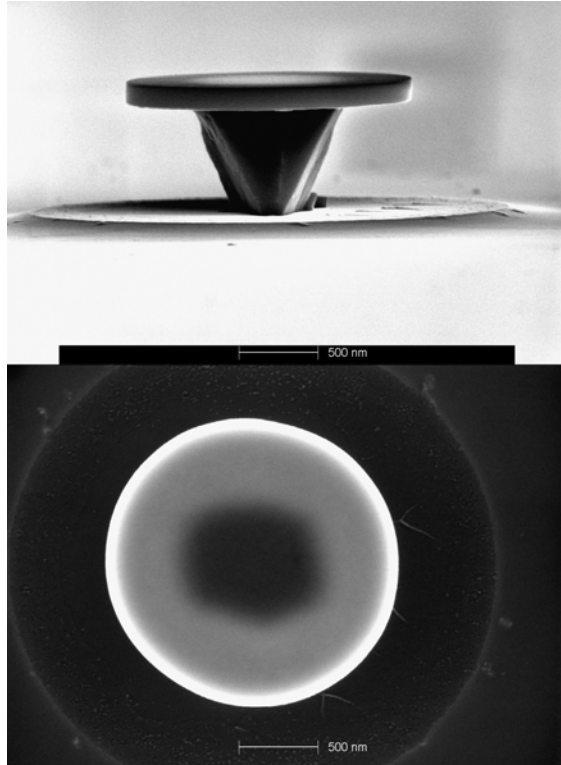


Figure 3-5. An SEM image of our $1.8\mu\text{m}$ disk. The undercut is roughly $0.5\mu\text{m}$ and the pedestal is about $0.8\mu\text{m}$ wide and $0.7\mu\text{m}$ high, very robust. The thickness of the disk is 150nm .

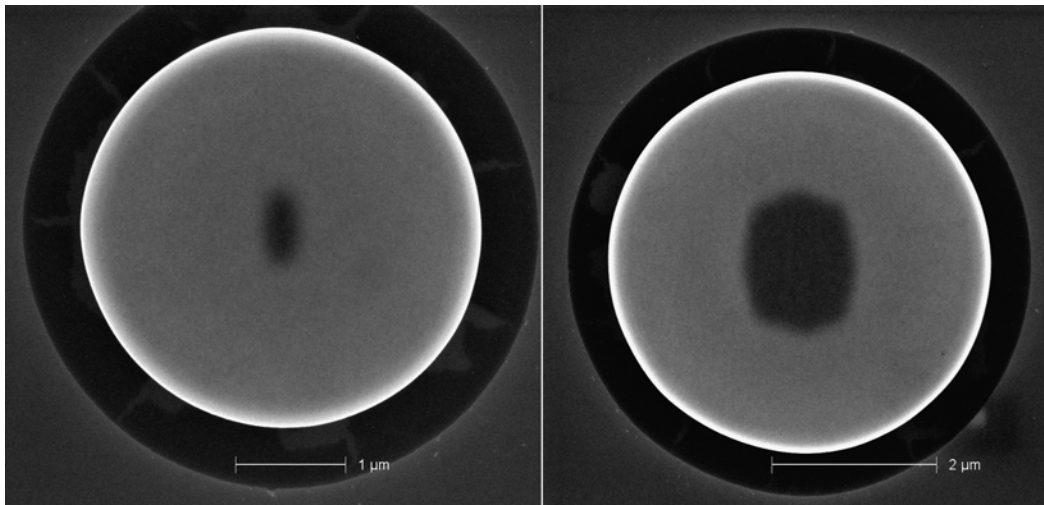


Figure 3-6. An SEM image of our $3.5\mu\text{m}$ and $4.5\mu\text{m}$ disk. The undercut is between $1\mu\text{m}$ and $2\mu\text{m}$, far enough for high-Q microdisk. The shape is perfectly circular.

3.3. Optical setup and typical PL results for high-Q microdisk

This part of measurement is done at Northwestern University, Prof. Hui Cao's group. The advantage of their setup is a very small liquid-He-flow cryostat with both top window and side window accessible for PL collection. And the structure is explained as below. For most of our measurement, a long working distance objective lens with NA~0.4 is used to collect the PL signal from the sample, as well as the path for the pumping laser, a 45 degree beam split after the objective lens is used to separate the PL signal and pumping laser. With this setup, the laser beam spot can be focused down to 2 μ m and the lens can be as close to the sample as possible. The disadvantage is, of course, with the sacrifice of 50% signal and a very strong reflection of pumping laser in the detection path, which cannot be filtered out completely. The objective lens is adjusted to produce a magnification of 67. The image is then demagnified ~20 times to match the NA of spectrometer, a value of 0.14, or with an additional magnification of 3, is captured by the CCD camera. With a total magnification of 200, it is easy for us to find the detail of the smallest microdisk. The side window collection is an auxiliary setup, typical for the microdisk cavity, since presumably in the in-plane direction we will have stronger signal from the Whispering-Gallery mode compared with the top. However, the disadvantage is the numerical aperture of lens for side collection is smaller (~0.2). Only the first one or two columns of disks close to the sample edge will be accessible for optical measurement. The majority of the disks will be blocked from observation.

The result turns out for our microdisk is that, the cavity mode signal is very strong, even at a low pumping level of 5W/cm², comparable to normal vertical cavity. It is quite surprising since the light scattering into the vertical direction should be very weak, which could due to our special sharp of the pedestal. In Figure 3-7, the PL measurements from the top and the side are compared. Our objective is to get as strong as possible of single QD signals (usually favored by top collection), and meanwhile get as high as possible mode-to-background ratio (usually favored by side collection). We prove, from all size of disks, the mode-to-background ratio is almost same for top and side collection. Although in the side collection scheme, more modes are visible, which is usually TM modes or higher-order modes with low cavity Q . Since we are only interested in the high- Q

fundamental TE modes and QD Spontaneous Emission signals, we will only focus on the top collection for most of our measurement.

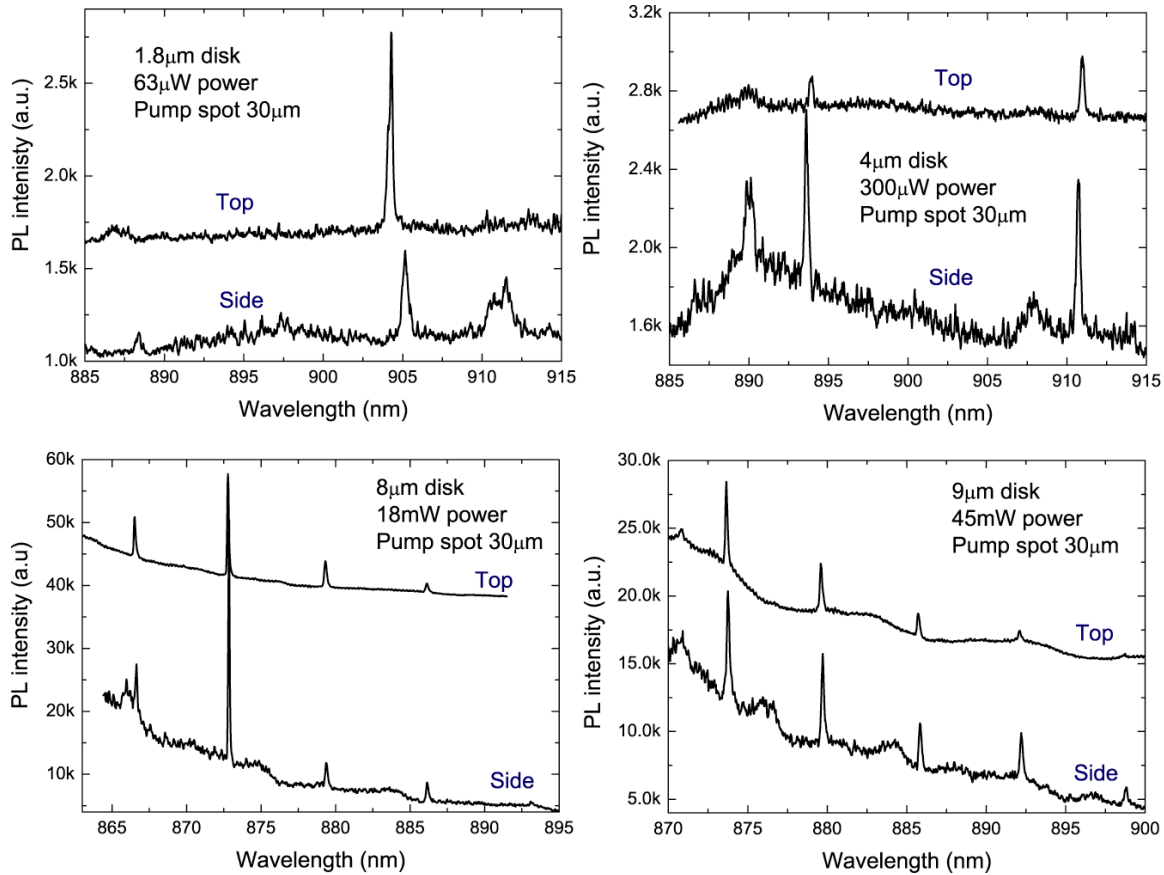


Figure 3-7. Comparison between top and side collection. All the data are collected at the same pumping power.

So in Figure 3-8a, with a typical PL we show a FSR of 45nm for the smallest sample. There are usually two modes in our QD wavelength regime, very occasionally, three modes. In Figure 3-8b, we show the statistical distribution of the modes position by observation of all modes, sequentially taken from a row of microdisks with the same design size. In this figure, the red shaded area shows the QD SE wavelength region of 890-950nm. With a FSR of 45nm, quite likely only two modes are present in the QD regime. We connected all the data points, possibly related to the same mode, for example, $\text{TE}_{15,1}$ close to 900nm. We can see that the neighboring disks have close mode position and the mode positions are gradually changing from one side of the wafer to another.

This result is not surprising since all the variations are caused by small difference of chemical etching rates.

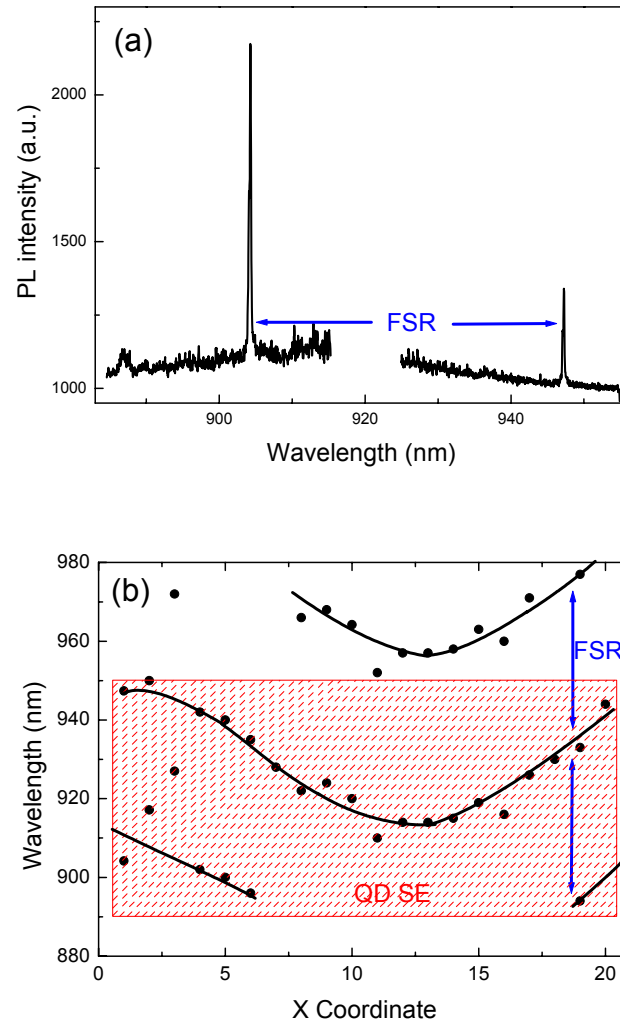


Figure 3-8. (a) PL spectrum shows the FSR of a typical 1.8 μm microdisk, which is roughly 45 nm. In the QD SE regime, there only exist two TE modes. (b) The mode positions along a row of 1.8 μm disk. The neighboring disks have very close mode position (wavelength).

The way to distinguish a mode and QD is power tuning and temperature tuning. Typically a mode peak will shift much slower than a QD exciton peak when the temperature is changed, which will be described in more detail in the section 3.4. That is the mechanism for temperature tuning. For power tuning, for example, the QD peak off resonant will saturate at a pumping power of 200 μW and the optical modes keep

increasing until a saturation power of 6mW if the laser spot is 30 μ m. In Figure 3-9, we show a LI curve for a cavity mode without lasing and a typical QD. So typically at higher pumping power only modes exist over a flat background.

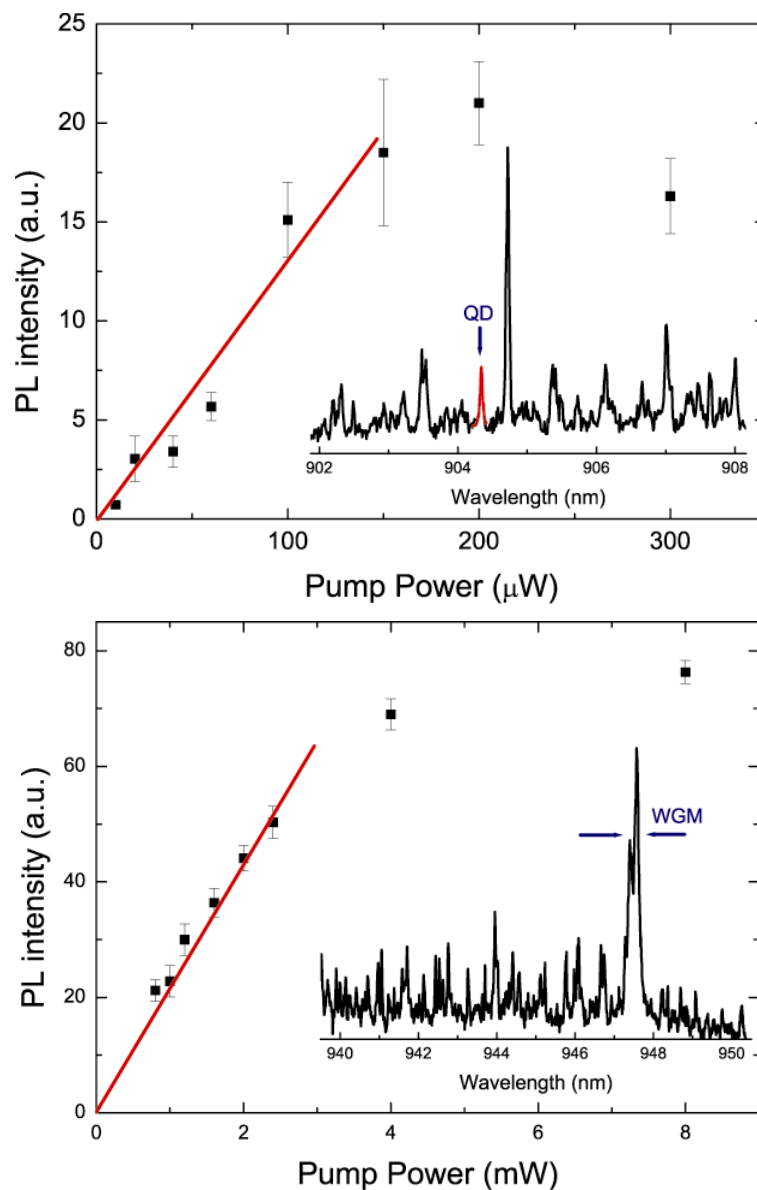


Figure 3-9. Power tuning curve for a single QD exciton peak and a cavity mode peak. The top figure is for the QD and the bottom figure is for the WGM.

For the smallest disk, usually it has a doublet, possibly due to the slightly elliptical shape of the disk. At low pumping regime, we measure a Q of 7,000 for the 1.8 μ m disk

and 13,000 above for the 3 or 4 μm (Figure 3-10). The actual Q of the disk could be higher due to the absorption broadening at the low pumping regime. The intrinsic Q should be decided at the transparent window. It will be discussed later, and the Q is roughly 10,000 for the 1.8 μm disk and beyond the spectrometer limit (a resolution of 0.06 nm) for the bigger disk. In Figure 3-10, a high-resolution scan shows the PL of a high- Q mode under threshold. This mode will lase at a pumping of $10\mu\text{W}$ with a $6\mu\text{m}$ laser spot, so a power of $1\mu\text{W}$, which is much lower than threshold, is used for this measurement.

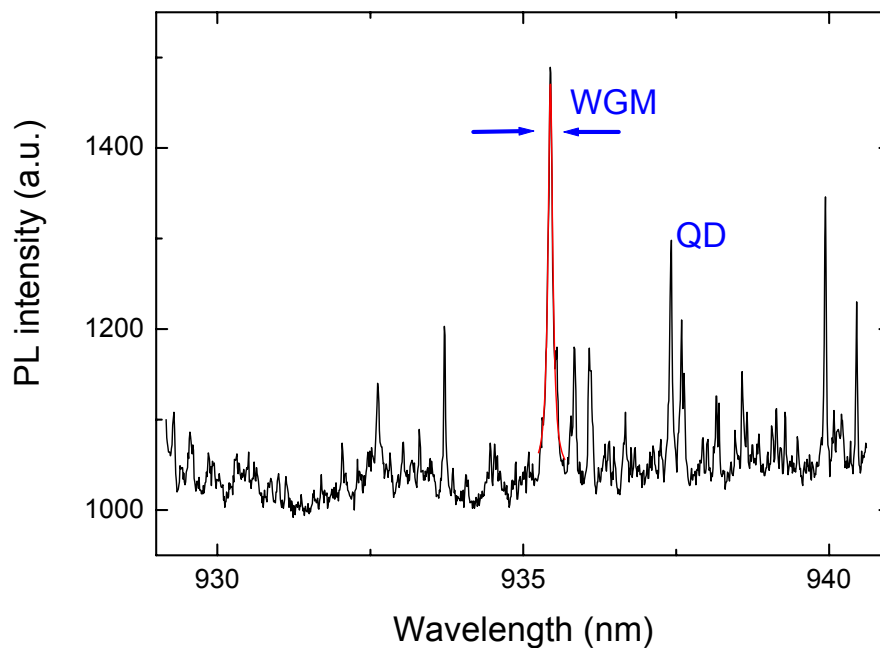


Figure 3-10. A high-resolution PL spectrum shows a high- Q mode from a 3.5 μm disk. The linewidth is about 0.067nm after de-convolution, which suggest the Q is 13,000 and above. The actual Q might be higher than this because absorption broadening, but it is beyond the spectrometer resolution.

3.4. Low-threshold QD lasing

For our smallest microdisk, we measure the LI curve. On half of our smallest disks, we see no obvious lasing above threshold behavior like the mode shown in Figure 3-9. While, for the rest half, we find a lasing threshold of $200\text{A}/\text{cm}^2$ in the temperature region of 6~50K, if there is no QD on resonant with the cavity mode, or on resonant but with poor

spatial coupling. The actual threshold power on the smallest disk is $5\mu\text{W}$ for each disk, which is much lower than the reported value of $20\sim 30\mu\text{W}$. On each disk, there are roughly 200 QDs in the disk and with an inhomogeneous broadening of 60nm . So for each mode, there is on average just less than one QD to spectrally couple with. However, in reality, there should be many QDs, say 10 QDs coupled to the mode, each with relatively weak coupling. Figure 3-11 shows the linewidth reduction when the pumping power crosses the threshold. From now on, we will switch from laser power to power density for the description of pumping strength.

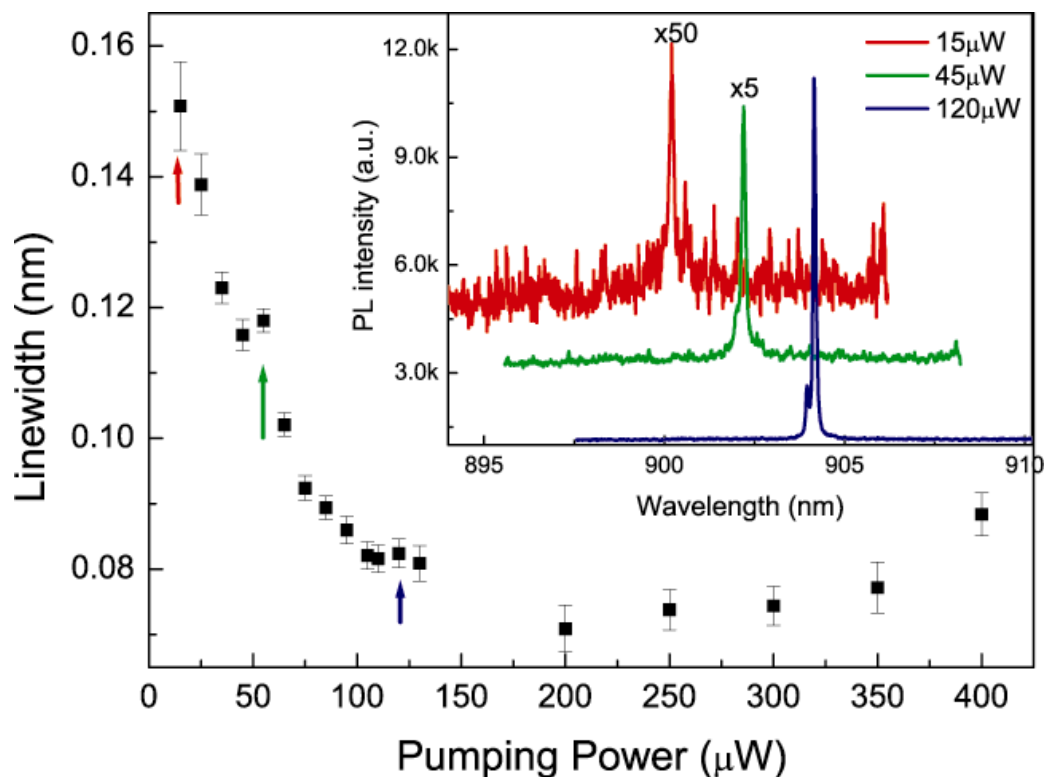


Figure 3-11. the linewidth of the cavity mode reduces with a increasing of pump power. The insertion shows the PL at 3 different pumping power points: $15\mu\text{W}$, $45\mu\text{W}$ and $120\mu\text{W}$. The threshold here is corresponding to a power of $45\mu\text{W}$.

There are doublet structures for our WGMs, but they always have the same lasing threshold, although the relative intensity of each mode will depend on the coupling with QDs. This fact suggests the onset of lasing of one mode actually will bring up the intensity of another. Figure 3-12 shows the LI curve and corresponding linewidth

narrowing for the temperature of 40K. We see a completely different skew rate below and above threshold, a much faster linearly increasing of intensity with the power increasing above the threshold. Meanwhile, the linewidth will narrow down from 0.15~0.18 nm to 0.065nm, roughly the resolution limit of our spectrometer. Maybe a little bit linewidth increasing when the pump is much above the threshold. All these suggest that typical lasing happens in our microdisk cavity.

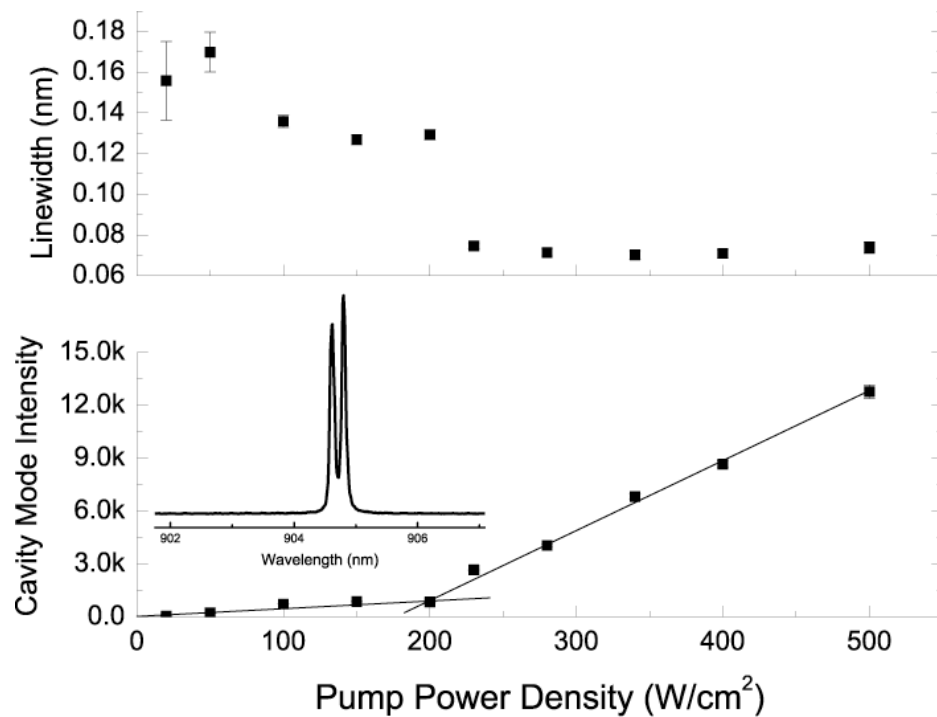


Figure 3-12. Lasing characteristics of a cavity mode at a temperature of 40K. The top figure shows the linewidth narrowing and the bottom one shows the intensity dramatically increases after the threshold.

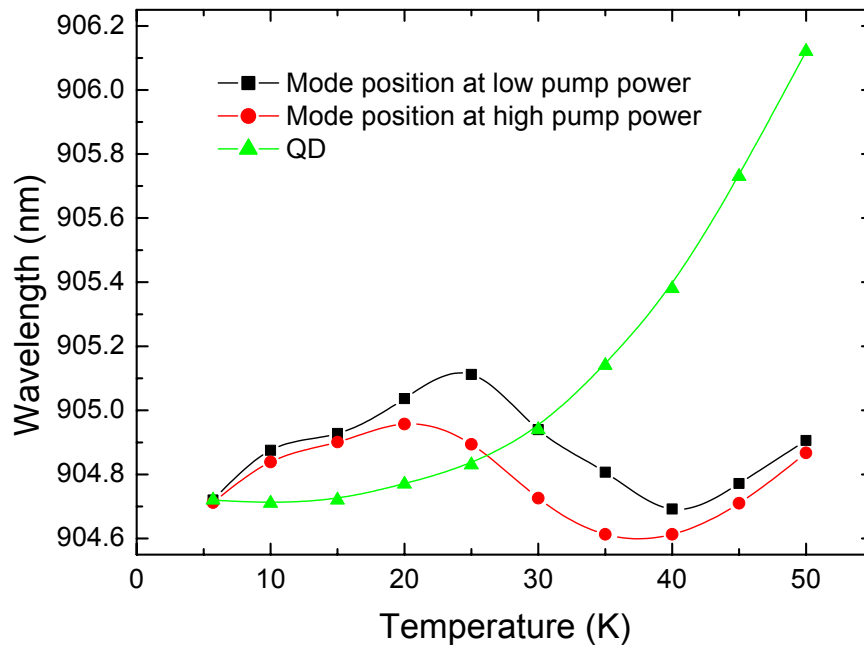


Figure 3-13. The WGM positions shift with temperature at low pumping power and high pumping power condition separately. A QD exciton peak shifting with temperature is also plotted for comparison.

Since the cavity modes position will be influenced by the refractive index, the carriers filling effect will cause the shift of the cavity modes position. We plot out the position of cavity mode with low ($40\text{W}/\text{cm}^2$) and high ($500\text{W}/\text{cm}^2$) pumping in Figure 3-13 and it does show the pumping shift of the cavity modes position at different temperature. This shift will cause a deviation from the standard L-I curve for the crossing of lasing threshold if the number of QDs coupled is very limited. We do see such a phenomenon, which suggest single QD or (1~3) QDs lasing is quite promising in our structure.

3.5. Towards single QD lasing

In Figure 3-14 we plot the PL data at a temperature range of 4~50K. The temperature shift of cavity modes and QDs is quite different. Generally, it is possible to tune the QD peak through the cavity mode if originally at low temperature the QD peaks are at low wavelength side of the cavity modes. We did this kind of tuning, and the result is shown in the figure. We noticed for the $1.8\mu\text{m}$ disk the mode shift is not typical for traditional

microcavity: It red-shifts much faster than the QD peaks at a low temperature of 4K~20K, after a temperature of 25~30K it begins to blue-shift, while when the temperature goes to 40K, it changes to red-shift again. So for some QDs, like dot “d”, it has double chance to cross the cavity modes. However, we see no change for the lasing threshold as well as the cavity mode intensity, which suggest no coupling effect for this QD. We notice that the PL intensity of this QD peak is relatively strong compared to other QD, which can be explained if the dot is located off the mode region, say, at the center of the disk, so its SE rate is just like the condition without the existing of a cavity. The other dots “a”, “b”, “c”, on the opposite, could be spatially coupled well with the mode, so its SE rate is suppressed when they are not on resonance with the mode spectrally.

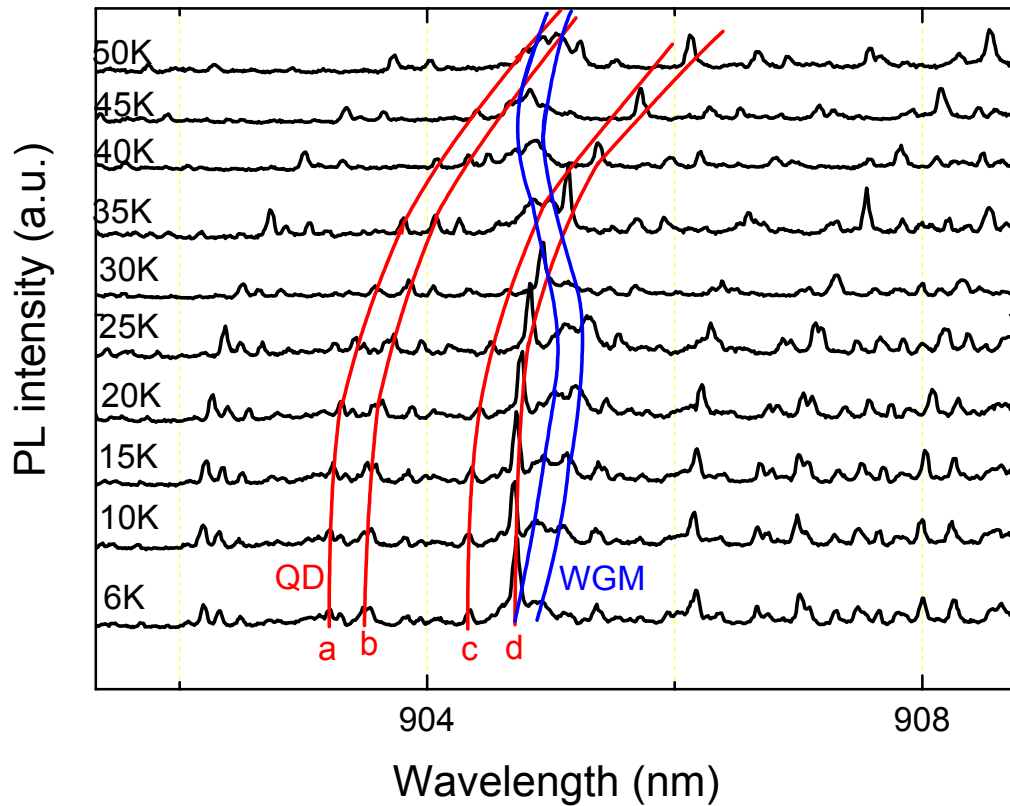


Figure 3-14. High resolution PL data at different temperature. The red curve shows the trace of QD peaks shift with temperature. They roughly shift equal distance for the same temperature change. The cavity modes don't shift monotonically.

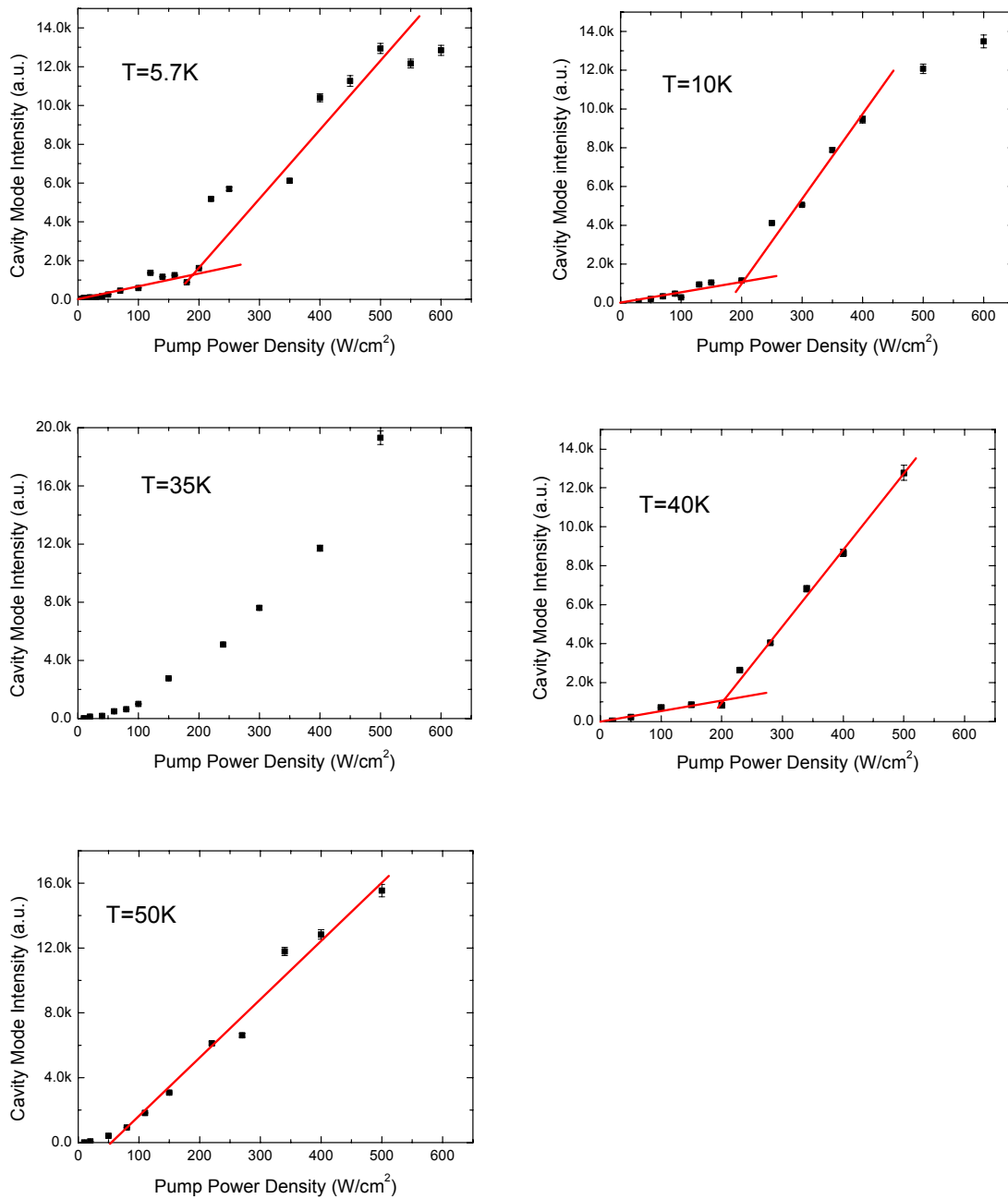


Figure 3-15. L-I curve for the cavity mode at different temperatures.

In Figure 3-14, at a temperature of 35K, dot “c” is roughly at a resonance of the mode and dot “a” and “b” are close to the resonance with the mode at a temperature of 50K. We noticed there is an obvious lasing threshold change at these temperature points.

Especially at 50K, the lasing threshold reduced to $50\text{W}/\text{cm}^2$ from the L-I curve, compared with L-I curve at a temperature of 40K. All these suggest on resonance coupling of QDs with the cavity mode will reduce the lasing threshold. So the lasing threshold will be $1.3\ \mu\text{W}$ for each disk, much lower than the reported value of $20\ \mu\text{W}$. Considering most of the optical power is reflected back from the sample, the actual power absorbed by the 150 nm thick GaAs will be about 15%, which give out an estimation of $8\ \text{W}/\text{cm}^2$ for the actual threshold. The result is close to the low threshold limit for broad area semiconductor lasers and creates the new record for a microcavity laser.

Chapter 4. Regrowth Dynamics of InAs Quantum Dots on the GaAs Circular Mesa and Partial Microdisk Cavities

In this chapter, we report MBE regrowth of InAs quantum dots on GaAs circular mesas, prepared by optical lithography. Because of better strain relaxation, the possibility of quantum dots growth near the lithographic edge is high. Under controlled growth conditions, quantum dots appear only close to the edge. Under these conditions, we discuss the possible influence of crystal orientation to the quantum dots formation, as well as geometrical factors, such as the lateral size of the mesa, and the depth and steepness of the lithographic step. With the full control of the quantum dots formation, we measured the photoluminescence spectrum of the buried dots, as well as the real space image from a CCD camera. The results indicate that quantum dots only form at the edge. Besides the physical location, all the other parameters are quite similar to self-assembled quantum dots formed on planar surfaces.

4.1. Circular features defined by optical lithography and chemical etching

The GaAs (001) substrate was patterned with normal optical lithography. Circular features from 2 to 20 μm were transferred to the sample using a wetting etching recipe of diluted $\text{H}_3\text{PO}_4:\text{H}_2\text{O}_2=1:1$ or $3:1$ and then photoresist was stripped. This recipe is widely used for GaAs based materials. For disk-shaped patterns, an additional undercut of $300\text{nm}\sim 1\mu\text{m}$ is required to define the pedestal. After standard solvent cleaning, a wet etching of diluted $\text{NH}_4\text{OH}:\text{H}_2\text{O}_2=1:1$ was used to remove a thin layer of GaAs ($\sim 40\text{nm}$). The sample was then transferred to the MBE chamber for growth. This process flow is explained in Figure 4-1 below. In this figure, the process flows for as-grown QDs in microdisk and regrowth QDs embedded inside a slant-edge disk are compared. Because of the MBE growth, the disk edge will be slant. Our first goal of process optimization is to make clean epitaxial regrowths to guarantee high quality QDs for optical application such as a turnstile photon source. A second goal is to keep the circular shape and smooth

profile to maintain a reasonable cavity Q. We find the approach in Chapter 3 will not guarantee the first goal.

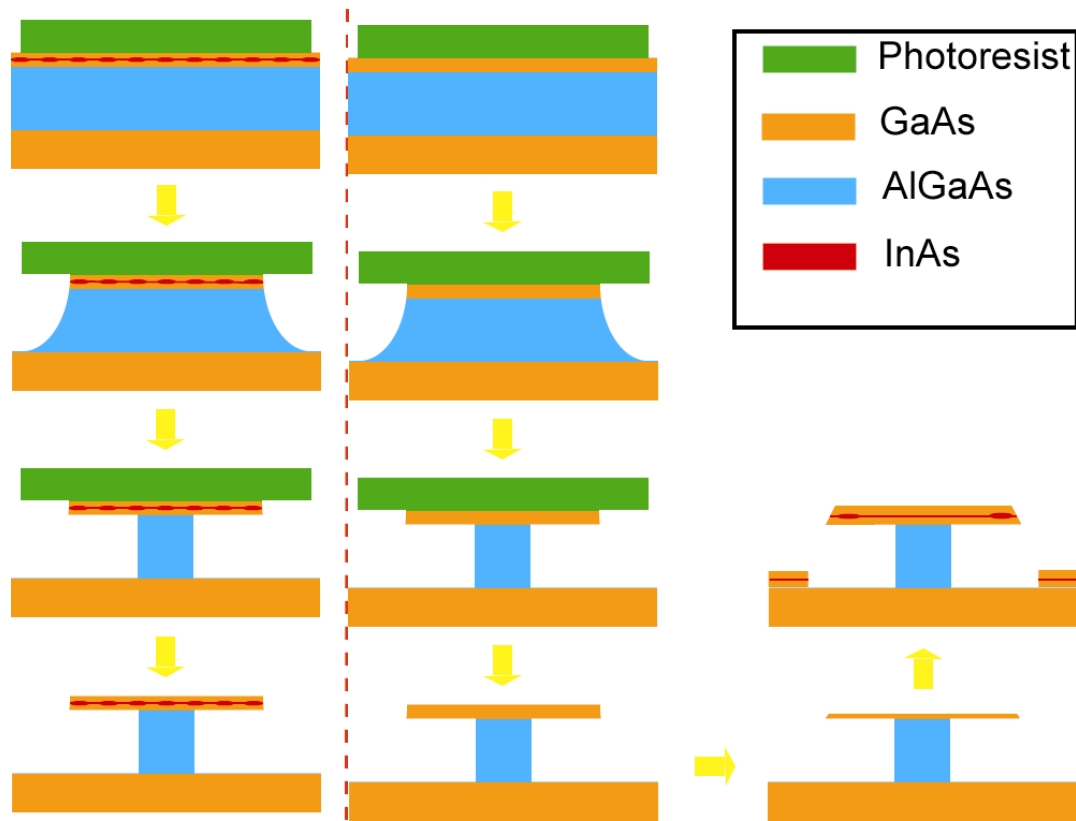


Figure 4-1. The left drawing shows the process flow for as-grown QDs integrated with microdisk; the right drawing shows the process flow for regrowth QDs integrated with microdisk.

To make clear what kind of recipe is satisfactory for regrowth purpose, we need to analyze what kind of chemical cleaning is compatible with regrowth. The recipe currently used is based on ammonia hydroxide and hydrogen peroxide. The regrowth is not an issue at all for silicon wafers since the dense oxide layer will be blown off at high temperature and leave fresh surface for growth. Similar phenomenon happens in GaAs wafer except the oxide layer is much thinner and not dense. If the last step is treated with an acid solution and rinsed in DI water, the sample will even lose the protection of this thin oxide layer during the process of loading and transferring. The same story happens on Si-wafer if it is rinsed in diluted HF solution to strip the oxide layer. Although some

research groups claim the acid based cleaning will provide a relatively cleaner surface under a combinational investigation [54] [55], it will not generate a successful epitaxial growth. Only with a thin sacrifice layer before loading or by the means of in-situ chemical cleaning will provide a clean surface for epitaxial growth. Ammonia hydroxide and hydrogen oxide based etchants are generally utilized in semiconductor industry since the thin sacrifice layer and trace ions or particles are easy to be blow off at a high temperature. Another reason to use this solution is that it will etch the photoresist and get rid of possible trace organic materials left after the standard solvent clean. In Figure 4-2, several images shows the regrowth results with this standard recipe clean, the standard recipe clean followed by a HCl dip and DI rinse, and a digital etching of HCl and hydrogen oxide alternately applied. These researches show only that our standard recipe clean can generate a clean surface without the aid of an in-situ ion-beam clean.

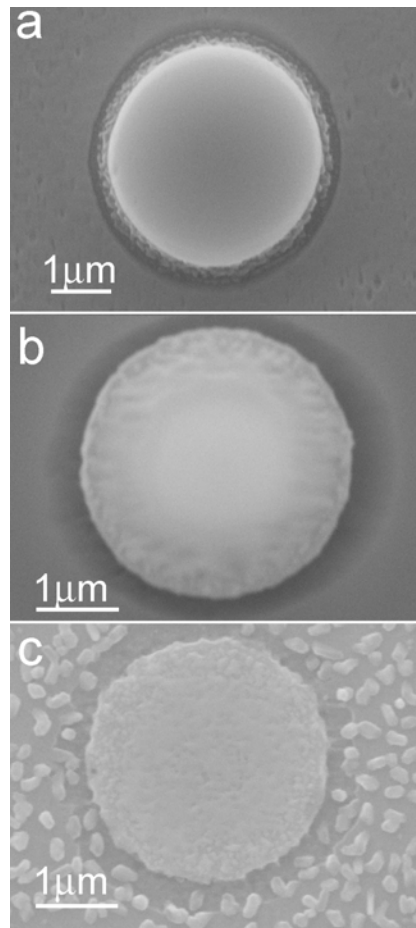


Figure 4-2. SEM images for Pre-loading chemical etching.

(a) $\text{NH}_4\text{OH}:\text{H}_2\text{O}_2:\text{H}_2\text{O}=1:1:100$ for 15secs; (b) $\text{NH}_4\text{OH}:\text{H}_2\text{O}_2:\text{H}_2\text{O}=1:1:100$ for 15secs and dipped into HCl solution;

(c) digital etching only: 15 cycle repetition of $\text{HCl}:\text{H}_2\text{O}=1:10$ for 30 secs and $\text{H}_2\text{O}_2:\text{H}_2\text{O}=1:10$ for 1mins.

The samples are rinsed in excess of DI water after relevant chemical cleaning.

In order to maintain the disk-like shape defined by the non-selective etch, the etch quota of the pre-loading etching should be very small. While after a very thin layer of GaAs buffer layer growth, InAs QDs will be grown. We must make the surface epitaxial ready after this shallow pre-loading etching. Those propose a challenging job for surface cleaning and overall chemical processing. Using the standard chemical cleaning, $\text{NH}_4\text{OH}:\text{H}_2\text{O}_2:\text{H}_2\text{O}=1:1:100$ for 15 secs will etch away 50nm of GaAs. The thin AlGaAs layer exposed will make the etching a little slower on the bottom surface of the disk structure. So the overall GaAs material etched away is between 50nm and 100nm. We select the initial GaAs top layer to be 120nm thick. Chemical residue, photoresist residue and aluminum oxide will contaminate the top disk surface. Figure 4-3 shows the failed regrowth due to chemical residue contamination at the disk edge, photoresist residue, and the aluminum oxide contamination from the bottom surface. Figure 4-4 shows the disappear of disk-shape or complete removal of top GaAs layer due to overetching for a 100nm of top GaAs layer. A thicker GaAs layer (>150nm) will provide a bigger room for adjusting the etching quota. However, either the disk edge will be too slanted or the disk is too bulky for microdisk application. This small tolerance of etching time or the top layer thickness reduces the stability of pre-loading clean for regrowth. One way to solve the problem is to use an even diluted solution for better control. However, even with the aid of stirring, the surface status is not as ideal under an AFM investigation. The pin defects show up, which is quite typical for low quality regrowth.

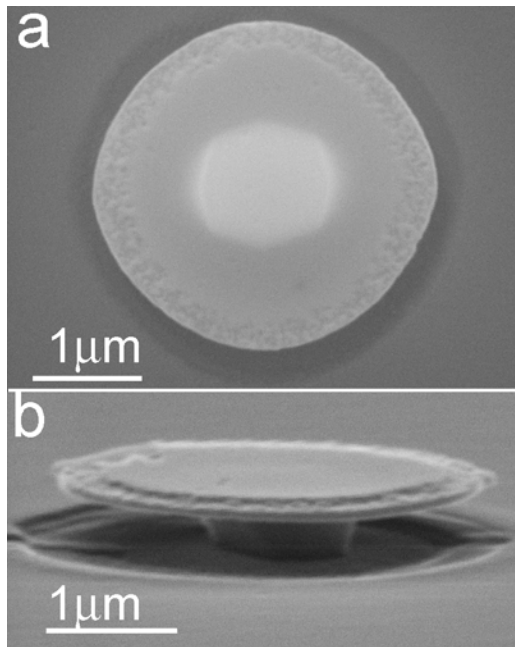


Figure 4-3. SEM images show insufficient chemical cleaning. (a) top view; (b) side view. Defects most likely happen at the disk edge, due to photoresist residue and junk trapped around the disk.

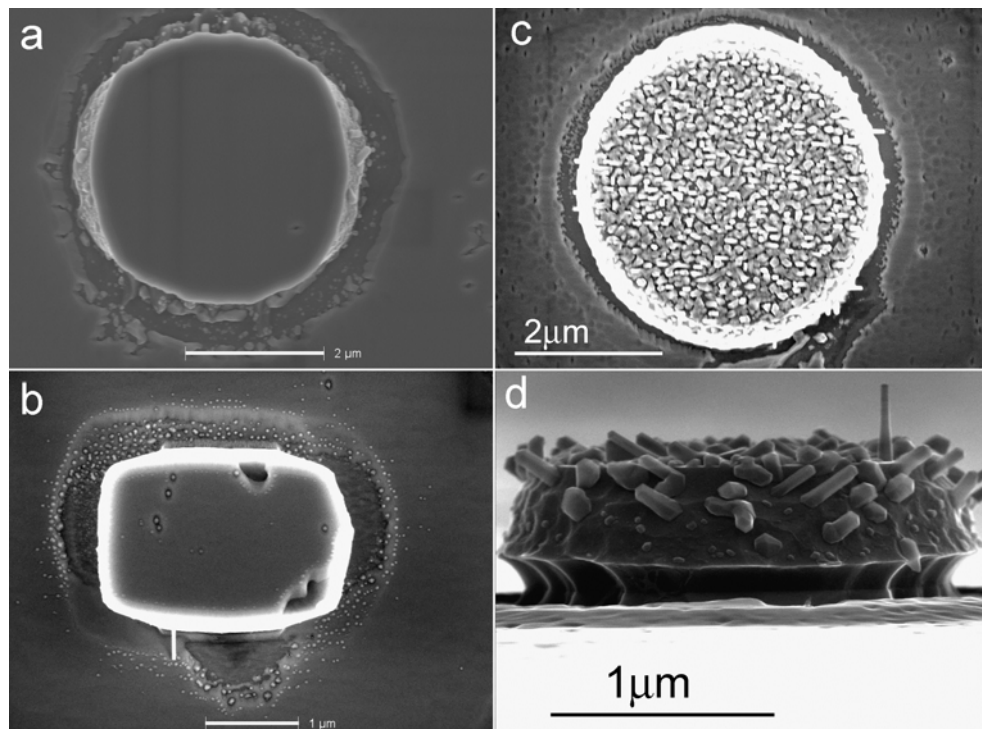


Figure 4-4. Etching depth is too much. (a) the disk shape deviates from circular shape; (b) part of the GaAs layer extending out has been etched away; (c) the GaAs top layer almost completely gone (top view); (d) the GaAs top layer almost completely gone (side view).

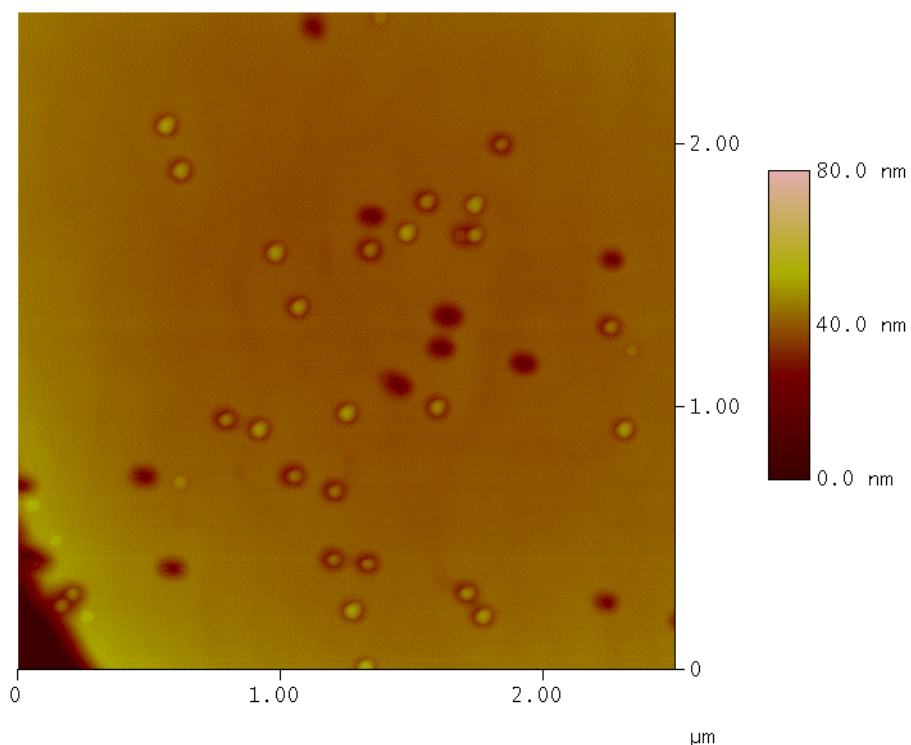


Figure 4-5. An AFM image shows typical pinhole defects when the pre-loading etching solution is too diluted.

Aluminum contained materials are generally not compatible with regrowth. The complex of surface profile makes the cleaning work even challenging. Actually we cannot isolate the selection of pre-loading clean and first-step non-selective etching for the micordisk regrowth. Figure 4-6(a)(b) shows failed regrowth if the non-selective etching is in the oxidation-limited regime for HBr based recipe (a) and $\text{HNO}_3:\text{HCl}:\text{H}_2\text{O}=1:1:2$ recipe (b), although they generate a smooth and circular profile. Unfortunately we have to use a chemical recipe in the interim regime or oxide-removal-limited regime (Figure 4-6(c)(d)) to make a successful regrowth. In this regime, $\text{H}_2\text{SO}_4:\text{H}_2\text{O}_2:\text{H}_2\text{O}=1:8:80$ will give a good regrowth, while it deviate too much from the circular shape. $\text{H}_3\text{PO}_4:\text{H}_2\text{O}_2:\text{H}_2\text{O}=1:1:25$ or $3:1:25$ will give acceptable circular shape.

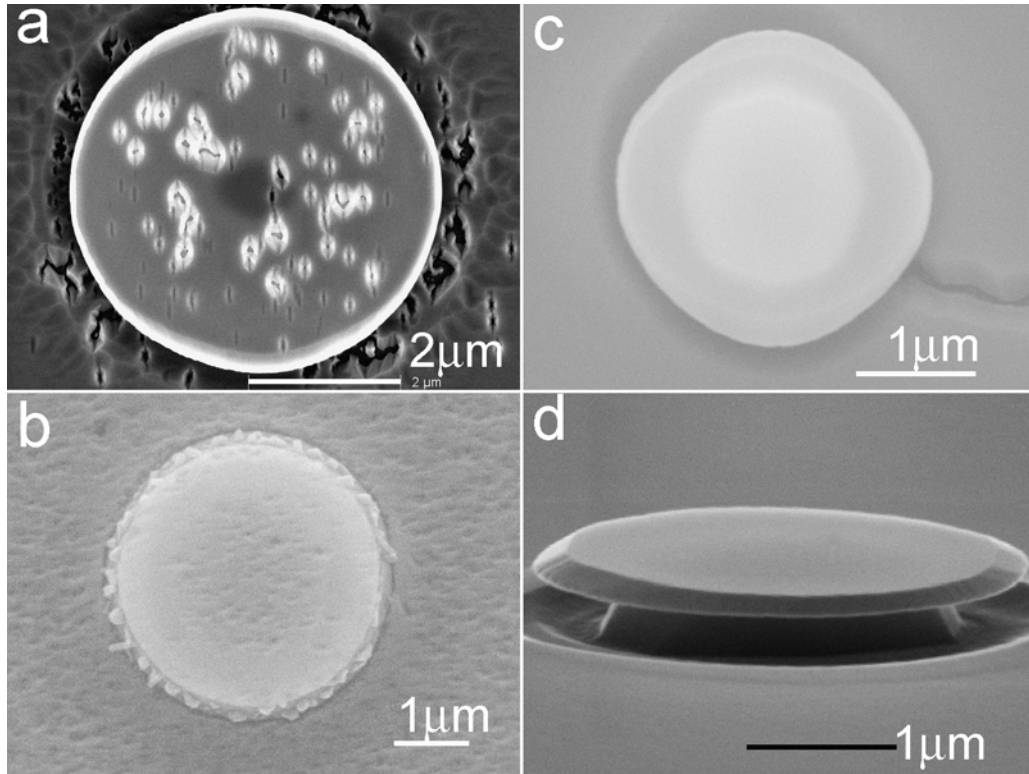


Figure 4-6. The choice of non-selective recipe will influence the regrowth results. (a) HBr based recipe; (b) HCl:HNO₃:H₂O=1:1:2; (c) H₂SO₄:H₂O₂:H₂O=1:8:80 (top view); (d) H₂SO₄:H₂O₂:H₂O=1:8:80 (side view).

Working on quasi-nonselective recipe, we must give consideration to all the growth issues such as the aluminum concentration in the AlGaAs layer and the thickness of AlGaAs layer. With the phosphoric acid based quasi-nonselective recipe, the etching profile on a pure GaAs substrate is 45 degree slanted, which is not ideal, but does not matter since the pre-loading clean will make the sidewall slanted anyway. We found out if the thickness ratio of AlGaAs layer over GaAs top layer is less than 5 and $x=70\sim 75\%$, the slant angle will be the same as pure GaAs material. However, if the aluminum concentration is higher than 77%, with the increasing of etching thickness in AlGaAs layer, the slant angle will suddenly switched to $-45\sim -60$ degree. This sudden switch will make the edge even rougher. In our process, we will try to avoid this condition. However, the undercut will not happen if $x < 70\%$ and the pedestal must be at least with a height of 600nm to prevent light couple to the substrate, which require careful balance of process condition. Figure 4-7 shows the slant angle change in these two conditions.

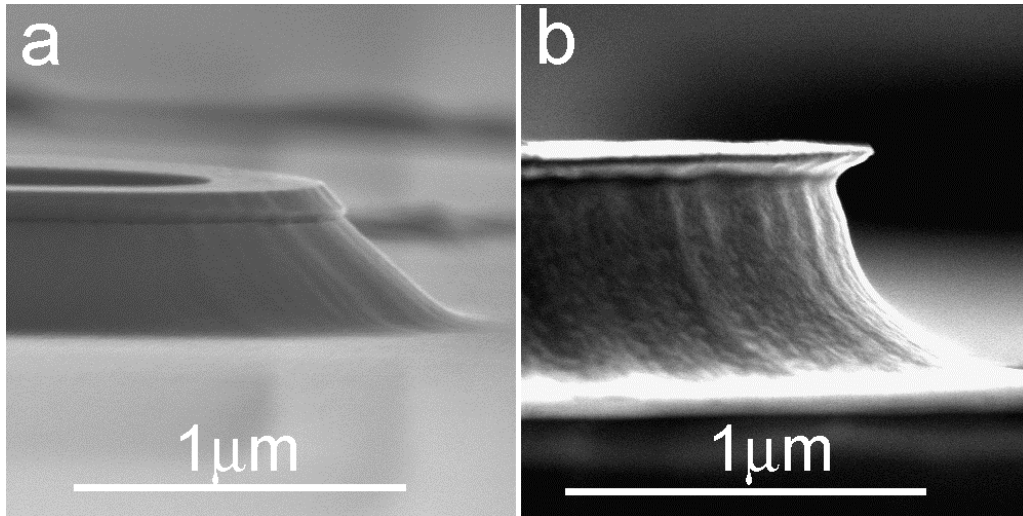


Figure 4.7. Quasi non-selective profile depends on the AlGaAs layer thickness and aluminum concentration. (a) the edge is 45 degree tilted when the aluminum concentration is 70%; (b) the tilting angle of the edge is reversed to $-45\sim-60$ degree, if the etching depth is over 600nm and the aluminum concentration is 80%. In both cases, the top GaAs layer thickness is 120nm.

4.2. MBE regrowth on a circular shaped mesa

Because of the atom-like nature, self-assembled quantum dots (QD) are of great interest as a single photon emitter [56] [3]. From early 90's, this strain driven phenomenon has been realized and widely investigated on many lattice-mismatched systems, such as Ge/Si [57], InAs/GaAs [58] and InGaAs/GaAs [59]. Despite the nature of random distribution, some techniques are used to “guide” the QD formation. One of them is a QD superlattice [60], in which the underlying layer of QDs serves as the stressor of the upper level QDs. Another approach is to use lithographic features to seed the QD formation or confine the lateral size of QDs [61]. In this case, usually ultra-high resolution lithography is required to define the sub-100 nm QDs. In this part, we will discuss another way to control QDs positioning without the aid of ultra-high resolution lithography, that is, self-assembled QDs formation on an optical lithographic edge. T.D. Kamin [62], et al. presented a method of Ge QDs formation on Si pixel lines. It may seem trivial, but this approach can be further developed to incorporate QDs into optical devices [63]. In this paper, we present the research of InAs QDs regrowth on GaAs (001)

substrate. This self-assembled prototype system is mostly widely investigated and unlike the Ge/Si system, we can extract the growth dynamics information using optical methods, besides normal material characterizations.

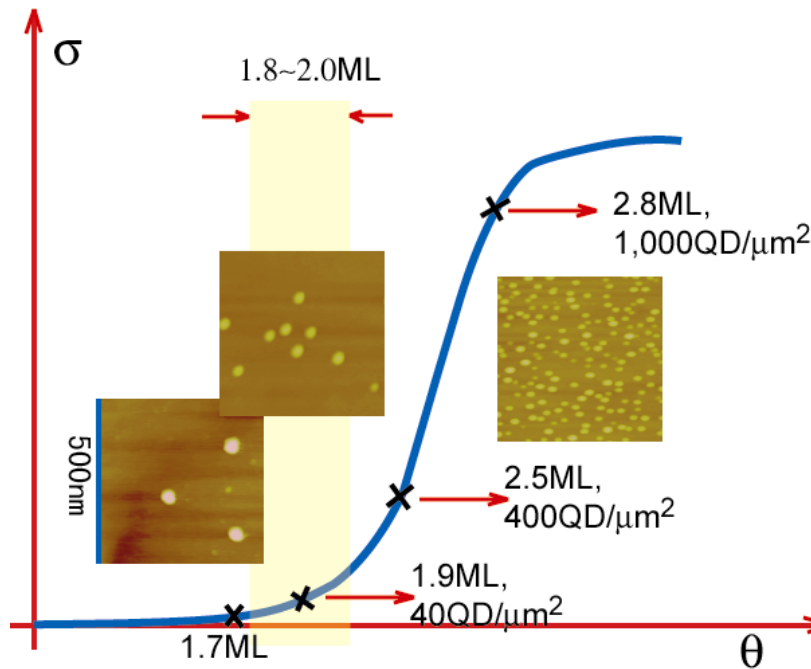


Figure 4-8. The growth condition for the regrowth. Normally a growth temperature of 500 degree C and an InAs coverage of 1.8~2.0ML are used.

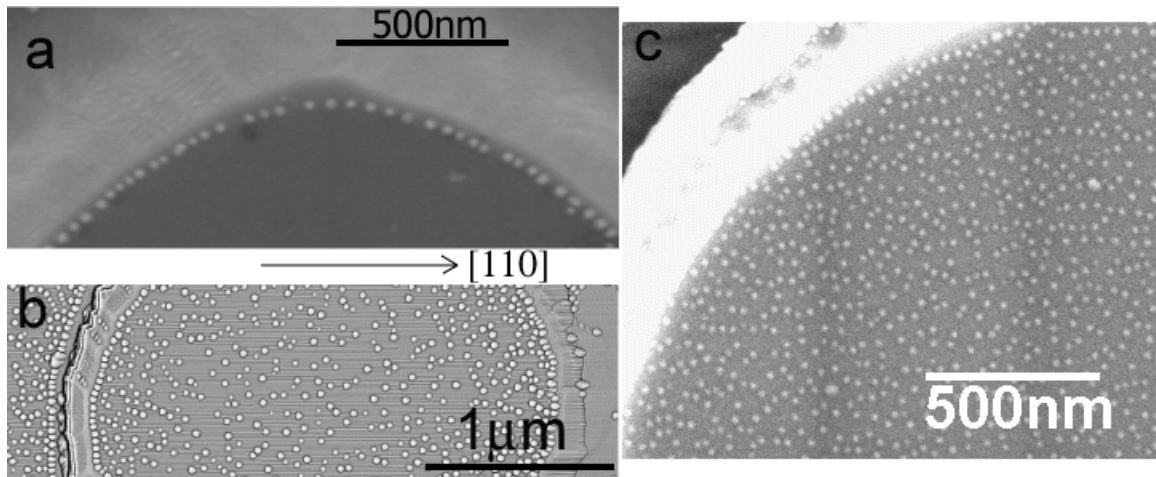


Figure 4-9. MBE regrowth on circular mesa structures. (a) The growth temperature is 500 °C. QDs only appear at the lithographic edge. (b) The growth temperature is 480 °C, just 20 degree lower, and QDs show up on the whole top surface with the area density lower at the mesa center. (c) The growth temperature is 500°C, but the InAs coverage changes from 1.9ML to 2.5ML. Again, QDs are everywhere on the top surface.

After one-hour high temperature annealing, a buffer layer of 35nm GaAs, 1.9ML InAs were sequentially grown on the substrate at a temperature of 500 °C. At this growth temperature, we typically get an area density of 10 QDs/ μm^2 , and we can see from Figure 4-9a that typically QDs only show up close to the lithographic edge. Here, material migration plays an important role in the QD preferential formation. At our growth conditions, with a substrate temperature of 500 °C and an As/Ga flux ratio of 30, a diffusion length on the order of one μm can be estimated. Hence, for the sizes of the circular mesas used, we see no substantial QD distribution in the center area of the mesa. With a increasing of InAs coverage, we noticed that QDs first fill up the edge before they appears elsewhere. For comparison, an AFM image of QDs distribution at a growth temperature of 480 °C is presented in Figure 4-9b. We can see that QDs appear almost everywhere but the density decreases from the edge to the center. So with a diffusion length of tens of nanometers, it is less obvious that the QDs are aligned with the lithographic edge. The spatial alignment will break also in the high InAs coverage region (Figure 4-9c). So this QDs nucleation at the edge only works in the near to critical coverage regime.

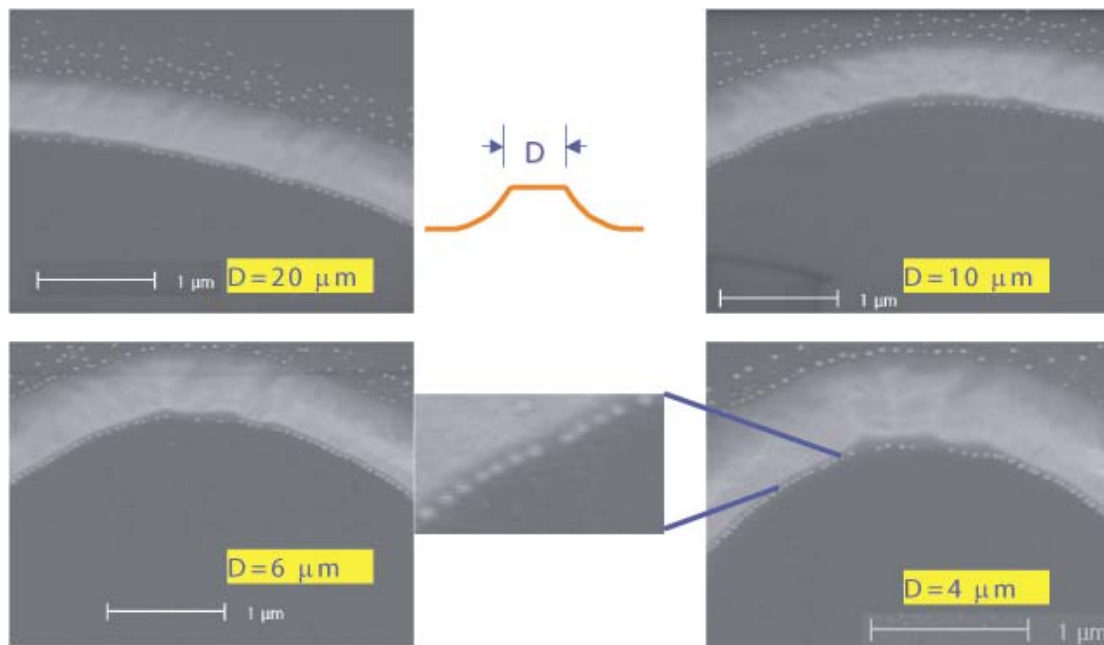


Figure 4.10. Regrowth on mesa structures with different diameters.

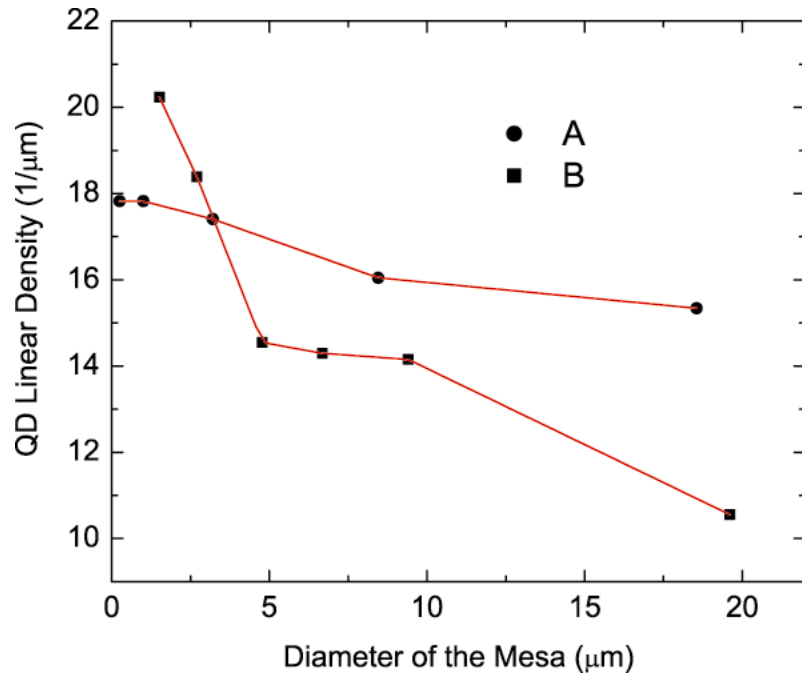


Figure 4-11. Average linear density of QDs at the mesa edge. On Sample “A”, the etching depth is about 500 nm, while on Sample “B”, the etching depth is 1 μm . On both samples, the linear density slightly increases with the decrease of the mesa diameter.

Besides the diffusion length, the sidewall of the mesa plays an important role in the QD formation. The InAs material will not only migrate from the top of the mesa but also from the sidewall. To prove this, we apply the QD linear density as a “gauge” to measure the InAs migration. We prepared two samples: sample A with an etching depth of 500 nm and sample B with an etching depth of 1 μm . If InAs does migrate from the sidewall, we expect to see a linear density increase with a shrinking of the mesa sizes. We notice that it is true on both sample A and B. When both the sidewall and top surfaces are present and the In adatoms migrate faster on the side wall ((101) surface for example) than the top surface ((001) surface), we will see InAs segregation on the top surface close to the edge. All the above analyses are based on an isotropic distribution. However, the migration could also depend on the crystal orientation. In Figure 4-12 we show the QDs distribution for 4 different crystal orientations ([100], [010], [-100] and [0-10]). We can see that there is a special crystal orientation ([100]), where QDs will also appear in the vicinity of the edge.

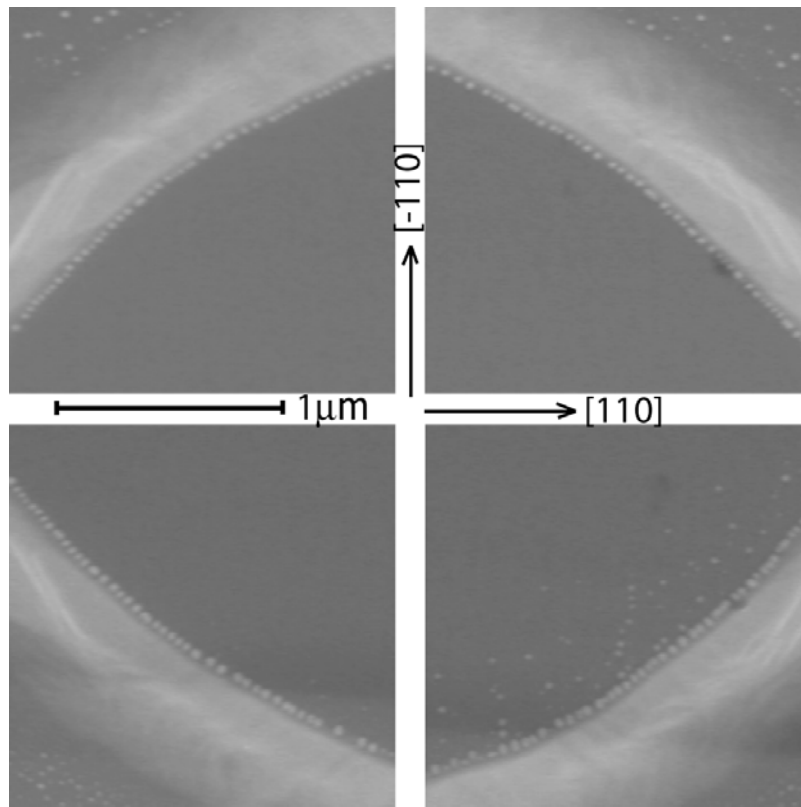


Figure 4-12. The QD linear density dependence on the crystal orientation. The QDs distribution is almost uniform along the mesa edge. However, owing to non-inversion symmetry, QD alignment with the edge is relatively poor between $[110]$ and $[1 -10]$ direction.

To make clear the role of the sidewall for the diffusion of In adatoms, we design another series of samples beginning with 100 nm of GaAs on top of a 600 nm $\text{Ga}_{0.3}\text{Al}_{0.7}\text{As}$ layer. In contrast with the samples described above, we apply a selective etch to make an undercut after the nonselective etch of $\text{H}_3\text{PO}_4:\text{H}_2\text{O}_2$. In this case, we make disk-like structures instead of the circular mesa. The purpose of the undercut is to determine the sidewall contribution to InAs migration. With the fixed GaAs top layer (a thickness of 100 nm) and same kind of sidewall tilt, we see a big difference in the QD density between the small and big disk samples. These results are discussed in next section. On small disk sample ($\sim 3\mu\text{m}$), we obtain a linear density as low as 0.5 QDs/ μm . This further supports our conclusion that the In sidewall contribution is at least as

important as the material migration from the top surface in mesa structures (without undercuts).

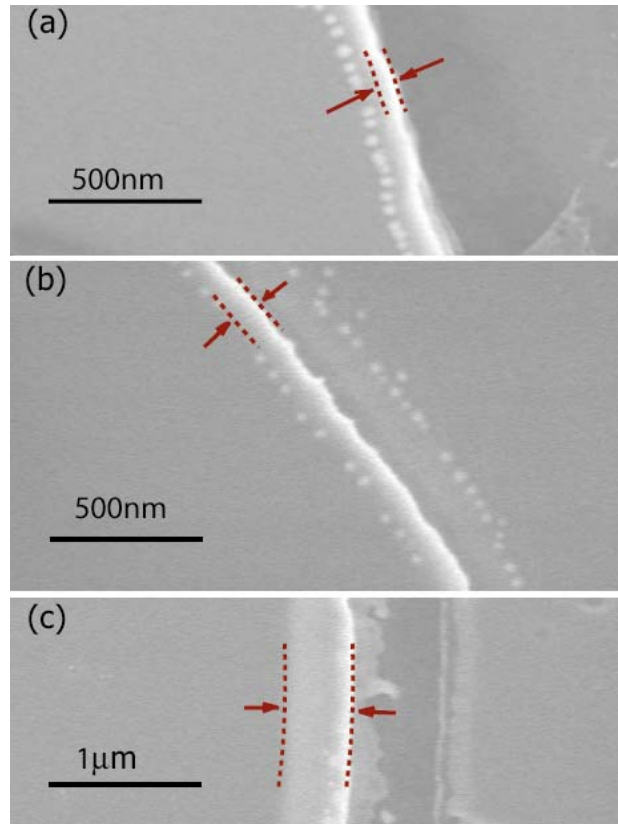


Figure 4-13. The QD linear density dependence on the tilt of the sidewall. The sidewall is about 80 nm wide in (a), 150 nm wide in (b) and 600 nm wide in (c). For all three samples with undercut, the GaAs top layer is about 100 nm thick.

For the above comparison between disk and mesa samples, the tilt of the sidewall is the same (very close to 45 degrees). In our definition 90 degrees means a completely straight sidewall. However, it is possible to adjust the sidewall tilt using chemical etching and MBE growth. Figure 4-13 shows how the QD density depends on the sidewall tilt. With the same top layer thickness of 100 nm, the lateral widths of the sidewall are 80 nm in (a), 150 nm in (b) and 600 nm in (c). The disk diameters are 20 μm for all three cases. We can see that the QD density is highest in (a), a bit lower in (b) and almost no dots in (c) while the growth conditions are the same. In case (c), instead of providing In adatom flux,

there will be a net out-flow of In adatoms because of better strain relaxation on (001) vicinal surfaces.

With the complete control of QD growth, we capped the QDs with an additional 100nm of GaAs layer and make optical measurement. The top layer will be grown at the same temperature for the QDs growth. Figure 4-14 shows the clear facets show up at a high growth temperature of 585°C, which is the normal temperature for GaAs growth. However this temperature is too high for the application of optical cavity where a smooth profile is required. However, too low growth temperature will generate a high density of growth defects, introducing additional non-radiative recombination mechanism. So we would fix the growth temperature to a medium temperature of 490~500°C.

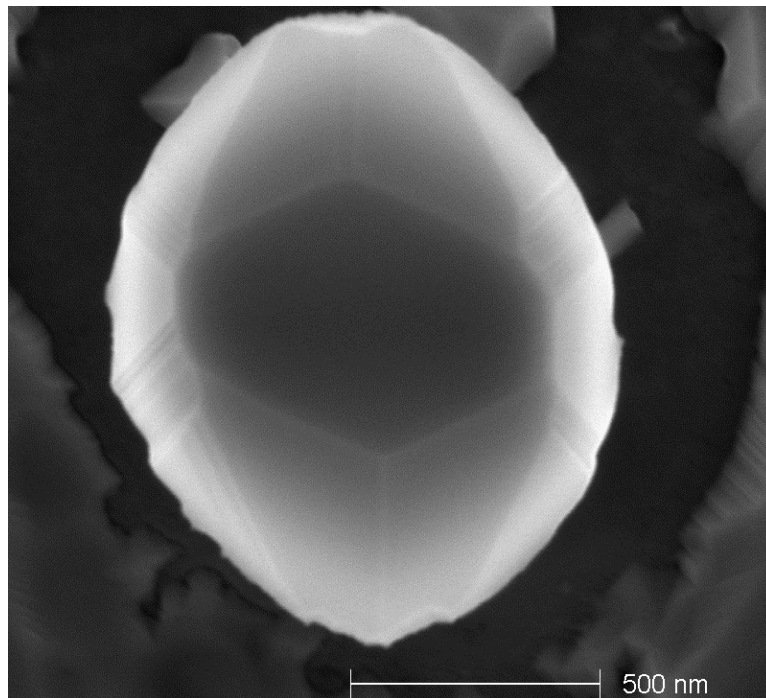


Figure 4-14. Crystal facets show up at the edge of regrowth feature (post or disk). The growth temperature is 585 degree C.

The sample was installed in an angle-pumped and He-flow cryostat. The projection of a pinhole limits the Photoluminescence (PL) to that from a 5 μ m wide region. Figure 4-15a shows a CCD image of several spatially very close disk sample. On top of the disk, only PL from the edge is observed. However in between the disks, occasionally we also

see the QDs PL emission from the bottom, but far away from the edge. Figure 4-15b shows a typical PL spectrum from a 25 μm disk sample. The wetting layer signal is at 850 nm, while QDs signals are between 890nm and 940nm and the sharp peaks corresponding to signals from individual QDs. The detail PL measurement will be discussed in the next chapter.

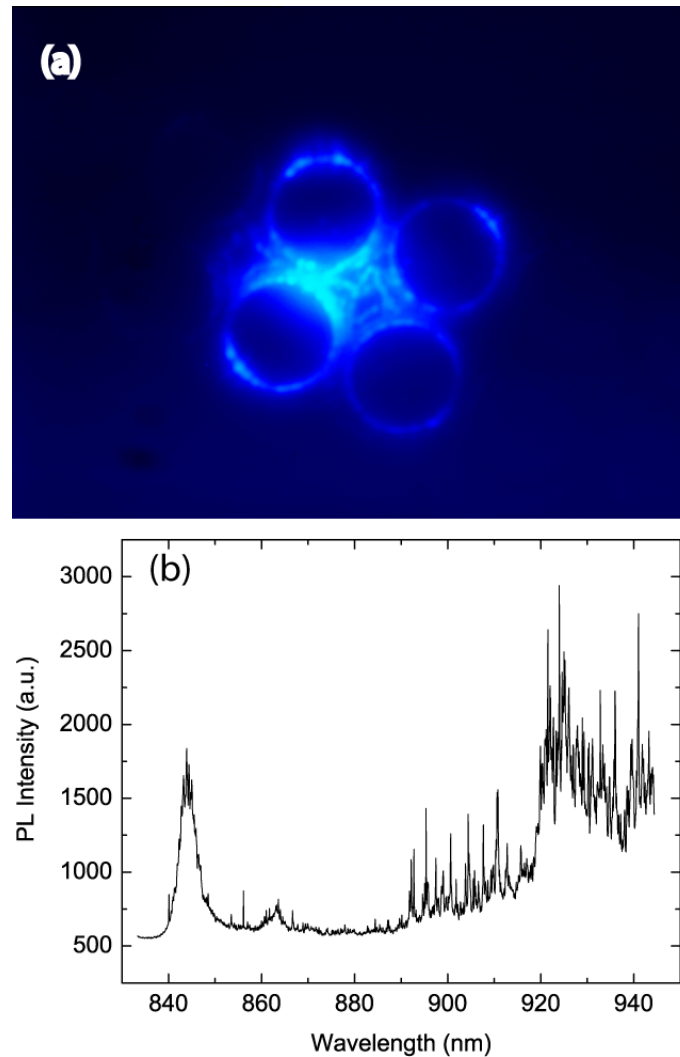


Figure 4-15. (a) The CCD image of PL from several 15 μm disk samples very close to each other. (b) A typical PL from the edge of a 25 μm disk sample, the collection area is limited to 5 μm . According to AFM or SEM observations, there should be ~ 50 QDs in the spectrum range of 890~940nm.

In summary, we have discussed the growth conditions necessary to place QDs at the lithographic edge of patterned structures. The regrowth mechanism is explored in

experimental detail. Besides the influence of the mesa size and crystal orientation on the QD density, we discussed the role of the sidewall including the length and tilt. With these geometric factors as well as growth parameters, it is possible to control the QDs density in a useful optical device such as a microdisk cavity.

4.3. MBE regrowth on a partial microdisk cavity

In this section, we demonstrate the localization of optically active and polarization ordered InAs quantum dots in the narrow whispering gallery mode region of a GaAs microdisk cavity. This is achieved through preferential In adatom surface diffusion on a partial cavity structure in a way that can be generalized to other optical cavities. In agreement with our model, and contrary to regrowth on mesa structures, we observe decreasing perimeter quantum dot densities with decreasing microdisk diameters.

The spontaneous formation of semiconductor quantum dots (QDs) using various crystal growth processes have been used to great success for the last decade in areas spanning optical biological tags [64], ultra low threshold lasers [65] and high-efficiency single photon sources [3]. While, these bottom-up approaches hold tremendous promise, an outstanding issue is the integration of QDs into mesoscopic device architectures. This is particularly important for an emerging class of optical and spin-based structures for quantum information processing [66] [67], based on primarily isolated InAs QDs, for example, triggered single photon sources [56] [3] or cavity mediated spin interactions [68]. To increase the single photon train extraction efficiency or mediate the interaction between QD states a microcavity is used [69]. The interaction between the cavity mode and QD is determined by the spectral, spatial coupling, and polarization overlap [70]. While the spectral matching between the QD and a cavity mode can be measured and to some extent tuned, the spatial alignment and polarization are fixed from the QD crystal growth and is typically random. Thus, the location of the QD in the microcavity is an important constraint, as well as the alignment of the QD emission and cavity mode polarizations.

Several research groups have used a variety of lithographic patterning and regrowth to obtain spatial positioned QDs. These include patterning in holes [71] and on mesas [72].

Mui *et al.* [73] predicted that the surface migration induced preferential edge nucleation of QDs, and this approach has recently been generalized to a variety of structures [74] [75]. However, an approach has not been developed which can locate QDs in highly spatially dependent optical cavities. Here, we place InAs QDs at the anti-nodes region of cavity modes based on a new regrowth approach. The cavity is a GaAs microdisk, where light is emitted in the disk plane. For a cavity resonance near 1 μm , the cavity mode region is limited to a narrow approximately 300 nm region near the disk edge. If QDs are randomly oriented in the disk plane, most QDs are not positioned in the narrow cavity mode region and the coupling will be poor [76] [77]. We analyze the regrowth of InAs QDs on microdisks of varying sizes and elucidate a connection between the QD spatial ordering and the In adatom migration, allowing us to control the density and size of the spatially aligned QDs. We fabricate microdisks with QDs positioned in the cavity mode region. In the next chapter, we will demonstrate isolated QD exciton emission with polarizations aligned with the TE cavity mode polarization.

All structures were grown by molecular-beam-epitaxy (MBE) and initially consist of a GaAs buffer layer, 500 nm of $\text{Al}_{0.7}\text{Ga}_{0.3}\text{As}$ layer and 100 nm GaAs. Standard optical lithography and a two-step wet chemical etch was used to define the microdisks. A nonselective etch of phosphoric acid and peroxide was followed by an AlGaAs selective etch of dilute buffered oxide etcher (BOE). The photoresist was then stripped, the samples were cleaned in standard solvents, and a final etch of $\text{NH}_4\text{OH}:\text{H}_2\text{O}_2:\text{H}_2\text{O}=1:1:70$ removed approximately 50 nm of GaAs. The samples were reinserted into the MBE chamber for regrowth consisting of 50 nm of GaAs, 1.9 monolayers (MLs) of InAs and the 100 nm top half of the cavity, all at 500 $^\circ\text{C}$, under As_2 flux. Scanning Electron Microscopy (SEM) images of the microdisk before and after the regrowth are shown in Figure 4-16.

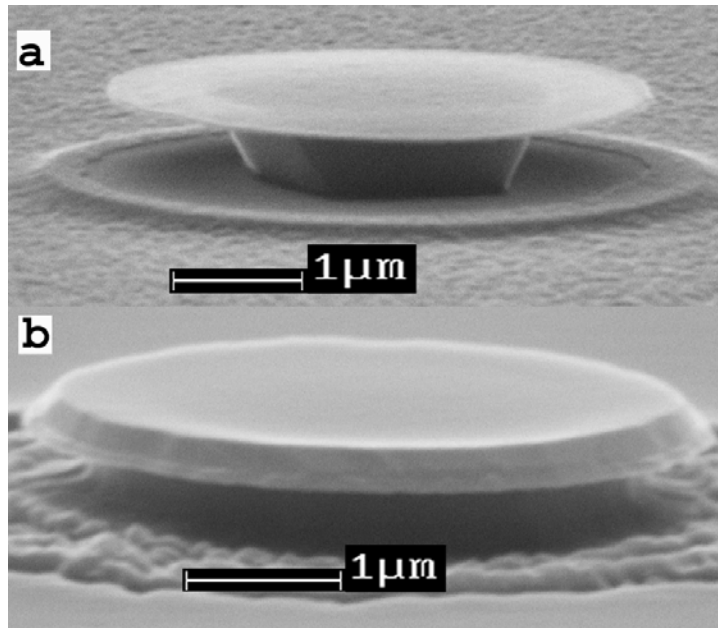


Figure 4-16. (a) SEM of the microdisk sample before regrowth, with a top layer thickness of ~ 50 nm and a diameter of 4 μm . (b) The microdisk sample after regrowth, with a total thickness of 200–250 nm.

The QD distribution was investigated in samples without the top cavity using SEM and Atomic Force Microscopy (AFM). Results are shown in Figure 4-17. In strain induced InAs QD formation, QDs form in regions where the InAs coverage, θ exceeds the critical coverage, θ_c . Under our growth condition θ_c is approximately 1.8 ML. The InAs coverage (1.9 ML) is just above the critical coverage, and in an unprocessed control sample this coverage corresponds to a QD density of $10 \text{ QDs}/\mu\text{m}^2$. However, we observe no significant number of QDs except at the disk edge region of the structures, even in the largest (50 μm diameter) disks. Based on this observation and our analysis below, we conclude that the patterning modify the local InAs coverage through In adatom migration from the center to the edge. In the center region of the disk the on-set of QD formation is delayed with respect to QD formation at the edges. Furthermore, Figure 4-17 shows that the linear density of QDs at the disk perimeter is a strong function of the disk diameter. Smaller diameter disks (Figure 4-17a) have smaller linear densities than larger diameter disks (Figure 4-17b). These observations are summarized in the experimental data in Figure 4-17d.

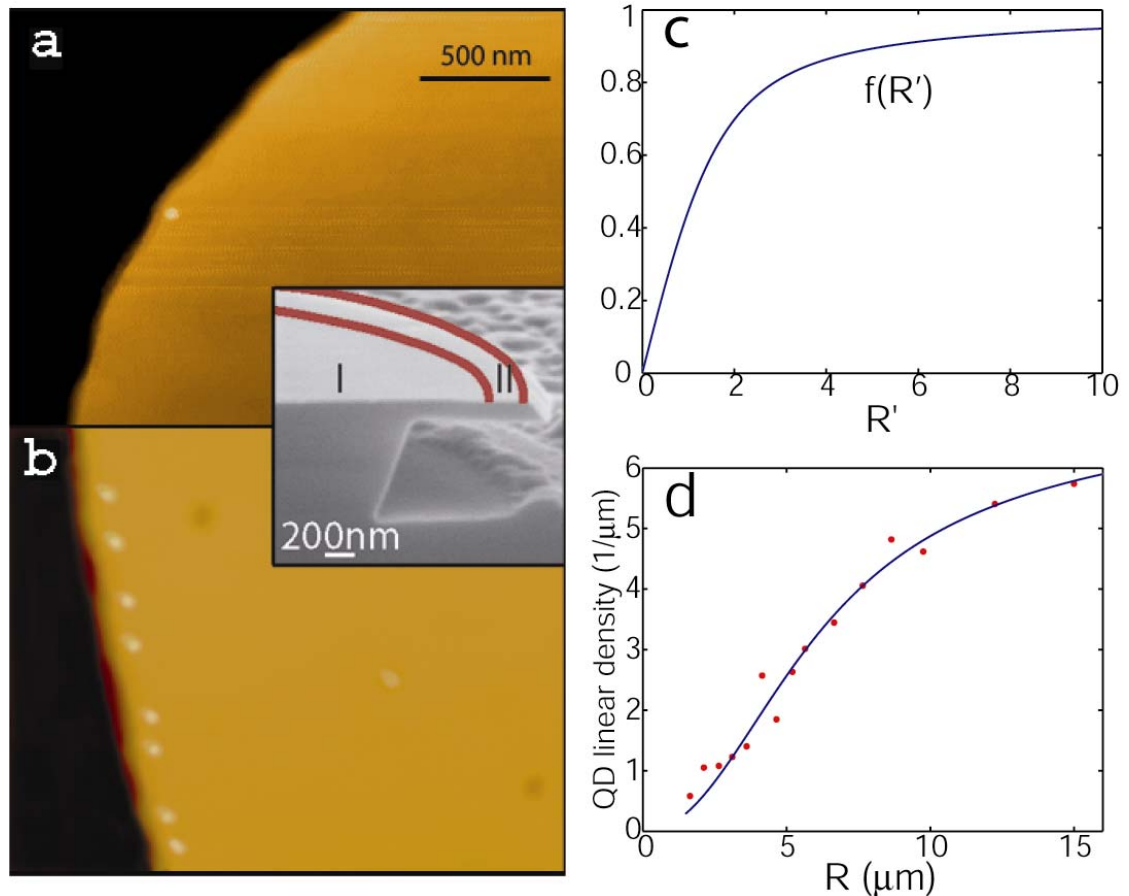


Figure 4-17. (a) An AFM image of 5 mm disk showing one QD at the disk edge. The QDs width and height are approximately 40 nm and 5nm, respectively. (b) An AFM image of the 30 mm disk, using the same scale, showing several QDs aligned at the disk edge. Insert: The SEM image of the disk cross-section shows the sidewall of the disk is 45° tilted. We denote the edge region as Region II and the non-edge region as Region I. (c) Plot of the function $f(R')$ versus R' , where $R'=R/\lambda$. (d) The QDs density versus the disk diameter. The linear QD density approaches 7.6 QDs/mm for large disks and zero for small disks. The line is the fitting result based on our model (see text).

It has been shown that free surfaces, such as our disk edges, are sinks for surface steps leading to a highly stepped edge [78], and aiding 2D step-flow growth and presumably QD nucleation [79]. In addition, the edge of the disk surface relaxes lattice mismatch strain more than the disk interior. All of these processes create lateral In adatom diffusion. Thus, qualitatively the edge region can locally exceeds θ_c before the center region. The QDs densities at the edge will depend on the usual growth parameter factors, as well as

the lateral diffusion length, λ . Furthermore, microdisks with radius below λ will have substantially lower perimeter QD densities than microdisks with radius above λ .

In developing a quantitative model to analyze the QD formation on patterned microdisk, we assume distinct diffusion regimes below and above θ_c . Below θ_c , the In adatom density, n is approximately uniform and the lateral flux, q to the disk edge is small compared to above θ_c . However, when θ just exceeds θ_c , it does so initially near the edge and QDs form in a narrow edge region characterized by a width t_0 , denoted Region II in Figure 4-17. Condensation of adatoms in region II introduces In adatom depletion at the boundary of Region I and II. In adatoms diffuse to a surface lattice site with a lifetime τ , and neglecting desorption the In adatoms diffusion equation is

$$-D \cdot \nabla^2 n + \frac{n}{\tau} = J, \quad (4.1)$$

where D is the In adatom diffusion constant which is assumed independent of crystal orientation, and J is the InAs deposition rate. We solve Eqn (4.1) to obtain the In adatom distribution over the non-edge Region I of the disk defined by $(R-t_0)$, where R is the disk radius. We assume that above θ_c n is essentially zero at the outer boundary of Region I. Since $t_0 \ll R$, we set $r=R$ as the boundary and Eqn (4.1) can be solved as

$$n(r) = J \cdot \tau - A \cdot J_0(i \cdot r') / J_0(i \cdot R'), \quad (4.2)$$

where A is a constant, $J_0(x)$ is Bessel function with an imaginary variance, r' and R' are the normalized radii ($r'=r/\lambda$ and $R'=R/\lambda$) and $\lambda = \sqrt{D \cdot \tau}$. The In adatoms flux across the outer boundary of Region I is

$$q = -D \cdot \frac{dn(r)}{dr} \Big|_{r=R} = \frac{DA}{\lambda} \cdot \frac{J_1(i \cdot R')}{i \cdot J_0(i \cdot R')}. \quad (4.3)$$

We can relate the material migration with the local InAs coverage at the edge as

$$(\theta - \theta_c)_{edge} \propto q \quad (4.4)$$

Finally, the variation in the density of QDs with surface coverage can be expressed as $\rho = \rho_0(\theta - \theta_c)^\alpha$ [80]. Since we observe only one row of QDs within the fixed width t_0 of the perimeter, we use the linear density, σ and find

$$\sigma = \sigma_\infty \cdot f(R')^\alpha \text{ and } f(R') = \frac{J_1(i \cdot R')}{i \cdot J_0(i \cdot R')}, \quad (4.5)$$

where $f(R') \rightarrow 1$ in the limit $R' \rightarrow +\infty$. $f(R')$ is shown in Figure 4-17c. Using our experimental data from microdisks with diameters varying from 3 to 30 μm , we fit the QDs density and obtain $\lambda = (3.2 \pm 0.4)\mu\text{m}$, $\alpha = (2.2 \pm 0.3)$ and $\sigma_\infty = (7.6 \pm 2.1)/\mu\text{m}$, where the exponential factor α is close to the value reported in reference [19]. The model and data are shown in Figure 4-17d, where the solid line represents the model.

Our FDTD calculations show that the fundamental $\text{TE}_{m,1}$ and $\text{TM}_{m,1}$ cavity modes are centered about 100 nm from the edge. We grow and process samples, according to the initial procedure, with the GaAs top layer. The final microdisk thickness is 200~250 nm. The disk edge has a 45° tilt from the growth dynamics [81], but is otherwise smooth (Figure 4-16 and Figure. 4-17). The sidewall tilt allows for lateral growth and the possibility of tuning the disk edge – QDs distance by adjusting the over layer thickness. The 45-degree tilted sidewall slightly degrades the cavity Q (Chapter 2), but also makes the top collection easily.

We have shown a method that combines self-assembled growth and simple processing to spatially align QDs in the optical mode region of a microdisk cavity. We have discussed the growth mechanics of QDs by this patterned regrowth process, and propose that the regrowth on the microdisk modifies the local InAs coverage, thus increasing the local QDs density at the disk edge. In the next chapter, we will use micro-PL measurement to show that QDs in our regrowth sample are optically active. We observe single exciton and biexciton emission as well as emission from the cavity mode. We expect that this process can be used to more efficiently couple single QDs and cavity modes for a variety of devices and applications.

Chapter 5. Optical Measurement on Regrowth Samples

This Chapter will talk about the general characters of PL spectrum from regrowth QDs. There is a broad range of discussions on self-assembled QDs, including the growth and optical properties. However, very few are taking about regrowth QDs, especially isolated QDs from regrowth, not mention of possible applications in optics. The reason is QDs from regrowth have relatively more complicate spectral structures, variable in the quality due to a variable of cleaning techniques. In this chapter, we will show high quality QDs embedded in the regrowth microdisk. The first section will focus on the isolated QDs, including neutral exciton, charged excitons and multi-exciton identification. Then the measurement will extend to time-resolution PL measurement. According to the lifetime measurement, we present a model to explain the carriers diffusion and capture process, uniquely to the regrowth QDs. In the third section, WGM modes in the regrowth microdisk are identified. Finally, possible cavity coupling effects are presented.

5.1. PL from isolated QDs

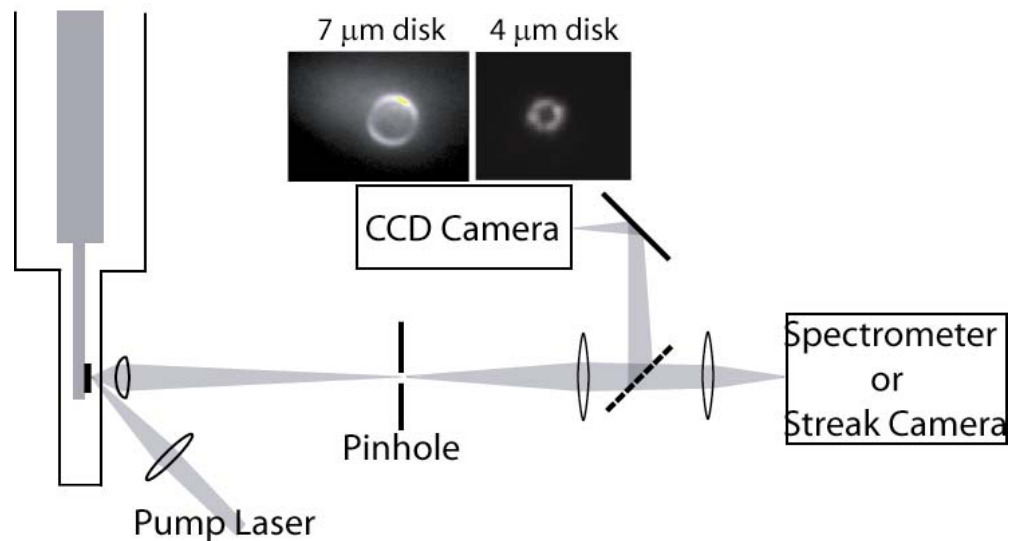


Figure 5-1. PL measurement setup.

Micro-PL measurements were made on a variety of microdisks with diameters ranging from 3 to 30 μm , and undercuts ranging from 0.3 to 1 μm . The sample was mounted in a He-flow cryostat and unless noted all measurements were done at $\sim 7\text{K}$. A tunable Ti-sapphire laser emitting between 750-900 nm or a semiconductor laser emitting at 670 nm were used as the pump source. The pump is incident at approximately 45° to the sample and focused to a 20~30 μm diameter spot. The collecting optics were aligned normal to the sample and employed confocal imaging with a collection diameter of 5 μm . Although emission from the microdisk is in plane, enough light is scattered to allow vertical collection. The collected PL was dispersed by a 50 cm spectrometer with a spectral resolution of 70 μeV , imaged with a CCD monitor capable of imaging single QD emission, or measured in the time-domain using a streak camera with 30 ps resolution. Normally on our regrown samples there is a broad wetting layer feature centered at approximately 850nm and QDs emission between 890~940nm (Figure 5-2a). PL Measurements on disks of various sizes using the aperture as a spatial filter indicate that all the QDs emission is from the disk-edge region. For large disks, we adjusted the disk edge close to the center of the collection aperture, while small disks were centered inside the aperture. In agreement with our earlier SEM and AFM results, on small disks there are typically one to three QD emission spots in the CCD image and located at the edge, while on large disks the QD emission at the edge was almost continuous. Typical PL spectra for large and small disks are shown in Figure 5-2a. From the SEM and AFM results on the uncapped disks, QDs form at the top disk edge as well as the bottom etched AlGaAs surface; however, the bottoms QDs are typically optically inactive, being regrown on the etched AlGaAs surface where non-radiative recombination dominates. Furthermore, by adjusting the AlGaAs layer thickness and etching depth, we control the lateral offset of bottom QDs from the disk edge to be at least 1 μm (Figures in the last chapter), so the collecting aperture can spatially filter any remaining emission. On small disks ($\sim 3 \mu\text{m}$) the density of QDs is low enough to align only a few dots (usually 1~3) in the vicinity of the microdisk cavity. A high-resolution spectrum of a 3 μm diameter disk containing distinct QD emission lines is shown in Figure 5-2b. These emission lines correspond to a single bright emission spot in our CCD image. The pump wavelength is 860nm, pumping into the quasi-continuous states of the QD. By varying the incident

pump power we can determine the excitonic or biexcitonic nature of emission lines, labeled “a” and “b”. Peak “a” (centered at 916.65 nm) shows linear dependence on the pumping power while peak “b”, 3.4 meV below “a”, shows quadratic dependence on the pumping power. Using a streak camera we measured the lifetime of QD peak “a” to be 940 ps, which is typical for our self-assembled QDs prepared without regrowth [82].

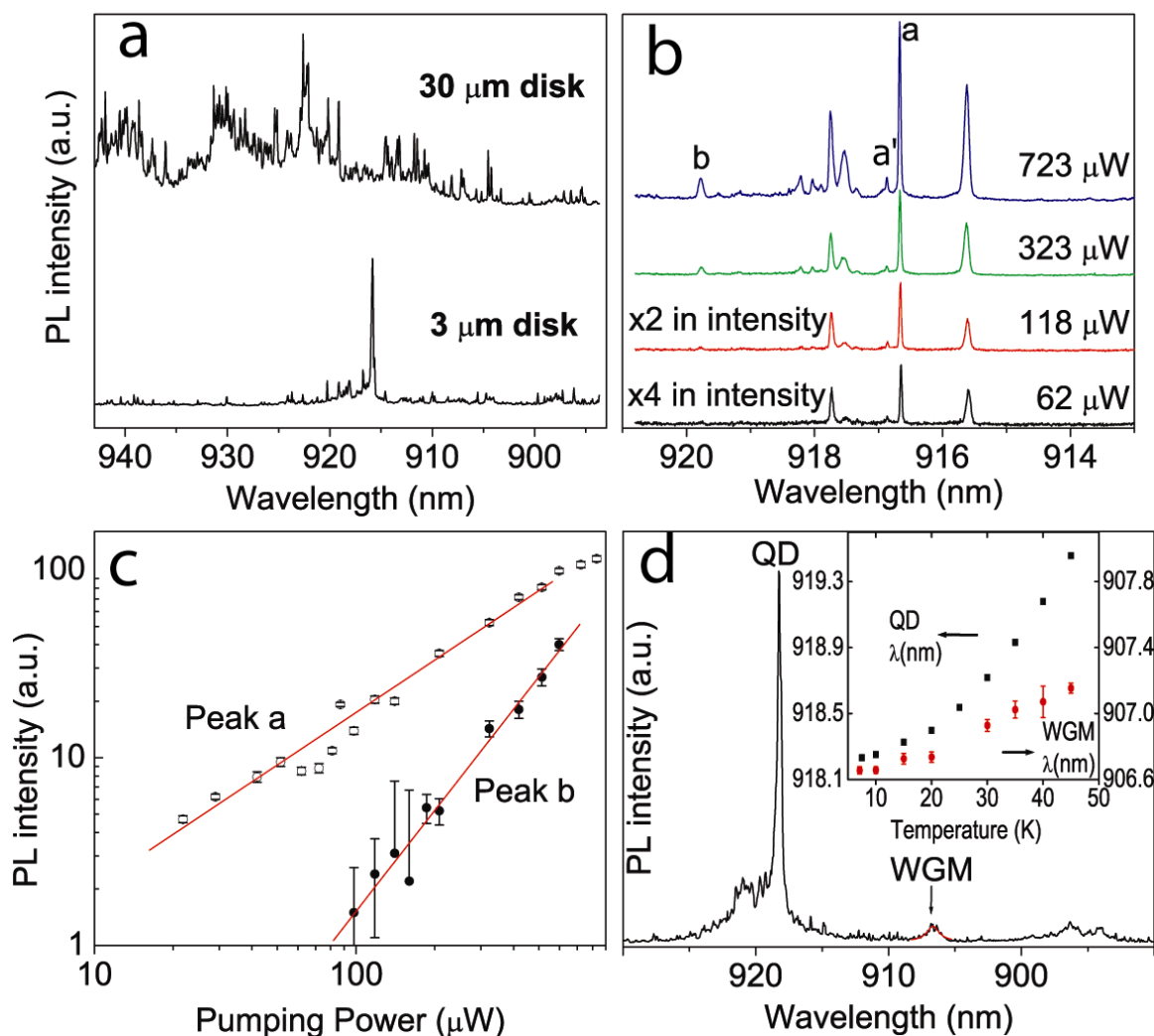


Figure 5-3. (a) PL spectrum from a 3 μm diameter and 30 μm disk, pumped by a cw 670nm semiconductor laser. The pump power is 1 μW . (b) The 3 μm diameter microdisk, pumped using a cw Ti-sapphire at 860nm, under different pump powers. (c) The pump power dependence for peaks “a” and “b”. (d) The PL spectrum of a typical QD and WGM. The insert shows the temperature-tuning curve of the QD and WGM.

The excitonic peak “a” is linearly polarized as is typical [83]. However, the orientation of the polarization is strongly related to the orientation of the disk. Possibly due to the regrowth process, we typically see a big split of ~ 300 meV between two exciton peaks with orthogonal polarization. Their excitation can be selectively enhanced by adjusting the polarization of 860nm pumping. As shown in Figure 5-3, Peak a is strongly tangentially polarized, while peak a’ is radially polarized. Since the TE cavity modes have in-plane tangential polarization, the exciton emission polarization basis is optimally oriented.

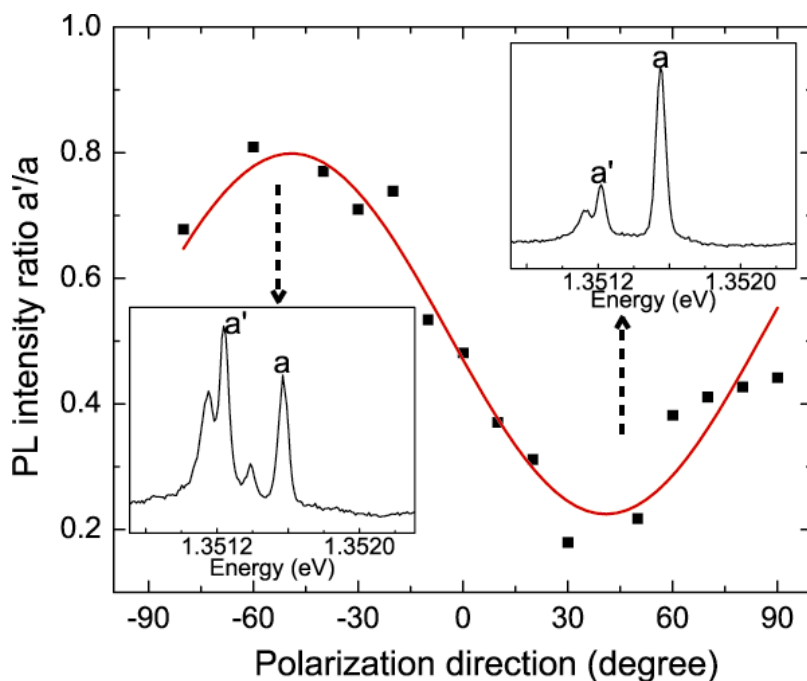


Figure 5-3. The PL intensity ratio between two orthogonally polarized exciton peaks from one QD. Peak a’ is radially polarized, while peak a is tangentially polarized.

To distinguish between uncoupled single QD emission and cavity mode emission [84], we have made temperature dependant PL measurements. With increasing sample temperature, the QD emission shifts to longer wavelength as the semiconductor band gap is reduced, while the cavity mode emission line is determined by the optical path length of the disk and shifts much less. Figure 5-2d shows a PL spectrum containing a single QD exciton emission line and the emission from a cavity mode. Typically from 7 K to 45 K, we see a wavelength shift of 1.3 nm for the exciton line, and a 0.5 nm shift for the

cavity mode. Cavity Q values are typically 2000 and agrees with our FDTD calculation. The cavity Q is also confirmed by measuring the filtered spontaneous emission from the wetting layer.

We have shown a method that combines self-assembled growth and simple processing to spatially align QDs in the optical mode region of a microdisk cavity. We have discussed the growth mechanics of QDs by this patterned regrowth process, and propose that the regrowth on the microdisk modifies the local InAs coverage, thus increasing the local QDs density at the disk edge. Micro-PL measurement shows that QDs in our regrowth sample are optically active. We observe single exciton and biexciton emission as well as emission from the cavity mode. We expect that this process can be used to more efficiently couple single QDs and cavity modes for a variety of devices and applications.

5.2. Large splitting in the neutral exciton emission

Semiconductor self-assembled quantum dots (SAQD), due to their sharp atom-like states and solid state based approach, are of great interest for future quantum information processing devices [4] [85]. In such a nano-scale structures, electrons and holes are confined by the 3D confinement as well as the many-body interaction. A series of theoretical and experimental tasks have already been taken to make clear the confinement states in the SAD [86] [87] [88], such as single exciton, bi-exciton and charged excitation. From theoretical point of view, the fully developed techniques in atom and molecular system can be successfully applied to the SAD research. This kind of knowledge make the fully manipulation of SAD possible, which pave the way for the future device application.

Just like a real atom, when a SAQD is placed into a special chemical or physical environment, its energy level will be unavoidably disturbed. For a long time, this is not a big issue, since people only focused on the properties based on an ensemble of QDs. It is not until recently that single QD devices, one QD under electrical gates or one QD in an optical microcavity, are under significant consideration. Basically there are some ways to isolate SAQD into individual devices. One is bottom-up approach, that is, lithography is

used to selectively keep the QDs under a small area with the removal of other QDs. Another approach is to selectively grow QDs on a patterned surface. There are some discussions about the influence of surrounding environments to the properties of SAQD, such as dopants relation to charged exciton formation, or phonon-broadening of QDs peak in a sub-micron mesa. But most of them are for the QDs isolated under the first approach, while QDs prepared under the second approach, very little research is carried out.

For application of triggered single photon sources, we typically grow InAs QDs at low coverage and higher temperature to achieve isolated QDs. QDs grown at this condition will have a lateral size of 40~50 nm and a height of 5~15 nm. A lens shape approximation means D_{2d} symmetry and an inherent inplane rotation symmetry brings a bright and dark exciton [89] with double degeneracy for each QD. However, the symmetry can be broken and the double degeneracy will be lifted if QDs are placed under external magnetic or electric field. Here, we will show there is inherent symmetry broken for QDs grown on a template with anisotropic strain distribution.

In this section, we will take about the Photoluminescence (PL) signature of InAs QDs buried in a GaAs microdisk, about 100 nm to the disk edge. The materials studied here are prepared by molecular beam epitaxy (MBE). A thin GaAs layer (40~50 nm thick) sitting on an AlGaAs pedal, with an undercut of 200~800 nm is prepared by chemical etching and optical lithography. A thin layer of GaAs was removed before the sample was inserted back MBE chamber for regrowth. Following a 40 nm GaAs buffer layer growth, 1.9 ML InAs was deposited at a growth temperature of 500 °C. The InAs QDs will only show up near the top lithography edge. Finally, The QDs were buried under 100 nm thick GaAs layer. Considering the lateral growth, the QDs will be about 100 nm from the disk edge also. The density of QDs will depend on the sizes of the disk, the shape and length of the sidewall. As a comparison, we put the regrowth results on patterned GaAs mesa with the sidewall of same tilt. Mentioned in the previous chapter, the QDs density will be almost constant on the mesa sample, while the density will be much lower on the disk sample with the same diameter. And the density keep decreasing when the disk size shrinks and with a disk diameter of 3~4 μm , we typically get one or two QDs under Atomic Force Microscopy (AFM) investigation.

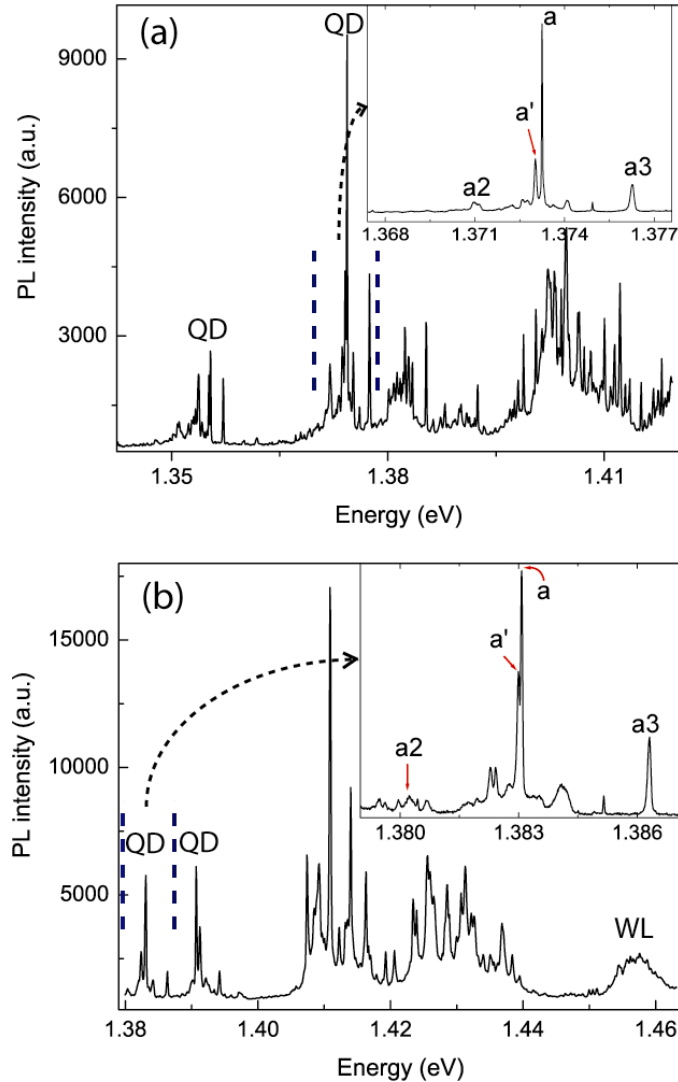


Figure 5-4. (a) A Photoluminescence (PL) spectrum taken from a disk sample A. The insertion shows the fine structure of a QD centered at 1.377 eV. (b) PL for disk sample B. similar signature exists for a QD centered at 1.383 eV.

The sample was mounted in a liquid-He flow cryostat. A microscope objective lens with a NA of 0.5 was used for optical measurement and an angle-pumping scheme was used to screen the scattered laser. An aperture was used to limit the PL only from a $5\mu\text{m}$ region to improve the signal noise ratio. The typical PL is shown in Figure 5-4. At low pumping regime, with above (GaAs) band pumping, we typically observe several isolated QDs peaks with a signature of one major peak and several side peaks around in the wide spectrum scan. With a fine resolution scan, we typically see a fine structure (Peak *a* and

a' with a separation of 70~300 μeV) around the major QD peak and two side bands (Peak $a2$ and $a3$) with a separation of 1.5~2 meV to the major peaks. These PL signature corresponding to one bright spot in the CCD screen and under AFM there is no evidence that QD bunching will happen, so in confidence we accredit the PL signature to one isolated QD. Since at all the temperature region Peak a plus a' always exist and dominates, we believe it relates to single exciton (X). The conditional existing of Peak $a2$ and $a3$ (under limited temperature region and selective pumping) makes us believe it relates to charged excitons (X^+ and X^-). With a physical location close to the edge, the interface-trapped carrier will apply electric field and in turn shifts the QD peak due to quantum stark effect. This effect may shift the whole “signature”, but not an isolate peak, which add confidence that all the signature emissions are really from one single QD. The convolution of Peak a and a' introduces QD peak “broadening” at low resolution scan.

The fine split of single exciton lines comes from the electron-hole (EH) exchange interaction from purely quantum effect. The EH exchange interaction for a QD system with C_{2v} symmetry can be expressed by the effective spin Hamiltonian [90]:

$$H_{ex} = 2\Delta_0 J_z S_z + \Delta_1 (J_x S_x - J_y S_y) + \Delta_2 (J_x S_x + J_y S_y) \quad (5.1)$$

Where $S_z(J_z)$ is the z component of the total electron spin S (hole pseudospin J). J_z takes values of 1/2 and -1/2 corresponding to heavy hole spin of $-3/2$ and $3/2$, respectively. The first term in this Hamiltonian is the isotropic (in-plane) EH exchange interaction, which splits the X_0 into bright states (angular momentum of $m=\pm 1$) and dark states ($m=\pm 2$) with a separation of Δ_0 (a typical value of 300 μeV for InAs QDs). The second term only split the bright states into two orthogonal polarized states:

$$\Gamma_x = \frac{1}{\sqrt{2}} \left(\left| -\frac{1}{2}, \frac{3}{2} \right\rangle + \left| \frac{1}{2}, -\frac{3}{2} \right\rangle \right) \text{ and } \Gamma_y = \frac{1}{\sqrt{2}i} \left(\left| -\frac{1}{2}, \frac{3}{2} \right\rangle + \left| \frac{1}{2}, -\frac{3}{2} \right\rangle \right). \quad (5.2)$$

While the third term only split the dark states into

$$\Gamma_1 = \frac{1}{\sqrt{2}} \left(\left| \frac{1}{2}, \frac{3}{2} \right\rangle + \left| -\frac{1}{2}, -\frac{3}{2} \right\rangle \right) \text{ and } \Gamma_2 = \frac{1}{\sqrt{2}i} \left(\left| \frac{1}{2}, \frac{3}{2} \right\rangle - \left| -\frac{1}{2}, -\frac{3}{2} \right\rangle \right). \quad (5.3)$$

And the separations are Δ_1 and Δ_2 , respectively. For the self-assembled InAs QDs on planar surface, these split are rather small ($<50 \mu\text{eV}$). However, if the QD are elongated or strain inside the QD is anisotropic, this split will be substantially larger. For our

regrowth sample, we would expect the strain in the tangential direction of the disk would differ from that in the radial direction.

Now we only focused on the single exciton peaks and the corresponding split between them. The exciton Peak a is usually tangentially polarized and presented at all pumping conditions and temperature region. Peak a' is usually radially linearly polarized. Both have an ideal FWHM of $<70 \mu\text{eV}$. The separation in Figure 5-4a is $300 \mu\text{eV}$ and the separation in Fig. 5-4b is $70 \mu\text{eV}$. In Figure 5-3, we plot the intensity ratio of Peak a' over Peak a versus the polarizer angle to get rid of error introduced by the fluctuation. The fact that the polarization direction of Peak a' is roughly in the radial direction of the disk is interesting for cavity-QD interaction, this type of polarized X^0 will achieve better coupling.

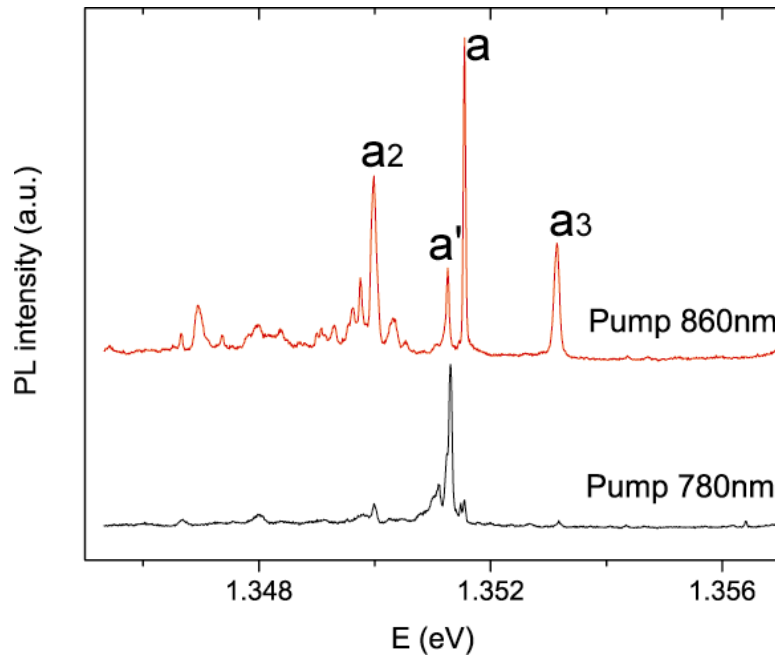


Figure 5-5. The PL spectrum for a disk sample C at a temperature of 8K. (a) The sample is pumped into the quasi-continuous states from wetting layer fluctuations around the disk edge. (b) The sample is pumped with above band pumping.

And according to the character of polarization, we can selectively excite polarized Peak a or Peak a' by controlling the polarization of the pumping laser. For above band pumping, we usually see a mixture of Peak a and a' since the spin or polarization information is lost as

well as energy relaxation from GaAs band-edge to InAs band-edge and all the possible polarization orientations are filled. But if we pump into the quasi-continuous states of the QD, the spin or polarization information is mostly kept. We can express exciton states either in the circular polarized expression:

$$\left| -\frac{1}{2}, \frac{3}{2} \right\rangle \text{ and } \left| \frac{1}{2}, -\frac{3}{2} \right\rangle$$

or in the linear polarized expression Γ_x and Γ_y . In Figure 5-6, we plot the intensity of Peak *a* and Peak *a'* as a function of the polarization angle of the pumping laser. We note “0 degree” as the direction, to which Peak *a* over Peak *a'* achieve maximum and “90 degree” as the direction, to which Peak *a* over Peak *a'* achieve minimum. And there is a conversion between two coordinates (one for pumping laser, and one for the disk coordinate) since we used angle pumping instead of normal incidence pumping. We noticed if the pumping laser is polarized in the tangential direction of the disk, the polarized Peak *a'* will be completely suppressed and in the radial direction, the polarized Peak *a'* will achieve maximum intensity, given the pumping power is fixed.

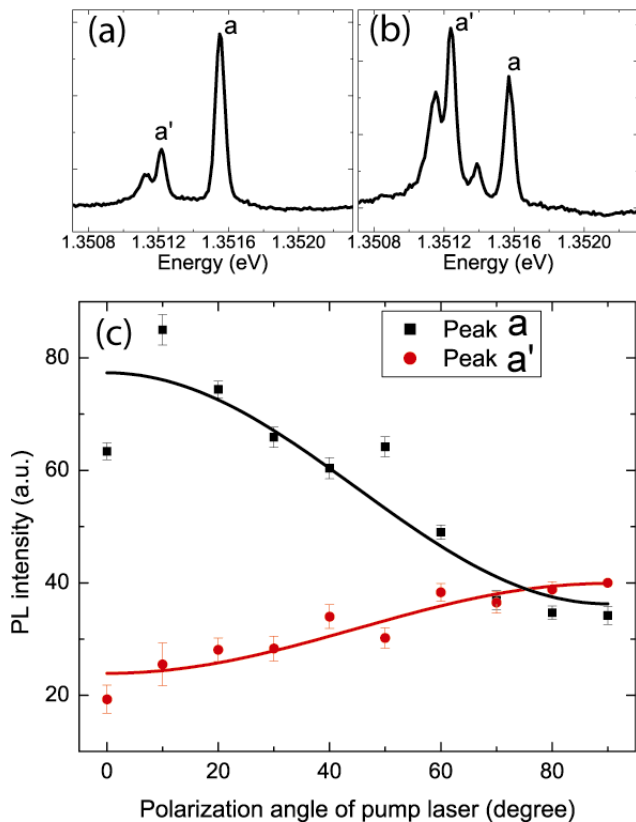


Figure 5-6. (a) The polarization of the pump laser is set to achieve minimum intensity ratio of Peak *b2* over Peak *b1*. (b) The polarization of the pump laser is set to achieve maximum intensity ratio of Peak *b2* over Peak *b1*. (c) The PL intensity of Peak *b1* and *b2* versus the polarization angle of the pumping laser.

Around the disk edge, there is a ring-shaped quasi-continuous distribution of wet layer fluctuations [91]. And QDs are sitting around these wetting layer fluctuations. We noticed that the relative intensity of Peak a and a' would depend on the carriers diffusion path. Most of our measurement is done at low temperature of 8K. If we pumped into these wetting layer fluctuations, the carriers will diffuse in the tangential direction, and hence the tangential polarization will be relatively favored. If above band pumping is used, however, carriers from the radial direction will be dominate since most of the wetting layer fluctuation states also trap carrier and give out radiative emission. In this case, the radial polarization will have better chance to be excited. With the increasing temperature, the shallow confinement no longer effectively trap carrier and tangential diffusion to the QD become dominant. So at a temperature of 40~50K, only Peak a is dominant.

In this section, we talked about the PL signature of regrowth QD buried in a microdisk. In our growth and measurement scheme, isolated QDs can be identified from the spectrum. Through the measurement, a group of sharp peaks, used to be thought as from different QDs, are actually just from one single QD. Unlike group characteristic of QDs, the signature of isolated QDs is very important for electrical or optical mesoscopic devices working on quantum operation. Just as a real atom, the QD is very sensitive to the surrounding chemical and physical environment. In our measurement, we clear identify a split of polarized X^0 peaks, a result of symmetry broken caused by preferential edge nucleation. And furthermore we can selectively excite the exciton states by adjusting the polarization of the pumping probe.

5.3. Life time measurement of isolated QDs

We report time-integrated and time-resolved PL measurements on isolated InAs quantum dots by a self-assembled regrowth process on disk-shaped structures. Due to the regrowth process, these quantum dots are positioned at the lithographically defined disk edge with low density. Based on a simple mono-exponential model, the measured radiative ground-state decay rate of these quantum dots become substantially smaller when the temperature is higher than a threshold of 30K. At these temperatures, the decay rates are significantly smaller than those associated with quantum dots grown on planar

surface at the same growth condition. Our experiment results and rate equation simulation indicate this lower temperature stability comes from coupling to reservoir states. A likely source of this coupling is the ring-like wetting layer fluctuations around the disk edge, which is a result of our regrowth process.

Self-assembled quantum dots (QD) formation is a strain driven phenomena and occurs in a broad range of semiconductor systems, of which SiGe QDs on a silicon substrate, and InAs QDs on a GaAs substrate are two proto-type systems. The growth mode, called the Stranski-Krastanov mode, has been widely discussed. As an example, in the InAs/GaAs QD system, the self-assembled QDs are initially positioned on a thin InAs layer, called the wetting layer. After coverage with GaAs this layer diffuses, burying the QDs in a rough QW [92] [93]. Under optical pumping, carriers are first generated in the bulk GaAs material, then are transported to the thin wetting layer, and finally to the QDs, if no other recombination occur.

Because of their atom-like nature, single QDs at low temperature ($T < 60\text{K}$) are useful for quantum information processing [94] [95]. Radiative recombination and thermal dephasing of QDs excitations are well discussed in this temperature regime and beyond are widely discussed either for an ensemble of QDs or isolated QDs. For the InAs QDs in the typical growth condition, the radiative lifetime is usually constant in the regime of $T < 60\text{K}$ [96] [97].

Recently, QDs regrowth on patterned substrate begin to gain interest as a solution to spatially control the QDs position so that each device contains a specific number of QDs at specific location. With relatively low publication in the field, it is still unclear whether the carriers recombination follows the same rule as the self-assembled QD on planar surface. We have approached this problem using regrowth on a patterned surface.

We introduce a method to spatially embed QDs into a microdisk cavity. Since the cavity mode is located in the disk perimeter region, we locate the QDs close to the edge during growth. We have proposed that long-distance In adatom migration driven by the requirement to minimize the chemical potential, leads to QD nucleation near the disk edge. However, because of the structure at the disk edge, the wetting layer region here is highly stepped with localized variations in thickness. This has been observed for epitaxial lattice mismatched growth on other patterned structures [98]. In this paper we

present evidence for the existence of temperature activated coupling to a reservoir of states. This does not lead to decay through another channel but a recycling of carriers. The carrier recycling is observed as an increase in the mono-exponential radiative lifetime with increasing temperature. This recycling is experimentally reported and theoretically discussed in QDs ensemble grown on planar substrate [99] [100] [101] [102] [103]. Usually the reservoir is thought as wetting layer or nearby QDs with lower confinement. However, because of the complex of ensemble, the measurement results are taken from a mixture of neutral exciton, multi-exciton and charged excitons, not even considering the thermal shift of exciton peaks. In our sample, with clearly isolated exciton emission peak, it is relatively easy to figure out this recycling behavior. We suggest that the reservoir is composed of wetting layer fluctuations whose density is possibly large because of our regrowth process.

Our patterned samples were prepared with Molecular Beam Epitaxy (MBE) growth on GaAs(001) substrate in conjunction with wet chemical etching. The MBE layers consist of a 300 nm GaAs buffer layer, a 500 nm $\text{Al}_{0.7}\text{Ga}_{0.3}\text{As}$ undercut layer for the microdisk pedestal, followed by 100 nm of the GaAs partial cavity layer. Using photolithography, microdisks from 3~50 μm in diameter were patterned. They were defined with first an quasi-isotropic etch and then an undercut of ~500 nm with a selective etch. After chemical cleaning, the samples were reloaded into the MBE chamber. A 35 nm GaAs buffer layer, a 1.9 ML InAs QD layer and an 80 nm GaAs top layer were sequentially grown. To spectrally isolate single QD emission, which is essential for the single photon sources [56] [3] required by quantum information processing, the material deposition should be just above the critical coverage for QD island nucleation. To add additional control, this is often done at a relatively high growth temperature [104]. At these growth conditions, QDs only appear at the disk edge and with a very low linear density (1~3 QDs per disk) for the small disks. For the optical measurement, an angle-pumped, continuous He flow crystal setup was utilized. A pinhole aperture was put at the conjugate position of the investigated disk, which limits the luminescence collection to a 5 μm wide region to reduce the background noise. A 0.5m spectrometer with a liquid N_2 cooled CCD array and with a resolution of 70 μeV is utilized. Figure 5-7 shows two

typical PL spectra. Usually, there is a narrow WL peak at 850nm, a broad range of emissions around 860~885nm associated with WL fluctuations, and several sharp QD peaks between 890 nm and 940nm (the number of these sharp peaks statistically matches the QDs that we count using AFM). Images from the CCD monitoring camera typically indicate a pattern consisting of a bright ring and several spots. We have correlated these bright spots with discrete QD emission lines.

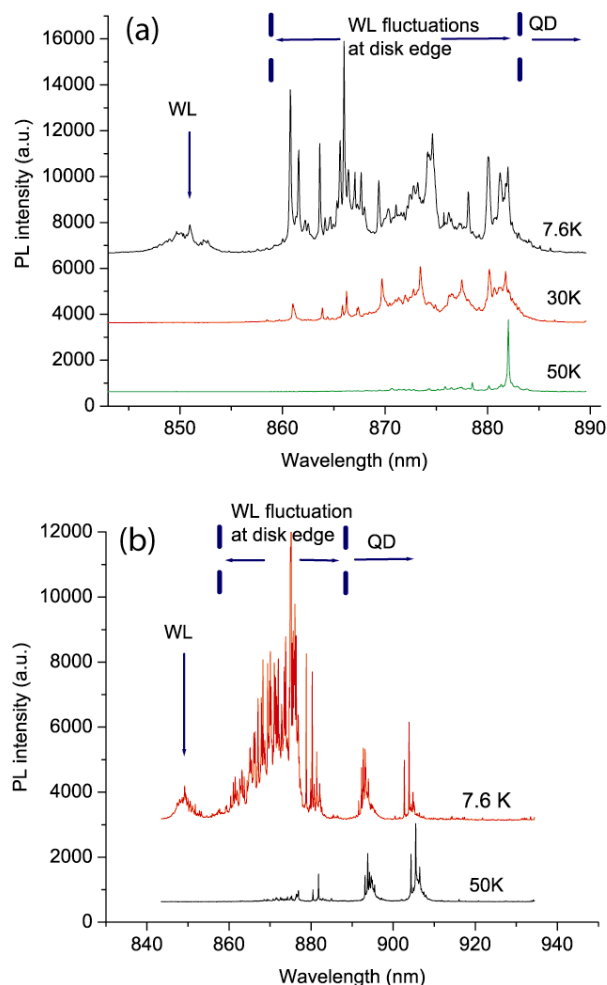


Figure 5-7. (a) 7K Micro-PL measurement from disk 1 (3 μm diameter). There are quasi-continuous states in the range of 860~885nm. With increasing temperature, emission is only at 882nm, possibly because all the carriers relax to the deepest confinement. (b) Micro-PL measurement from another disk, disk 2 (4 μm diameter). Besides the quasi-continuous states in the range of 860~885nm, there are also distinct QD peaks in the long wavelength side of 890 nm.

We have found that for small disks the majority of the luminescence at low temperature ($\sim 7\text{K}$) is from the ring-shaped pattern, located close to the edge. We use the aperture to correlate spectral and spatial position, and conclude that the ring-shaped emission is dominated by emission in the spectrum region we associate with wetting layer fluctuations and is localized in the vicinity of the edge. With increasing sample temperature, the PL emission in the 860~885nm range disappears leaving only QD emission (in the 890~940nm range), indicating the confinement in these WL fluctuations is weak. When the sample temperature is increased, trapped carriers evaporate from local energy minima into the global energy minimum (Figure 5-7a and disk 1 with a diameter of 4 μm) of the WL fluctuations or into the 3D QDs (Figure 5-7b and disk 2 with the same size).

Figure 5-8 shows a typical PL measurement of a 3 μm diameter disk sample (disk 3) and photoluminescence excitation (PLE) for the $\sim 890\text{nm}$ QD emission line. The PLE intensity drops nearly an order of magnitude while scanning the pumping wavelength above 850nm, but nevertheless persists. Since we observe $\sim 890\text{nm}$ QD emission from pumping into a continuous distribution of states until a soft cutoff at 872nm, we estimate the energy separation between QD ground states and these nearby WL fluctuations using the cutoff edge to be about 26 meV in this sample. The persistence of PL excitation before the cutoff is related to the carrier transfer from WL fluctuations states to the QD states. On $\sim 50\%$ of our samples we see an additional resonance very close to the PLE cutoff. We associate this resonance with QD excited states. This can have an important role in carrier diffusion to QDs and we discuss this further in a later section.

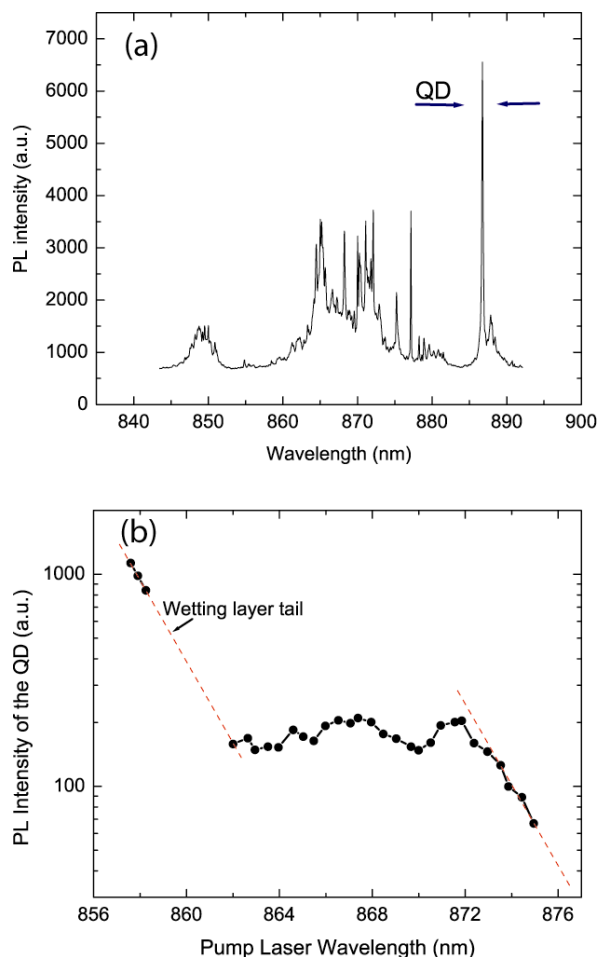


Figure 5-8. (a) Micro-PL measurement from the disk 3 (4 μ m diameter). Very similar to the disk 2, there is a QD peak at 887 nm. (b) PLE measurement with detection of the 897nm QD peak. The wavelength of the pump laser is tuned from 857 nm to 875 nm. The results show there are quasi-continuous states spatially close to the QD state. The sharp drop of the QD PL intensity at 850~860 nm is observed as the pump wavelength scans cross the wetting layer into the WL fluctuation region. When the pump passes 872 nm, there are no longer quasi-continuous states, accounting for the second drop of PL intensity.

We make lifetime measurement on disk 4 with a diameter of 3 μ m and a QD exciton emission line centered at 917 nm. Figure 5-9a shows a low-resolution spectrum and Figure 5-9b shows a high-resolution spectrum. A streak camera with a resolution of 30 ps is used in our measurement. This disk sample was chosen because it has a large energy separation between the WL fluctuations and QD ground state. For above band pumping, we usually observe a single exciton emission peak, while for pumping in the 860~886nm range we typically see two additional side peaks in the low pumping power region (much lower than the exciton saturation power), noted as peak a2 and a3 in Figure 5-9b. The

three-peaks signature is typically observed in our sample. We related a₂ and a₃ to charged excitons (trions), though we have no clear evidence. The formation of trions is not related to unintentional doping, but quite possibly to WL fluctuations around the QD, where selective trapping of either electrons or holes could occur. However, for some special wavelength of above band pumping (750nm for example), we also observe the side peaks. For planar QD samples, we typically pump into the wetting layer close to 850nm obtaining shorter rising times compared to above-band pumping. But, as seen in Figure 5-9c, for our disk samples this strategy produces longer rising edges in the lifetime measurement compared to above-band pumping. This is related to the long diffusion path from the disk center to the edge where the QDs are located and the lower diffusivity associated with the rough WL. We therefore used above band pumping at 750nm that provides carriers with enough excess energy to reduce their diffusion time to QD ground states. In Figure 5-9c, an 860nm excitation, pumped into WL fluctuations, is also shown. We see a short rising edge, as in the above-band pumping, and different from pumping into the WL. This suggests that carriers generated in the WL fluctuations have a more direct path to QD states than those in the WL. This is consistent with our CCD measurement, showing WL fluctuation emission near the disk edge in the vicinity of the QD. Since these WL fluctuation states are only weakly confined (see Figure 5-7) we can approximate them as nearly 2D. A schematic energy diagram in the region around a QD is shown in Figure 5-9d.

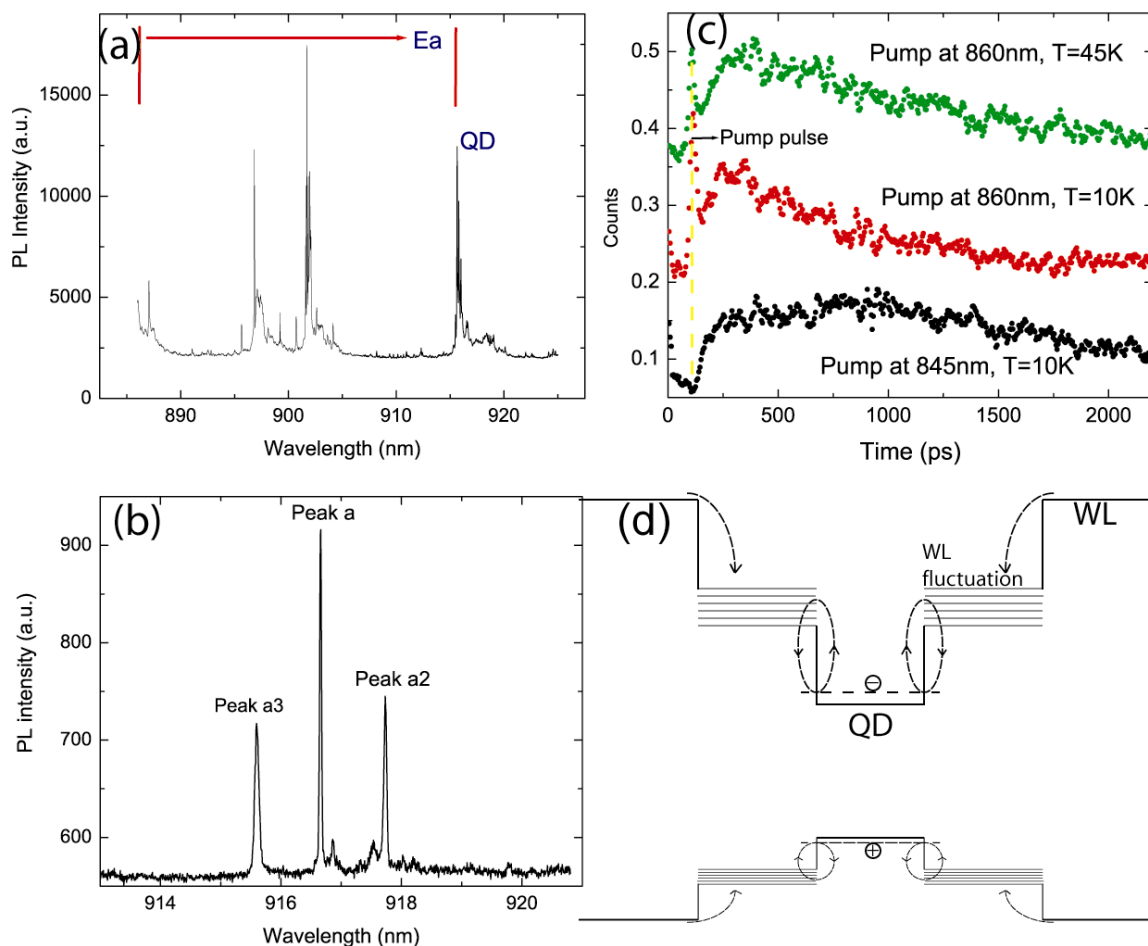


Figure 5-9. (a) The large wavelength scale PL spectrum for disk 4 ($3\mu\text{m}$ diameter). As with other samples, there is a broad quasi-continuous distribution of states between 860 nm and 885 nm, as well as several distinct QD peaks passing 890 nm. (b) A higher resolution scan for the QD peaks around 917 nm. Peak "a" is assumed to be the single exciton peak, and Peak "a2" and "a3" are assumed to be charged exciton peaks. (c) The SE decay curves under several combinations of pumping wavelength and sample temperature. The dash line on the left indicates the pump laser pulse. (d) A schematic band diagram of the global wetting layer, wetting layer fluctuations close to the edge, and the QD. The carriers repopulation between the QD and wetting layer fluctuations makes the observed mono-exponential exciton lifetime longer with increasing temperature.

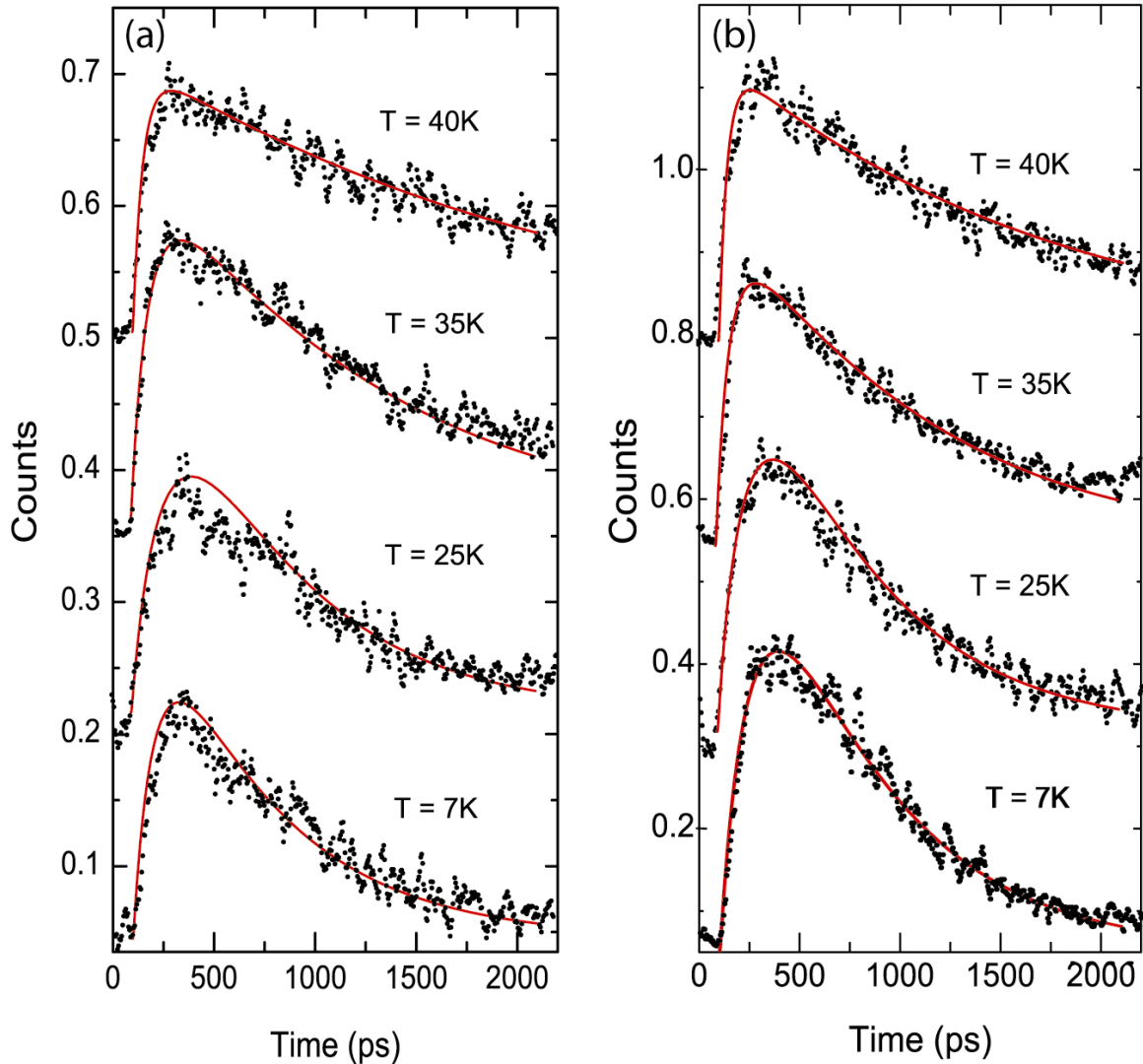


Figure 5-10. Comparison between the lifetime measurements and rate-equation simulations for disk 4. The "dots" are from experiment measurement and the "line" is from the simulation. (a) The exciton (peak a) SE emission decay curve. (b) The charged exciton (peak a2) decay curve.

We measured the single exciton lifetime, varying the sample temperature from 7K to 50K. The results are shown as in Figure 5-10 for the single exciton peak and one of the trion peaks. The temperature dependence of lifetime of the two states is shown in Figure 5-11. The rise times in Figure 5-9 are between 100~150 ps and remains approximately constant for the entire temperature tuning range (see also Figure 5-9c). For fixed pumping power, the time-integrated PL intensity of the single exciton peak increases with the temperature in the temperature range of 4K~30K and remains nearly constant in the range of 30~60K if the state is not saturated. We thus assume that up to 60K nonradiative

recombination is not significant. However, typically on our regrowth sample we see a mono-exponential decay with a lifetime that increases when the sample temperature is higher than 25~30K (Figure 5-11). There has been discussion of carriers evaporated from the QD states into the wetting layer at high temperature [105]. However, with an energy barrier of 95meV between the 850nm wetting layer and 917 nm QD ground states, it is quite unlikely (based on our modeling) that this effect involves the 850nm wetting layer states at a sample temperature of 30K. We propose the measured lifetime appears longer because of carrier recycling between QDs levels and a nearby reservoir. We believe this reservoir is composed of WL fluctuations at the edge. These WL fluctuations could be a dense, weakly confined distribution of 0D states. Below, a two level rate equation is used to explain the lifetime elongation.

In the model, we assumed that carriers created in the bulk GaAs or wetting layer region relax quickly through scattering into the QD. Carriers in the QD are assumed to be captured with a rate of c and lost at a rate of $r + e$. Here, r denotes the radiative recombination rate and e is the emission rate from the QD ground state into the reservoir states. As discussed above, the integrated intensity does not decrease in the 4~60K range and thus we can ignore the nonradiative recombination. From the PLE measurement, we can approximate the reservoir states around the QD as 2D states and the effective density of states (DOS) is $N_{WL} = (m_{WL} / \pi \hbar^2) k_B T$, where m_{WL} is the DOS effective mass of the carriers and taken to be $0.4 m_0$ [105] [106] for our materials, and T is the sample temperature. The occupation probability of the reservoir states and the QD are respectively $f_{WL}(t)$ and $f_Q(t)$, and are determined by the following coupling rate equations,

$$\begin{aligned} \frac{df_{WL}(t)}{dt} &= -c \cdot f_{WL}(t) \cdot (1 - f_Q(t)) + c \cdot \beta(E) \cdot f_Q(t) + g(t) \\ \frac{df_Q(t)}{dt} &= c \cdot N_{WL} A \cdot f_{WL}(t) \cdot (1 - f_Q(t)) - (r + e) \cdot f_Q(t) \end{aligned} \quad (5.4)$$

Here $f_{WL} \ll 1$ and $0 < f_Q < 1$, and $g(t)$ is the pumping and is given by a lorentzian form with a pulse width of 5ps based on our laser pulse width. A is the effective reservoir area surrounding each QD. In the above equations the emission (to the reservoir) and recapture rate coefficient are related by the detail balance requirement:

$$\frac{e}{c} = N_{WL} A \cdot \beta(E)$$

$$\beta(E) = \exp(-E_a / \nu k_B T) \quad (5.5)$$

We estimate A by comparing the QD ground state saturation power at the WL pumping wavelength (absorbing through the whole disk area) and the saturation power pumping at the WL fluctuations directly coupled to the QD, and estimate the value to be $\sim 0.20 \mu\text{m}^2$. We make the estimation based on high temperature (40~50K) PL data since at high temperature the only dominant emission is from the QD. However we note that this method assumes that WL fluctuations and wetting layer has similar absorption coefficients, and could over estimates the value. This value is verified later, where we fit A . The energy barrier E_a can also be estimated from PLE on the investigated QD. The parameter ν could be 1 if the capture and emission to the reservoir occur in the form of excitons, and 2 if they occur in the form of electrons and holes but average in pairs [106].

With these assumptions we can compare the experimentally measured excitons population decay with our rate equation simulation. We do this for both single exciton and one of the charged excitons. The reason is that charged excitons, especially negatively charged excitons are quite common for regrowth QDs and they have should have close thermal evaporation behavior if they origin from the same QD. Noticing that the rate equations are nonlinear in the high pumping power regime ($f \sim I$), we insure all the pumping powers are below 20% of the saturation power at each temperature point. In this case, the experimental results are independent of the pumping power.

In Figure 5-11, the change in the time dependent intensity as a function of sample temperature is shown for the single exciton and one of the charged excitons. This measurement was made on disk 4, shown in Figure 5-9. From the PLE measurement, we find an activation barrier E_a of about 45.3 meV for the single excitation (peak a) and 47 meV for the charged exciton (peak a2), with an assumption that electrons and holes are emitted to the reservoir not as excitons but average in pairs ($\nu=2$). If $c \gg r$ in Eqn. (5.4) and the pumping power is much smaller than saturation power for the QD, we get a nominal lifetime varying with the temperature:

$$\tau' = \tau \cdot (1 + N_{WL} \cdot A \cdot \beta) , \quad (5.6)$$

where τ is the intrinsic lifetime and τ' is the measured lifetime.

Using this model, we fit the lifetime data (Fig. 5-11) and get a value of $\tau = 599 \pm 34 \text{ ps}$, $A = 0.11 \pm 0.02 \mu\text{m}^2$ for the exciton and $\tau = 583 \pm 36 \text{ ps}$, $A = 0.19 \pm 0.03 \mu\text{m}^2$ for the charged exciton. There is a ratio of 2 between the values of the effective area A , which could come from the fact that for trions the final states are spin-dependent (spin up electron (hole) or spin down electron (hole) left in the QD) after the evaporation of the e-h pair. We noticed that these values qualitatively match the value for A estimated from intensities in our PLE experiments. If we have chosen $\nu = 1$ above, then A would be 1 or 2 orders higher from our original estimate.

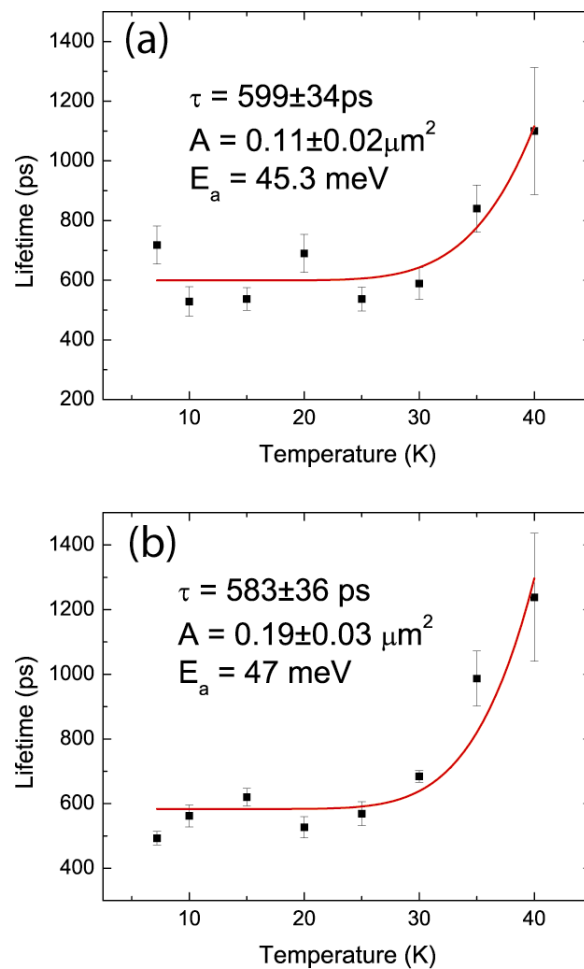


Figure 5-11. The fitted SE lifetime measurement results change with the temperature for disk 4. (a) The exciton. (b) One of the charged exciton (peak "a2").

Another possible explanation of the lifetime elongation with increased temperature is that carriers originally escaped from the shallow WL fluctuation states into the wetting layer states and are finally captured by the QDs. In this view, all the WL fluctuations and QDs are sitting directly on the global wetting layer and indirectly (through the global WL) coupled with each other. However, our simulations show this process will increase the rise time with increasing temperature, and does not match our experiment results. Another possibility is that there are excited states or optical phonon states between the QD ground states and the 850nm wetting layer. However, if the reservoir states are in fact excited QD states, the available reservoir states will be very limited for thermal emission to be prominent at a 30K. Also, the optical phonon states cannot be the reservoir since the radiative recombination channel remains significant in temperature regime questioned. Furthermore, optical phonon scattering typically shortens the lifetime of QD exciton states, and this is not observed.

The presence of non-radiative sites around the edge created during processing or regrowth must also be considered. From the simulation and experiment, if the reservoir is a temporary trapping center, for constant pump power and below saturation, the exciton PL intensity would not decrease at all temperatures. However, if the carriers in the trap level recombine via a non-radiative channel, the exciton PL will decrease with the increasing temperature. At a temperature up to 60K, we have not seen any decreasing of PL intensity. Instead, we see an increasing of QD PL intensity instead from 4K to 30K due to the reduced possibility of radiative recombination in the WL fluctuations region. Furthermore, the existence of a non-radiative channel will shorten the exciton lifetime, again not observed. Thus, we must exclude non-radiative recombination for our simulation.

We have investigated the ground state QD lifetime temperature stability for isolated QDs regrown on patterned surfaces. These QDs are located in the vicinity of a lithographically defined disk edge. Our time-resolved PL measurement indicates that carriers emission and recycling from the QD ground state to surrounding reservoir states make the measured mono-exponential lifetime longer with increasing temperature. We suggest that the surrounding states are WL fluctuation states close to the QD. The prominence of WL fluctuations around the edge makes the patterned QD environment

quite different from that on a planar surface. The interaction between the QD states and the WL fluctuation states makes the QD states less resilient to thermal evaporation. Because the WL fluctuation states are weakly bound at higher temperature, carriers relax back to the QD ground state and eventually recombine. The presence and prominence of WL fluctuations whose states couple to QD states provides new insights into the formation of QDs around the lithographic edge.

5.4. Whispering Gallery Modes in the regrowth cavity

This section will discuss the cavity modes in the microdisk cavities by regrowth and possible cavity effects in the regrowth sample. Different with the sample discussed in the previous section, the sample discussed here has enough undercut to ensure medium-high-Q. The SEM images below show the top view and side view for a 5 μm disk. The chemical cleaning before loading makes sure the top surface is perfectly clean and ready for epitaxial growth, while the bottom surface is purposely made imperfect by leaving partial AlGaAs layer untouched. The side view shows the sidewall is tilted due to the nature of MBE growth. Also we notice that crystal facet will show up as discussed in the previous section. Although the SEM images looks not as nice as the as-grown sample, the regrowth disk proves to have reasonable high-Q for cavity QED experiments.

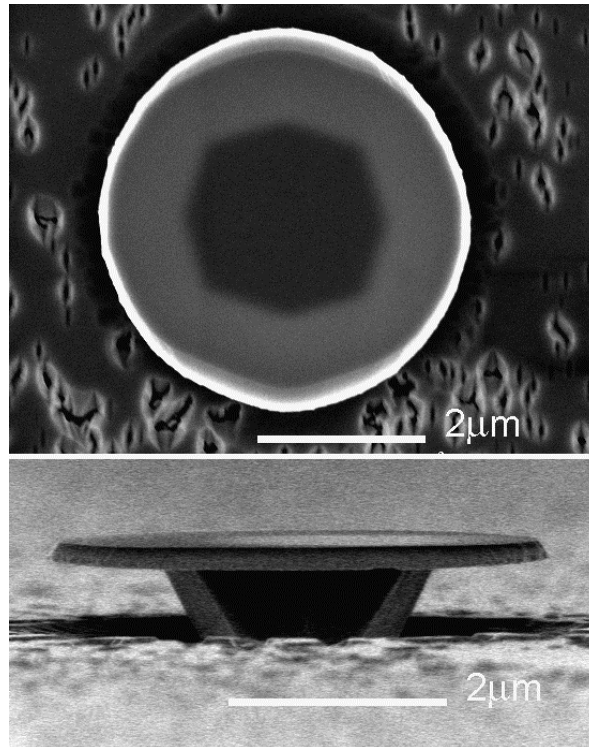


Figure 5-12. SEM images of 5 μm disk by regrowth. The top view shows the atomic flat surface and the side view shows the tilted edge due to the nature of MBE growth.

Again, this part of measure is done at Northwestern University, in Prof. H. Cao's group. In this part of measurement, contrast to the measurement for as-grown sample, the laser spot should be focused only on top of the disk to reduce possible emissions from the bottom surface. Therefore, the confocal setup, with collection and pumping through the same objective lens, is necessary for this step of optical measurement. To measure the PL from a 4 μm , the laser spot should be reduced to 2 μm , also the mechanic stability should be good. We randomly select one column of disks with sizes from 17 μm to 4 μm and test the cavity Q for each disk. The results are summarized in Figure 5-13. First of all, the yield for successful regrowth is high, all the disks in this size range at least have a medium high Q. The achievable cavity Q is 2,000~7,000. There is a trend that the Q will sharply reduce when the size shrinks, while it is almost constant for the range of 11~17 μm .

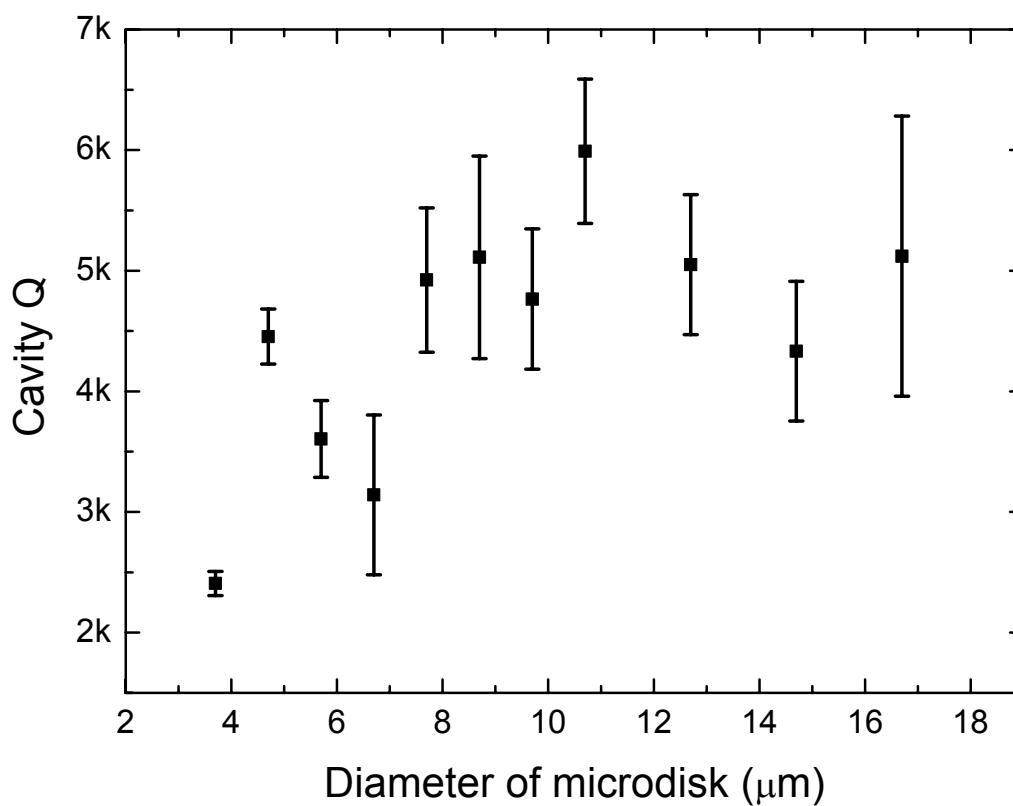


Figure 5-13. The cavity Q of different sizes of microdisk by regrowth in the same column.

Next, we carefully trace the linewidth of each modes changing with pumping and get the data of cavity Q in the low-pumping regime. Just as an example, we select the $5\mu\text{m}$ disk. In Figure 5-14, the left graph shows the mode distribution at a power of $130\mu\text{W}$ and we obtain a linewidth of 0.18nm and a FSR of $\sim 13\text{nm}$ close to a wavelength of 900nm . Our measurement shows in general it is impossible to achieve QDs lasing because of a very low density in this growth regime, however we always achieve lasing near wetting layer or wetting layer fluctuations. In Figure 5-14, the data shows lasing at a power of 10mW , with a linewidth narrowed below spectrum resolution.

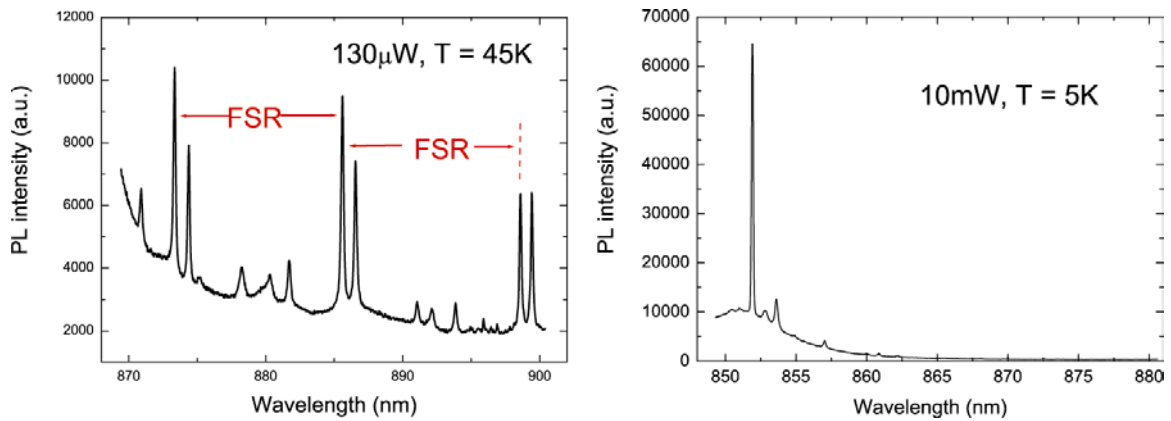


Figure 5-14. PL spectrum for a $5\mu\text{m}$ microdisk, the left graph shows the FSR for the mode distribution pattern and the right graph shows the lasing at wetting layer with a pumping power of 10mW.

For the cavity QED experiments, it is very important to realize tuning of the QD peaks through cavity modes. For this reason, we did temperature-tuning experiments for the cavity modes. In Figure 5-15, the left graph compares the PL taken at different temperature. It is easy to figure out the mode peak at a relatively high temperature, although the mode intensities are the same at different temperature. This is because the background is much flatter at high temperature. Similar with the mode shift reported in Chapter 3, there is a turning point around 30~35K and close to this point the mode shift stops. We believe, the abnormal shift close to the low temperature range 4K~30K should be related to the different thermal expansion coefficients between disk layer and the pedestal. However, the overall shift in the range of 5~55k is 0.9nm, smaller than the typical shift of QDs peak of 1.9nm.

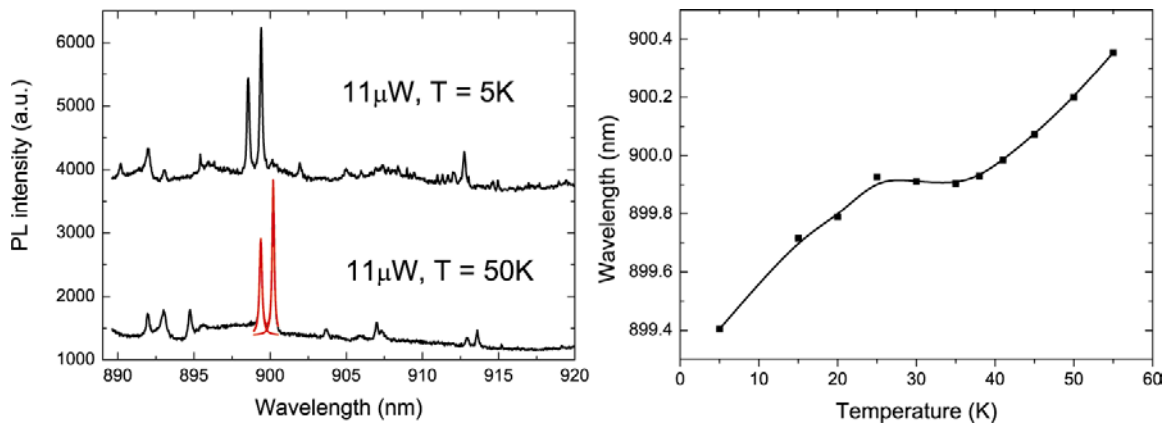


Figure 5-15. The temperature-tuning curve for the cavity mode peaks belonging to a $5\mu\text{m}$ microdisk.

Base on my measurements, all the active media including isolated QDs peaks will shift in almost the same way. They shift very slowly at low temperature 5~15K, and gradually faster with as the temperature increases. So in general, due to the abnormal shift of cavity mode peaks, we will expect at low temperature, the mode peaks will move faster than the QD peaks, while at high temperature, the trend is the opposite.

Same as the sample with shallow undercut, the disk sample now has a broad distribution at 860~890nm, and isolated QDs peaks at 890~920nm for small disks (4 μ m, 5 μ m and 6 μ m disks). We are only interested in the isolated QDs peaks and will focus on this regime. For the 5 μ m disk, the FSR is 13nm and for the 4 μ m disk, the FSR is 16nm with a wavelength close to 900nm. So, in principle, at least two fundamental TE modes will exist in the 890~920 nm regime. In fact, due to the complexity of regrowth, higher order modes or TM modes could also exist. In Figure 5-16, we show experimental results for a cavity mode tuning through QDs on a 4 μ m microdisk. The PL data are taken at a power of 0.5 μ W. The red curve shows the mode position filtered out at a higher power of 30 μ W. The QDs peaks are very broad, possibly due to degeneracy lifting. In principle, it is possible to reduce the broad peak into isolated fine peaks by adjusting the polarization and wavelength of pumping laser. However, in this experiment, above band bumping is utilized.

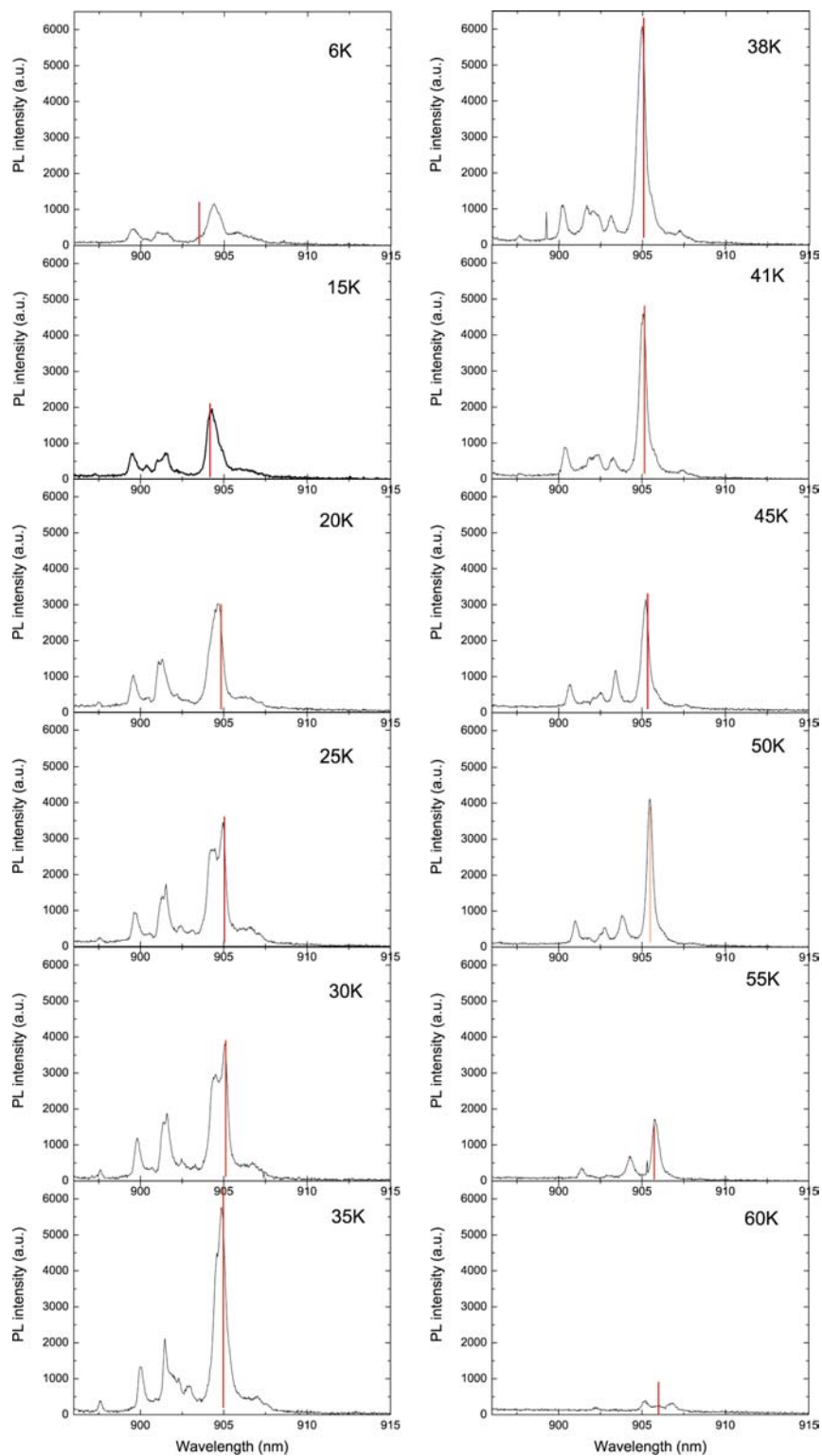


Figure 5-16. The experiments of QDs tuning through cavity modes. The red line is the cavity mode position determined at a high pump power.

Based on our measurement data, the mode intensity will not change too much with the temperature if not directly resonant with QDs. However, the QD intensity will depend on the temperature given the pumping power is constant and under saturation. The QDs intensity will sharply drop after a temperature of 60K. This is generally true both in as-grown QDs and regrowth QDs. According to the data, it is clear that the mode is chasing, then passing the QD peak in the range of 6K~30K. In the range of 30~50K, the QD peak is chasing the mode and they reach maximum overlap at 50K. However, the relative movement in the range of 38K~50K is rather smaller. It is not until after 50K, that the QD peak is completely above the mode peak. By comparing with the neighboring QD peaks, the QDs intensity increases by boosted 2~3 times when on resonance with the cavity mode. Due to the horizontal nature of microdisk emission, the actual enhancement should be much larger.

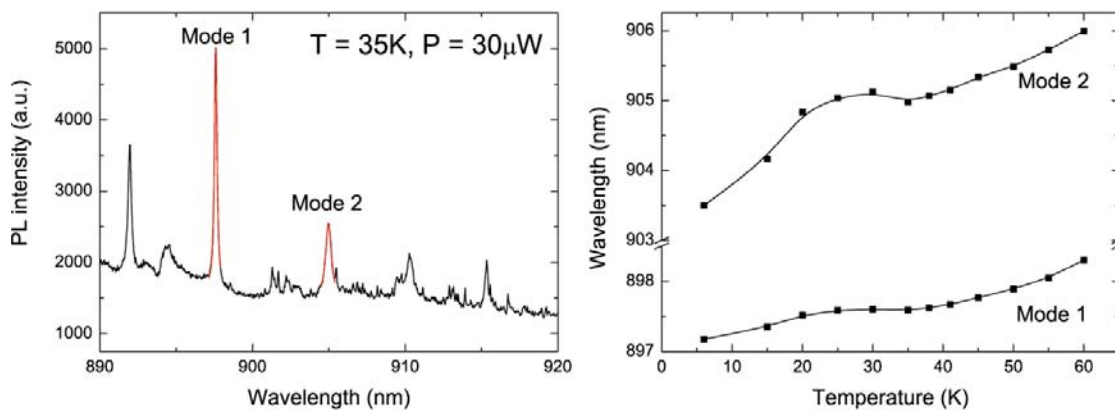


Figure 5-17. (left) the PL spectrum at a high power of 30 uW; (b) Two cavity modes shift with the temperature.

We put the PL data at higher power of 30 μW in Figure 5-17 and also the temperature tuning of the cavity modes in this 4 μm disk. However, the shift is quite different as the curve in Figure 5-15.

In the above discussion, only PL measurements are introduced. However, the direct and more convincing way is to do lifetime measurements. It should be possible to observe a lifetime shortening when the QD and cavity mode are on resonant. However,

this has not been done due to measurement setup. We still keep in mind that possible lifetime elongation will make this observation more difficult as discussed in previous section of this chapter.

Chapter 6. Future directions and conclusions

In this thesis, we introduce two coupling schemes of QDs with microdisk cavity. Microdisk made via wet etching get rid of the requirement of delicate ebeam tools. Compared with dry etching, this method will reduce the possibility of surface damage as non-radiative recombination sites. In general, the microdisk cavity will be an ideal high-Q cavity for cavity QED experiments except for the weakness of in-plane emission.

The first method uses traditional randomly grown self-assembled InAs QDs capped inside a GaAs layer. To make use of the advantage of Purcell effect and make better spatial coupling of QDs with the cavity modes, the disk size should be as small as possible. Here, the smallest $1.8\mu\text{m}$ disks are introduced. I discuss my methods for processing and growth, as well as the QDs PL and mode properties characterization. A high Q of 6,000~10,000 are reported in this thesis with a mode volume of $4\sim 5 (\lambda/n)^3$, a maximum Purcell effect of 80~150 can be achieved in theory if the spatial coupling and electric dipole alignment is ideal. Using this sample, we see a possibility of near individual QD lasing. The next step will be to further optimize the growth and processing to get strong coupling and single QD lasing in the same system.

The second approach is to use regrowth techniques to realize ideal spatial coupling. This scheme put high demands on the wafer cleaning, before the MBE regrowth to ensure high quality QDs. By exploring this technique, we find the regrowth QDs are quite similar to self-assembled QDs. For the same growth conditions, the emission wavelength is 890~920nm, the lifetime is 600~1000ps and the PL intensity remains high unless the sample temperature is above 60K. The only problem is the degeneracy lifting, which make a broad distribution under above-band pumping. However, this can be resolved by adjusting the pumping wavelength. The best result on our regrowth sample will be a cavity Q of 4,000~5,000 on our $5\mu\text{m}$ disk, with a mode volume of $13(\lambda/n)^3$. With this technique, we would expect a best Purcell effect of ~ 15 . In the final section of Chapter 5, a possible coupling experiment of QDs with microdisk is introduced, but only in the PL data. More convincing experiments will be lifetime measurements when the QD cross the cavity mode. However, this is left for the future.

Appendix A. Microdisk Processing recipe

1) Partial cavity growth:

In Gen II MBE system, with an Group V/III flux ratio of 15, a sample temperature of 600°C, three layers of structure including 300nm GaAs buffer layer, 600~700nm Al_{0.77}Ga_{0.23}As and 120nm GaAs top layer are sequentially grown on one inch GaAs(001) wafer. The growth rate of GaAs layer is around 0.2µm/hr, while the growth rate of AlGaAs layer is 0.6µm/hr.

2) Optical lithography:

The wafer is cleaved into 4 quarter-wafers with exact equal sizes ready for optical lithography. A quartz mask with a field size of 1 inch, from the commercial vender Compugraphics, is utilized in this step. The step is finished in CIS clean room.

- a) After standing solvent clean (acetone, methanol, isopropanol) in a small glass container.
- b) The wafer is baked at 110°C on a hot plate for 20 minutes.
- c) 1µm-thick photoresist of SPR3612 is coated on the quarter wafer using laurel coater. 3-step spinning process is used: pre-spin at 300 rpm, effective spin at 5500 rpm for 50secs, 300rpm finalize-spin for 20secs. The resist is manually applied just before the pre-spin ends for uniform coating.
- d) A pre-exposure bake of 90°C for 1mins is applied, followed by a cooling down process before the wafer is loaded into Karl-Suss contact aligner. The exposure time is 1 secs with 365nm and 15 mw/cm² UV lamp. The wafer is unloaded and post-baked at 115°C for 1~3 mins.
- e) The wafer is developed in LDD26W for 50secs. A little bit of over-exposure or over-develop is utilized, plus a hard bake of 135°C for half an hour to reflow the photoresist for best smoothness.

3) Chemical etching

This part of etching is finished at GaAs wet bench in CIS clean room. All the chemical solutions are stabilized for half an hour at room temperature, after the mixture, for best repeatability. For defining the circular pattern, an etching rate of 200nm/min is used, for example, with the recipe of $\text{H}_3\text{PO}_4:\text{H}_2\text{O}_2:\text{H}_2\text{O}=3:1:25$ for precise control and reduction of small drill between the photoresist and the GaAs top layer. No shake or swing is applied since the water flow will deviate the pattern from an exact circular shape.

For undercut of AlGaAs layer to define the pedestal of the microdisk, $\text{HCl}:\text{H}_2\text{O}=1:1$ or $1:3$, or buffered oxide etcher (BOE 6:1) is used. The etching rate is 200~500nm/min for $\text{Al}_{0.77}\text{Ga}_{0.23}\text{As}$. For $\text{Al}_{0.7}\text{Ga}_{0.3}\text{As}$, usually a heated solution, stabilized at 50°C is applied. Mechanic stirring of the solution is recommended for this step.

4) Photoresist strip

It is very critical to get rid of photoresist. Usually, standard solvent is enough to solve the photoresist with long enough time (>10mins for each solvent) and constant liquid flow, as far as the hard bake temperature (Step 2e) is not too high. Otherwise, Micropost® 1165 at 50°C is used to strip the photoresist. But this chemical is not compatible with regrowth process.

5) Chemical cleaning of pre-loading wafer

This step is only for regrowth. Before loading of processed wafer into the MBE chamber, it is critical to get the surface chemically clean. The sample needs to be transferred from one location to another, so multi-steps are required to chemically clean the surface. The pre-loading cleaning should be done close to the MBE loading chamber.

- a) Soaked in $\text{H}_2\text{O}_2:\text{H}_2\text{O}=1:10$ for 2mins. Rinsed in a huge amount of DI water.
- b) $\text{NH}_4\text{OH}:\text{H}_2\text{O}=1:50$ for 50secs.
- c) $\text{NH}_4\text{OH}:\text{H}_2\text{O}_2:\text{H}_2\text{O}=1:1:120$ for 12secs. Instantly taken out and rinsed in DI water.

Then blow dry with N_2 gun.

6) MBE regrowth

The sample is loaded instantly into a quarter-wafer-holder after the chemical clean is done. Before transferred to the growth chamber, the sample is baked at 400°C for 2hrs. In the growth chamber, the wafer is annealed at 630°C for 1hr. Then with a growth rate of 0.1 μ m/hr, As/Ga flux ratio of 20, As/In flux ratio of 30, 35 nm GaAs buffer layer, 1.8~2.0ML InAs layer, 80nm GaAs cap layer are sequentially grown. For the QDs growth, the sample is cooled to 500°C and stabilized for a while. For QDs imaging with AFM or SEM, InAs deposition is followed by 2secs waiting, and instantly temperature quenching.

Appendix B. 3D FDTD Calculation and Output Code

This part of calculation was done at tree1, tree2 or Junior. Stanford.edu.

% this code is for final project with 3D TE mode calculation

% and the sidewall of the disk is about 45 degree tilted and the undercut is 0.3um

% modified from udisk17m.m

% the unit of time is s, the unit of length is meter

epr=1/4/pi/9e9; %permittivity of free space

mur=pi*4e-7; %permeability in free space

vp=1/sqrt(epr*mur);

epr2=3.5.^2*epr; epr3=3.06.^2*epr;

sig2=0.0/epr2;

%modified...modified

neff=sqrt(epr2);

wavelength=900e-9; frequency=vp/wavelength;

delta_x=20e-9;delta_y=delta_x;delta_z=delta_x;

delta_t=delta_x/vp/sqrt(3);

diameter=1.8e-6;doub_a=diameter;doub_b=diameter;thick=0.2e-6;

undercut=0.2e-6;diameter2=diameter-undercut*2;pedal_H=0.4e-6;

x_grid=round(doub_a/delta_x+40);y_grid=round(doub_b/delta_y)+40;z_grid=round(thic
k/delta_z)+40;

t_grid=100000;

t_span=t_grid*delta_t;

error=1e-9;

%to define the coefficient of PMC

```

m=4;
sigx_max=0.8*(m+1)*vp/delta_x;sigy_max=sigx_max;sigz_max=sigx_max;
sigx1_max=sigx_max;sigy1_max=sigy_max;sigz1_max=sigz_max;
nx=10;ny=10;nz=10; %the layer number of PMC

%this is used to determine the initial condition
ie=x_grid+2*nx;je=y_grid+2*ny;ke=z_grid+2*nz;
i_A=round(ie/2-diameter/2/delta_x+6); j_A=round(je/2+1);k_A=round(ke/2+1);
i_B=round(ie/2+diameter/2/delta_x-6); j_B=j_A; k_B=k_A;

for i=1:(ie+1)
    if i<=nx sigx(i)=sigx_max*(1-(i-1)/nx).^4;
    elseif i>=(x_grid+nx+1) sigx(i)=sigx_max*((i-x_grid-nx-1)/nx).^4;
    else sigx(i)=0;
    end
end
for j=1:(je+1)
    if j<=ny sigy(j)=sigy_max*(1-(j-1)/ny).^4;
    elseif j>=(y_grid+ny+1) sigy(j)=sigy_max*((j-y_grid-ny-1)/ny).^4;
    else sigy(j)=0;
    end
end
for k=1:(ke+1)
    if k<=nz sigz(k)=sigz_max*(1-(k-1)/nz).^4;
    elseif k>=(z_grid+nz+1) sigz(k)=sigz_max*((k-z_grid-nz-1)/nz).^4;
    else sigz(k)=0;
    end
end

for i=1:(ie)

```

```

if i<=nx sigx1(i)=sigx1_max*(1-(i-1/2)/nx).^4;
elseif i>=(x_grid+nx+1) sigx1(i)=sigx1_max*((i-x_grid-nx-1/2)/nx).^4;
else sigx1(i)=0;
end
end
dyx1(1:ie)=(2-delta_t*sigx1(1:ie))./(2+delta_t*sigx1(1:ie));
dyx2(1:ie)=2*delta_t./(2+delta_t*sigx1(1:ie))/delta_x/mur;
dzx1(1:ie)=(2-delta_t*sigx1(1:ie))./(2+delta_t*sigx1(1:ie));
dzx2(1:ie)=2*delta_t./(2+delta_t*sigx1(1:ie))/delta_x/mur;

for j=1:(je)
if j<=ny sigy1(j)=sigy1_max*(1-(j-1/2)/ny).^4;
elseif j>=(y_grid+ny+1) sigy1(j)=sigy1_max*((j-y_grid-ny-1/2)/ny).^4;
else sigy1(j)=0;
end
end
dxy1(1:je)=(2-delta_t*sigy1(1:je))./(2+delta_t*sigy1(1:je));
dxy2(1:je)=2*delta_t./(2+delta_t*sigy1(1:je))/delta_y/mur;
dzy1(1:je)=(2-delta_t*sigy1(1:je))./(2+delta_t*sigy1(1:je));
dzy2(1:je)=2*delta_t./(2+delta_t*sigy1(1:je))/delta_y/mur;

for k=1:(ke)
if k<=nz sigz1(k)=sigz1_max*(1-(k-1/2)/nz).^4;
elseif k>=(z_grid+nz+1) sigz1(k)=sigz1_max*((k-z_grid-nz-1/2)/nz).^4;
else sigz1(k)=0;
end
end
dxz1(1:ke)=(2-delta_t*sigz1(1:ke))./(2+delta_t*sigz1(1:ke));
dxz2(1:ke)=2*delta_t./(2+delta_t*sigz1(1:ke))/delta_z/mur;
dyz1(1:ke)=(2-delta_t*sigz1(1:ke))./(2+delta_t*sigz1(1:ke));
dyz2(1:ke)=2*delta_t./(2+delta_t*sigz1(1:ke))/delta_z/mur;

```

2

```

for i=1:(ie)
    %modified
    for j=1:(je)
        %modified
        for k=1:(ke)
            %modified
            x(i)=(i-ie/2-1/2)*delta_x;y(j)=(j-je/2-1/2)*delta_y;z(k)=(k-ke/2-1/2)*delta_z;
            %modified
            a=x(i).^2+y(j).^2-(diameter/2-z(k)*1).^2; %modified
            b=x(i).^2+y(j).^2-(diameter/2).^2;
            if (a<=0)&(z(k)>=-thick/2)&(z(k)<=thick/2)
                %modified
                epr_xyz(i,j,k)=epr2;
            elseif (b<=0)&(z(k)>=-pedal_H-thick/2)&(z(k)<=-thick/2)
                epr_xyz(i,j,k)=epr3;

            %modified
        else
            %modified
            epr_xyz(i,j,k)=epr;

            %modified
        end

        %modified
    end

    %modified
end
end
end

```

```

for i=1:ie
  for j=1:(je+1)
    for k=1:(ke+1)
      if (j>ny)&(j<(je-ny))&(k>nz)&(k<(ke-nz))
                                                                 %modified
          epr_avg=(epr_xyz(i,j,k)+epr_xyz(i,j-1,k)+epr_xyz(i,j,k-1)+epr_xyz(i,j-1,k-1))/4;
          %error found vs udisk3DTE8.m
      else
                                                                 %modified
          epr_avg=epr;
                                                                 %modified
      end
                                                                 %modified
                                                                 %modified...modified
      cxy1(j)=(2-delta_t*(sigy(j)))/(2+delta_t*(sigy(j)));
      cxy2(i,j,k)=2*delta_t/(2+delta_t*(sigy(j)))/delta_y/(epr_avg);
      cxz1(k)=(2-delta_t*(sigz(k)))/(2+delta_t*(sigz(k)));
      cxz2(i,j,k)=2*delta_t/(2+delta_t*(sigz(k)))/delta_z/(epr_avg);
    end
  end
end
3
for i=1:(ie+1)
  for j=1:(je)
    for k=1:(ke+1)

```

```

if (i>nx)&(i<(ie-nx))&(k>nz)&(k<(ke-nz))
                                                    %modified...
    epr_avg=(epr_xyz(i,j,k)+epr_xyz(i-1,j,k)+epr_xyz(i,j,k-1)+epr_xyz(i-1,j,k-1))/4;
%error found
else
    epr_avg=epr;
end

                                                    %...modified

                                                    %modified...modified
cyx1(i)=(2-delta_t*(sigx(i)))/(2+delta_t*(sigx(i)));
cyx2(i,j,k)=2*delta_t/(2+delta_t*(sigx(i)))/delta_x/(epr_avg);
cyz1(k)=(2-delta_t*(sigz(k)))/(2+delta_t*(sigz(k)));
cyz2(i,j,k)=2*delta_t/(2+delta_t*(sigz(k)))/delta_z/(epr_avg);

end
end
end
4
for i=1:(ie+1)
    for j=1:(je+1)
        for k=1:(ke)
            if (i>nx)&(i<(ie-nx))&(j>ny)&(j<(je-ny))
                                                    %modified...
                epr_avg=(epr_xyz(i,j,k)+epr_xyz(i-1,j,k)+epr_xyz(i,j-1,k)+epr_xyz(i-1,j-1,k))/4;
%error found
            else
                epr_avg=epr;
            end
        end
    end
end

```

```
end
```

```
    %...modified
```

```
        %modified...modified
```

```
        czx1(i)=(2-delta_t*(sigx(i)))/(2+delta_t*(sigx(i)));
```

```
        czx2(i,j,k)=2*delta_t/(2+delta_t*(sigx(i)))/delta_x/(epr_avg);
```

```
        czy1(j)=(2-delta_t*(sigy(j)))/(2+delta_t*(sigy(j)));
```

```
        czy2(i,j,k)=2*delta_t/(2+delta_t*(sigy(j)))/delta_y/(epr_avg);
```

```
    end
```

```
end
```

```
end
```

```
5
```

```
clear epr_xyz;
```

```
Hzx(1:ie,1:je,1:ke+1)=0; Hzy(1:ie,1:je,1:ke+1)=0;
```

```
Hx(1:ie,1:je,1:ke+1)=Hzx(1:ie,1:je,1:ke+1)+Hzy(1:ie,1:je,1:ke+1);
```

```
Hxy(1:ie+1,1:je,1:ke)=0; Hxz(1:ie+1,1:je,1:ke)=0;
```

```
Hx(1:ie+1,1:je,1:ke)=Hxy(1:ie+1,1:je,1:ke)+Hxz(1:ie+1,1:je,1:ke);
```

```
Hyx(1:ie,1:je+1,1:ke)=0; Hyz(1:ie,1:je+1,1:ke)=0;
```

```
Hy(1:ie,1:je+1,1:ke)=Hyx(1:ie,1:je+1,1:ke)+Hyz(1:ie,1:je+1,1:ke);
```

```
Ezx(1:ie+1,1:je+1,1:ke)=0; Ezy(1:ie+1,1:je+1,1:ke)=0;
```

```
Ez(1:ie+1,1:je+1,1:ke)=Ezx(1:ie+1,1:je+1,1:ke)+Ezy(1:ie+1,1:je+1,1:ke);
```

```
Exy(1:ie,1:je+1,1:ke+1)=0; Exz(1:ie,1:je+1,1:ke+1)=0;
```

```
Ex(1:ie,1:je+1,1:ke+1)=Exy(1:ie,1:je+1,1:ke+1)+Exz(1:ie,1:je+1,1:ke+1);
```

```
Eyx(1:ie+1,1:je,1:ke+1)=0; Eyz(1:ie+1,1:je,1:ke+1)=0;
```

```
Ey(1:ie+1,1:je,1:ke+1)=Eyx(1:ie+1,1:je,1:ke+1)+Eyz(1:ie+1,1:je,1:ke+1);
```

```

1
%initial condition is determined
for n=1:t_grid
    t(n)=n*delta_t;

    %this part is used to calculate the scatter field value of Ey, Hx,Hz
    for j=2:je
        Exy(1:ie,j,2:ke)=cxy1(j)*Exy(1:ie,j,2:ke)+...
            cxy2(1:ie,j,2:ke).*(Hz(1:ie,j,2:ke)-Hz(1:ie,j-1,2:ke));
    end

    for k=2:ke
        Exz(1:ie,2:je,k)=cxz1(k)*Exz(1:ie,2:je,k)-...
            cxz2(1:ie,2:je,k).*(Hy(1:ie,2:je,k)-Hy(1:ie,2:je,k-1));
    end

    for i=2:ie
        Eyx(i,1:je,2:ke)=cyx1(i)*Eyx(i,1:je,2:ke)-...
            cyx2(i,1:je,2:ke).*(Hz(i,1:je,2:ke)-Hz(i-1,1:je,2:ke));
    end

    for k=2:ke
        Eyz(2:ie,1:je,k)=cyz1(k)*Eyz(2:ie,1:je,k)+...
            cyz2(2:ie,1:je,k).*(Hx(2:ie,1:je,k)-Hx(2:ie,1:je,k-1));
    end

    for i=2:ie
        Ezx(i,2:je,1:ke)=czx1(i)*Ezx(i,2:je,1:ke)+...
            czx2(i,2:je,1:ke).*(Hy(i,2:je,1:ke)-Hy(i-1,2:je,1:ke));
    end
end

```

```

for j=2:je
    Ezy(2:ie,j,1:ke)=czy1(j)*Ezy(2:ie,j,1:ke)-...
        czy2(2:ie,j,1:ke).*(Hx(2:ie,j,1:ke)-Hx(2:ie,j-1,1:ke));
end

    Ez(2:ie,2:je,1:ke)=Ezx(2:ie,2:je,1:ke)+Ezy(2:ie,2:je,1:ke);
    Ex(1:ie,2:je,2:ke)=Exy(1:ie,2:je,2:ke)+Exz(1:ie,2:je,2:ke);
Ey(2:ie,1:je,2:ke)=Eyx(2:ie,1:je,2:ke)+Eyz(2:ie,1:je,2:ke);

    %modified...modified

    for j=1:je
        Hxy(1:ie+1,j,1:ke)=dxy1(j)*Hxy(1:ie+1,j,1:ke)-...
            dxy2(j)*(Ez(1:ie+1,j+1,1:ke)-Ez(1:ie+1,j,1:ke));
    end

for k=1:ke
    Hxz(1:ie+1,1:je,k)=dxz1(k)*Hxz(1:ie+1,1:je,k)+...
        dxz2(k)*(Ey(1:ie+1,1:je,k+1)-Ey(1:ie+1,1:je,k));
end

for i=1:ie
    Hyx(i,1:je+1,1:ke)=dyx1(i)*Hyx(i,1:je+1,1:ke)+...
        dyx2(i)*(Ez(i+1,1:je+1,1:ke)-Ez(i,1:je+1,1:ke));
end

for k=1:ke
    Hyz(1:ie,1:je+1,k)=dyz1(k)*Hyz(1:ie,1:je+1,k)-...
        dyz2(k)*(Ex(1:ie,1:je+1,k+1)-Ex(1:ie,1:je+1,k));
end

```

```

for i=1:ie
    Hzx(i,1:je,1:ke+1)=dzx1(i)*Hxz(i,1:je,1:ke+1)-...
        dzx2(i)*(Ey(i+1,1:je,1:ke+1)-Ey(i,1:je,1:ke+1));
end

for j=1:je
    Hzy(1:ie,j,1:ke+1)=dzy1(j)*Hzy(1:ie,j,1:ke+1)+...
        dzy2(j)*(Ex(1:ie,j+1,1:ke+1)-Ex(1:ie,j,1:ke+1));
end

    Hz(1:ie,1:je,1:ke+1)=Hxz(1:ie,1:je,1:ke+1)+Hzy(1:ie,1:je,1:ke+1);
    Hx(1:ie+1,1:je,1:ke)=Hxy(1:ie+1,1:je,1:ke)+Hxz(1:ie+1,1:je,1:ke);
    Hy(1:ie,1:je+1,1:ke)=Hyx(1:ie,1:je+1,1:ke)+Hyz(1:ie,1:je+1,1:ke);
if n<=300 Hz(i_A,j_A,k_A)=exp(-(n/50-3).^2)*sin(2*pi*(frequency)*t(n));
else
end
%Hz(i_A,j_A)=sin(2*pi*(3.07591e14)*t(n));
Hz_A(n)=Hz(i_A,j_A,k_A);Hz_B(n)=Hz(i_B,j_B,k_B);
%calculation of the scatter field of Ey, Hx, Hz finished.
    n

end

%subplot(3,1,1);pcolor(Hz((nx+1):(x_grid+nx),(ny+1):(y_grid+ny),ke/2+1));
%shading flat;
%colorbar;
%axis image;
%title(['Hz at time = ']);
%Y=abs(fft(Hz_A));

```

```
%N = length(Hz_A);
%Amp=Y(1:N/2);
%nyquist = 1/2/delta_t;
%freq = (0:(N/2-1))/(N/2)*nyquist;
%subplot(3,1,2);plot(freq,Amp);title(['FFT of original pulse']);
%Y=abs(fft(Hz_B));
%N = length(Hz_B);
%Amp=Y(1:N/2);
%nyquist = 1/2/delta_t;
%freq = (0:(N/2-1))/(N/2)*nyquist;
%subplot(3,1,3);plot(freq,Amp);title(['FFT of received pulse']);

%y=[freq(1:2500);Amp(1:2500)];
%fid=fopen('udisk22m.txt','w');
%fprintf(fid,'%12.8f %12.8f\r',y);
%fclose(fid);

save udisk22m Hz Ez Ex Hz_A Hz_B;
unix('elm -s finished zxie < udisk22m.out');
```

Bibliography

- [1] E. M. Purcell, Phys. Rev. **69**, 681 (1946).
- [2] G. S. Solomon, M. Pelton, and Y. Yamamoto, Phys. Rev. Lett. **86**, 3903 (2001).
- [3] C. Santori, D. Fattal, J. Vuckovic, G. S. Solomon, and Y. Yamamoto, Nature (London) **419**, 594 (2002).
- [4] E. Waks, K. Inoue, C. Santori, D. Fattal, J. Vuckovic, G. S. Solomon, and Y. Yamamoto, Nature (London) **420**, 762 (2002).
- [5] Jean-Michel Gerard and Bruno Gayral, Journal of Lightwave Technology **17**, 2089 (1999).
- [6] M Pelton, C. Santori, J. Vuckovic, BY Zhang, G. S. Solomon, J. Plant, and Y. Yamamoto, Phys. Rev. Lett. **89**, 233602 (2002).
- [7] Gunnar Bjork, Anders Karlsson, and Yoshihisa Yamamoto, Phys. Rev. A **50**, 1675 (1994).
- [8] Hui Deng, G. Weihs, C. Santori, J. Bloch, and Y. Yamamoto, Science **298**, 199 (2002).
- [9] J. P. Reithmaier, G. Sek, A. Loffler, C. Hofmann, S. Kuhn, S. Reitzenstein, L. V. Keldysh, V. D. Kulakovskii, T. L. Reinecke, and A. Forchel, Nature **432**, 197 (2004).
- [10] E. Peter, P. Senellart, D. Martrou, A. Lemaître and J. Bloch, unpublished.
- [11] T. Yoshie, A. Scherer, J. Hendrickson, G. Khitrova, H. M. Gibbs, G. Rupper, C. Ell, O. B. Shchekin, and D. G. Deppe, Nature **432**, 200 (2004).
- [12] Gunnar Bjork and Y. Yamamoto, IEEE Journal of Quantum Electronics, Vol 27, No. 11, Nov 1991, p2386.
- [13] Gunnar Bjork, Anders Karlsson, and Yoshihisa Yamamoto, Phys. Rev. A **50**, 1675 (1994).
- [14] G. Bjork, S. Machida, Y. Yamamoto, and K. Igeta, Phys. Rev. A **44**, 669 (1991).
- [15] A. M. Vredenberg, N.E.J. Hunt, E.F. Schubert, D.C. Jacobson, J.M. Poate, and G.J. Zyzdik, Phys. Rev. Lett. **71**, 517 (1993).

- [16] K. Tanaka, T. Nakamura, W. Takamatsu, M. Yamanishi, Y. Lee, and T. Ishihara, *Phys. Rev. Lett.* **74**, 3380 (1995).
- [17] L.A. Graham, D.L. Huffaker, Q. Deng, and D.G. Deppe, *Appl. Phys. Lett.* **72**, 1670 (1998).
- [18] T. Tezuka, S. Nunoue, H. Yoshida, and T. Noda, *Japan J. Appl. Phys.* **32**, no. L54 (1993).
- [19] J. M. Gerard, *Phys. Rev. Lett.* Vol 81, No. 5, 3 August 1998, p 1110.
- [20] Andrenani LC, *Phys. Rev. B*, Vol 60, No. 19, Nov 15 1999, p13276-13279.
- [21] Atsuo Nakagawa, Satoru Ishii, and Toshihiko Baba, *Appl. Phys. Lett.* **86**, 041112 (2005).
- [22] K. Oda, N. Takato, and H. Toba, *J. Lightwave Technology* **9**, 728-736 (1991).
- [23] S.C. Hagness, D. Rafizadeh, S.T. Ho, and A. Taflove, *J. Lightwave Technology* **15**, 2154-2165 (1997).
- [24] B.E. Little, J.-P. Laine, and S.T. Chu, *Optics Letter* **22**, 4-6 (1997).
- [25] R.E. Slusher, A.F.J. Levi, U. Mohideen, S.L. McCall, S.J. Pearton, and R.A. Logan, *Appl. Phys. Lett.* **63**, 1310-1312 (1993).
- [26] Ruo Peng Wang, *J. Appl. Phys.* 81(8), 15 April 1997, p3391-3397.
- [27] Mee Koy Chin, et al., *J. Appl. Phys.*, vol. 75, No. 7, 1 April 1994, p3302
- [28] B. Gayral, *Appl. Phys. Lett.* Vol 75, No. 13, 27 September 1999, p1908.
- [29] H. Cao et al, *Appl. Phys. Lett.*, Vol 76, No. 24, 12 June 2000, p3519.
- [30] S.L. McCall et al, *Appl. Phys. Lett.* Vol 60, No. 3, 20 Jan1992, p 289.
- [31] S.A. backers et al, *Journal of Vac. Sci. & Tech. B*, Vol 16, Issue 6, Nov 1998, pp. 3817-3820.
- [32] Chu et al, *Appl. Phys. Lett.* Vol. 65, No. 25, 19 Dec 1994, p 3168.
- [33] S. C. Hagness et al, *Journal of Lightwave Technology*, Vol. 15, No. 11, Nov 1997, p 2154.
- [34] Allen Taflove, Susan C. Hagness, *Computational Electrodynamics — the finite-difference time-domain method*, 2nd edition, p798.
- [35] K. Diordiev, *IEEE Photonics Technology Letters*, Vol. 14, No. 3, March 2002, p 331

-
- [36] K. Djordjev et al, IEEE Photonics Technology Letters, Voll 14, No.8, Aug 2002, p1115.
- [37] K. Djordjev et al, Appl. Phys. Lett. , Vol. 80, No. 19. 13 May 2002, p 3467.
- [38] K. Djordjev et al, Journal of Lightwave Technology, Vol. 20, No.1, Jan 2002, p105.
- [39] Allen Taflove, Susan C. Hagness, Computational Electrodynamics — the finite-difference time-domain method, 2nd edition. Page 294
- [40] Claire Gmachl et al, Kolmogorov Arnold Moser transition and laser action on scar modes in semiconductor diode lasers with deformed resonators, Optics Letters, Vol 27, Issue 10, 824-826, May 2002.
- [41] Atsuo Nakagawa, Satoru Ishii, and Toshihiko Baba, Appl. Phys. Lett. **86**, 041112 (2005).
- [42] P. Michael, A. Kiraz, Lidong Zhang, C. Becher, E. Hu, and A. Imamoglu, Appl. Phys. Lett. **77**, 184 (2000).
- [43] E. Peter, I. Sagnes, G. Guirleo, S. Varoutsis, J. Bloch, A. Lemaitre, and P. Senellart, Appl. Phys. Lett. **86**, 021103 (2005).
- [44] Haiping Yu, Sam Lycett, Christine Roberts, and Ray Murray, Appl. Phys. Lett. **69(26)**, 4087 (1996).
- [45] F. Ducroquet, P. Kropfeld, O. Yaradou, and A. Vanoverschelde, Journal of Vacuum Science and Technology B **16**, 787 (1998).
- [46] MG Kang, SH Sa, HH Park, KS Kuh, and KH Oh, Thin Solid Films **308**, 634 (1997).
- [47] M. M. Berdichenko, L. N. Vozmilova, and V. G. Malyarova, Inorganic Mterials **24**, 1028 (1988).
- [48] B. Tuck, JSK Mills, and A. J. Hartwill, Journal of Materials Science **11**, 847 (1976).
- [49] Y. Mori and N. Watanabe, Journal of the Electrochemical Society **124**, C104 (1977).
- [50] A. Ramam, S. Kapoor, S. Prabhakar, R. Gulati, and I. Chandra, Journal of the Electrochemical Society **136**, 2405 (1989).
- [51] Y. Mori and N. Watanabe, Journal of the Electrochemical Society **125**, 1510 (1978).
- [52] C. Zhang, D. Lubyshv, T.N. Jackson, D.L. Miller, and T.S. Mayer, Journal of the Electrochemical Society **146**, 1597 (1999).

-
- [53] Jong-Hee Kim, Dae Ho Lim, and Gye Mo Yang, *J. Vac. Sci. Technol. B* **16**, 558 (1998).
- [54] Zhi Liu, Yun Sun, F. Machuca, P. Pianetta, WE Spicer, and RFW Pease, *Journal of Vacuum Science & Technology A* **21(1)**, 212 (2003).
- [55] Zhi Liu, Yun Sun, F. Machuca, P. Pianetta, WE Spicer, and RFW Pease, *Journal of Vacuum Science & Technology B* **21(4)**, 1953 (2003).
- [56] P. Michler, A. Kiraz, C. Becher, W. V. Schoenfeld, P. M. Petroff, L. D. Zhang, E. Hu, and A. Imamoglu, *Science* **290**, 2282 (2000).
- [57] J. Tersoff, C. Teichert, and M. G. Lagally, *Phys. Rev. Lett.* **76**, 1675 (1996).
- [58] Y. Ebiko, S. Muto, D. Suzuki, S. Itoh, K. Shiramine, T. Haga, Y. Nakata, and N. Yokoyama, *Phys. Rev. Lett.* **80**, 2650 (1998).
- [59] J. Oshinowo, M. Nishioka, S. Ishida, and Y. Arakawa, *Appl. Phys. Lett.* **65**, 1421 (1994).
- [60] G. S. Solomon, J. A. Trezza, and A. F. Marshal, *Phys. Rev. Lett.* **76**, 952 (1996).
- [61] J. Robinson, O. Dubon, J. Alexliddle, and A. Minor, 27th International Conference on the Physics of Semiconductors, Flagstaff, Arizona, USA, (2004).
- [62] T. I. Kamins and R. Stanley Williams, *Appl. Phys. Lett.* **71**, 1201 (1997).
- [63] Z. G. Xie, G. S. Solomon, unpublished
- [64] S. Rufo, M. Dutta, and M. A. Stroschio, *J. Appl. Phys.* **93**, 2900 (2003).
- [65] P. G. Eliseev, H. Li, G. T. Liu, A. Stintz, T. C. Newell, L. E. Lester, and K. J. Malloy, *Quantum Electronics* **30**, 664 (2000).
- [66] E. Waks, K. Inoue, C. Santori, D. Fattal, J. Vuckovic, G. S. Solomon, and Y. Yamamoto, *Nature (London)* **420**, 762 (2002).
- [67] A. Imamoglu, D. D. Awschalom, G. Burkard, D. P. DiVincenzo, D. Loss, M. Sherwin, and A. Small, *Phys. Rev. Lett.* **83**, 4204 (1999).
- [68] A. Imamoglu, D. D. Awschalom, G. Burkard, D. P. DiVincenzo, D. Loss, M. Sherwin, and A. Small, *Phys. Rev. Lett.* **83**, 4204 (1999).
- [69] J. M. Gerard and B. Gayral, *Journal of Lightwave Technology* **17**, 2089 (1999).
- [70] L. C. Andreani and G. Panzarini, *Phys. Rev. B* **17**, 2089 (1999).

-
- [71] H. Heidemeyer, U. Denker, C. Muller, and O. G. Schmidt, *Phys. Rev. Lett.* **91**, 196103 (2003).
- [72] T. I. Kamins and R. S. Williams, *Appl. Phys. Lett.* **71**, 1201 (1997).
- [73] D. S. L. Mui, D. Leonard, L. A. Coldren, and P. M. Petroff, *Appl. Phys. Lett.* **66**, 1620 (1995).
- [74] B. Yang, F. Liu, and M. G. Lagally, *Phys. Rev. Lett.* **92**, 025502 (2004).
- [75] H. Lee, J. A. Johnson, M. Y. He, J. S. Speck, and P. M. Petroff, *Appl. Phys. Lett.* **78**, 105 (2001).
- [76] H. Cao, J. Y. Xu, W. H. Xiang, Y. Ma, S. H. Chang, S. T. Ho, and G. S. Solomon, *Appl. Phys. Lett.* **76**, 3519 (2000).
- [77] W. Fang, J. Y. Xu, A. Yamilov, H. Cao, Y. Ma, S. T. Ho, and G. S. Solomon, *Opt. Lett.* **27**, 948 (2002).
- [78] D. Lee and J. Blakely, *Surf. Sci.* **445**, 32 (2000).
- [79] M. Kitamura, M. Nishioka, J. Oshinowo, and Y. Arakawa, *Jpn. J. Appl. Phys., Part 1* **8B**, 4376 (1995).
- [80] D. Leonard, K. Pond, and P. M. Petroff, *Phys. Rev. B* **50**, 11687 (1994).
- [81] N. Haider, M. R. Wilby, and D. D. Vvedensky, *Appl. Phys. Lett.* **62**, 3108 (1993).
- [82] G. S. Solomon, M. Pelton, and Y. Yamamoto, *Phys. Rev. Lett.* **86**, 3903 (2001).
- [83] C. Santori, D. Fattal, M. Pelton, G. S. Solomon, and Y. Yamamoto, *Phys. Rev. B* **66**, 045308 (2002).
- [84] A. Kiraz, P. Michler, C. Becher, B. Gayral, A. Imamoglu, Lidong Zhang, and E. Hu, *Appl. Phys. Lett.* **78**, 3932 (2001).
- [85] A. Imamoglu, D. D. Awschalom, G. Burkard, D. P. DiVincenzo, D. Loss, M. Sherwin, and A. Small, *Phys. Rev. Lett.* **83**, 4204 (1999).
- [86] C. Santori, G. S. Solomon, M. Pelton, and Y. Yamamoto, *Phys. Rev. B* **65**, 073310 (2002).
- [87] K. F. Karlsson, E. S. Moskalenko, P. O. Holtz, B. Monemar, W. V. Schoenfeld, J. M. Garcia, and P. M. Petroff, *Appl. Phys. Lett.* **78**, 2952 (2001).

-
- [88] M. Bayer, G. Ortner, O. Stern, A. Kuther, A. A. Gorbunov, A. Forchel, P. Hawrylak, S. Fafard, K. Hinzer, T. L. Reinecke, S. N. Walck, J. P. Reithmaier, F. Klopff, and F. Schafer, *Phys. Lett. B* **65**, 195315 (2002).
- [89] B. Urbaszek, R. J. Warburton, K. Karrai, B. D. Gerardot, P. M. Petroff, and J. M. Garcia, *Phys. Rev. Lett.* **90**, 247403 (2003).
- [90] E. L. Ivchenko and G. Pikus, *Superlattices and Other Heterostructures, Symmetry and Optical Phenomena* (Springer, New York, 1995), Vol. **110**, Chap. 5, p.160.
- [91] Z.G. Xie, G. S. Solomon, unpublished.
- [92] W. Wu, J. R. Tucker, G. S. Solomon, and J. S. Harris, *Appl. Phys. Lett.* **71**, 1083 (1997).
- [93] G. S. Solomon, W. Wu, J. R. Turker, and J. S. Harris, *Physica E* **2**, 709 (1998).
- [94] E. Waks, K. Inoue, C. Santori, D. Fattal, J. Vuckovic, G. S. Solomon, and Y. Yamamoto, *Nature (London)* **420**, 762 (2002).
- [95] A. Imamoglu, D. D. Awschalom, G. Burkard, D. P. DiVincenzo, D. Loss, M. Sherwin, and A. Small, *Phys. Rev. Lett.* **83**, 4204 (1999).
- [96] G. S. Solomon, M. Pelton, and Y. Yamamoto, *Physica Status Solidi C* **4**, 1205 (2003).
- [97] G. S. Solomon, M. Pelton, and Y. Yamamoto, *Phys. Rev. Lett.* **90**, 229702 (2003).
- [98] Y. Liu, S. Shimomura, N. Sano, K. Gamo, A. Adachi, and S. Hiyamizu, *Semicond. Sci. Technol.* **8**, 2197 (1993).
- [99] G. Wang, S. Fafard, D. Leonard, J. E. Bowers, J. L. Merz, and P. M. Petroff, *Appl. Phys. Lett.* **64**, 1994 (2815).
- [100] H. Yu, S. Lycett, C. Roberts, and R. Murray, *Appl. Rev. Lett.* **69**, 4087 (1996).
- [101] D. Morris, N. Perret, and S. Fafard, *Appl. Rev. Lett.* **75**, 3593 (1999).
- [102] A. Fiore, P. Borri, W. Langbein, J. M. Hvam, U. Oesterle, R. Houdre, R. P. Stanley, and M. Hegems, *Appl. Phys. Lett.* **76**, 3430 (2000).
- [103] F. Pulizzi, A. J. Kent, A. Patane, L. Eaves, and M. Henini, *Appl. Phys. Lett.* **84**, 3046 (2004).
- [104] G. S. Solomon, M. Pelton, and Y. Yamamoto, *Phys. Rev. Lett.* **86**, 3903 (2001).

-
- [105] Weidong Yang, Roger R. Lowe-Webb, Hao Lee, and Peter C. Sercel, *Phys. Rev. B* **56**, 13314 (1997).
- [106] P. Michler, A. Hangleiter, M. Moser, M. Geiger, and F. Scholz, *Phys. Rev. B* **46**, 7280 (1992).